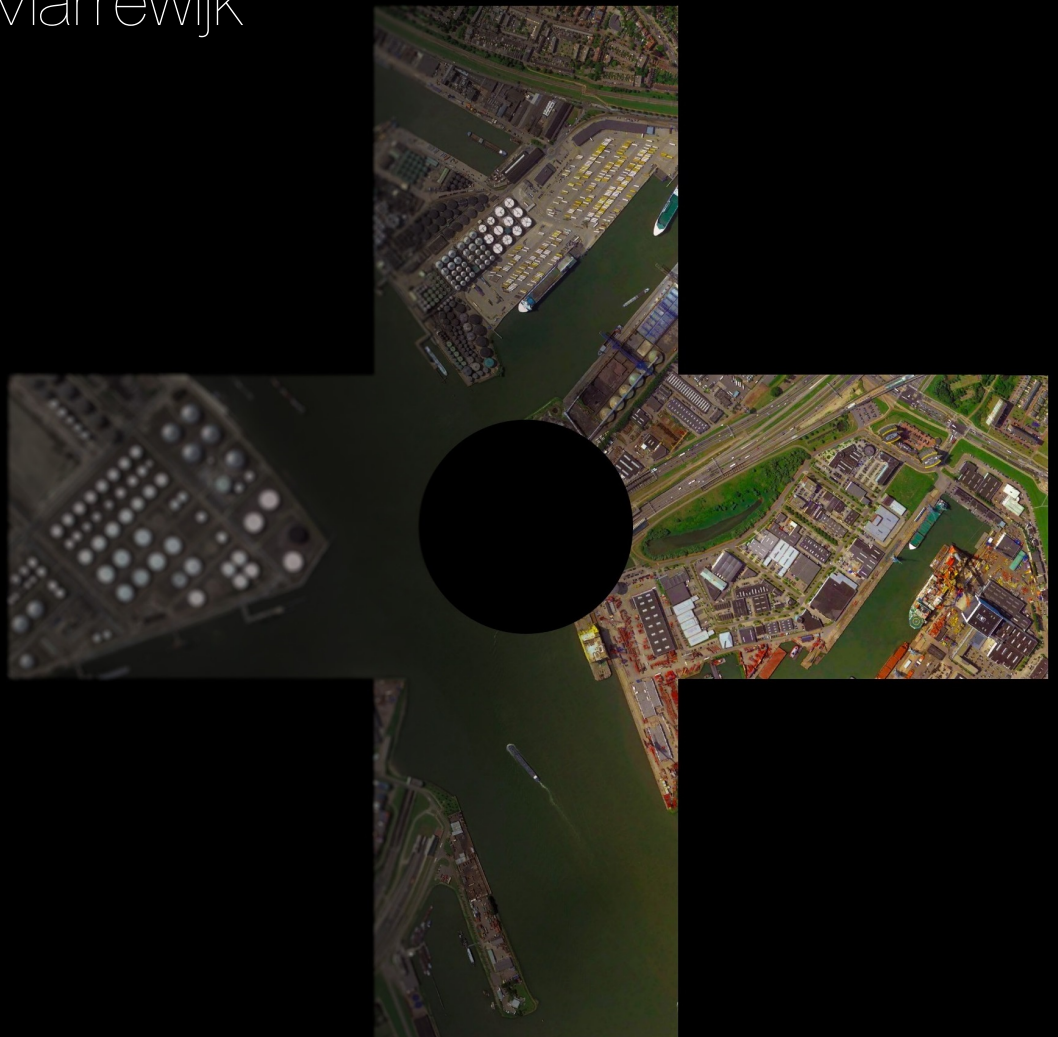# Design of an

Aberration Correction System

for a Deployable Space Telescope

G. P. van Marrewijk

TUDelft

Design of an

Aberration
Correction System

for a Deployable Space Telescope

by

G. P. van Marrewijk

To obtain the degree of Master of Science
in Space Systems Engineering

Report Version: 1.0
Student number: 4137787
Project duration: June 27, 2017 – May 7, 2018
Supervisors: Dr. ir. J. M. Kuiper,   TU Delft, SSE
                    D. Dolkens, MSc.,   TU Delft, SSE

This thesis is confidential and cannot be made public until May 7, 2019.

Cover satellite image: DigitalGlobe via Google Earth

TUDelft

For any man with half an eye
What stands before him can espy;
But optics sharp it needs, I ween,
To see what is not to be seen.

– JOHN TRUMBULL, *MCFINGAL* (1775)

Summary

The Deployable Space Telescope project aims to lower the launch costs for high-resolution space telescopes for Earth observation, by making the primary and secondary telescope mirrors deployable. However, such a system is sensitive to optical aberrations in the wavefront, which decrease the quality of the acquired images. To counteract these aberrations, five different concepts for an Aberration Correction System (ACS) are proposed. The most promising concept is studied in more detail. A deformable mirror (DM) is used for correction of the optical path. The DM is modelled with a ray trace model for a face sheet DM supported by an optimised pattern of push-pull actuators, and with a model for an existing monomorph DM. Both mirrors offer sufficient theoretical performance to improve the Strehl ratio on the central field to a value above 0.8 with the given tolerance budgets.

To evaluate the entire correction system, the ray trace model is extended with a simulation of the aberration control loop. A parallel perturbation stochastic gradient optimisation algorithm is applied to the output of two time-delay integration detectors. In this way, the DM deformation can be optimised during in-orbit ground scanning operations. The effects of different mirror types, different sharpness metrics and different algorithm settings are analysed in a Monte-Carlo simulation. In the final system design, coarse calibration is performed with modal control variables and a sharpness metric based on the sum of the squared pixel intensities. Fine calibration is performed with simultaneous zonal control of each actuator and an edge sharpness metric. With this novel design and application of the control method, an average Strehl ratio of above 0.9 and 0.8 can be achieved on the central field and extreme field of the primary detector, respectively. Finally, in-orbit optical drift effects can be actively compensated without interrupting nominal operations.

Keywords: *Deformable mirror, image sharpness, stochastic gradient descent, space telescope, Earth observation, machine learning, monomorph mirror, ray tracing, simulation*

Preface

From the age of four to the age of twenty-five, I have been educated by many different teachers, trainers, students, lecturers and professors. From many of these people, I can still remember the new things that they taught me, whether it was about how to write the letter k, how to apply the laws of diffraction, or why a personal opinion is something different than a fact.

Considering the support I received from all these teachers for over more than two decades, it makes me glad to present this thesis, which can be regarded as the ultimate piece of homework.

Before the start of a large project such as the MSc thesis project, it is always hard to get a firm grip on the work that needs to be done and how to choose directions. Luckily, the people around me have helped me to make the right choices throughout the project, thereby not only speeding up my work, but also reducing my stress level.

First of all, I would like to thank Hans Kuiper and Dennis Dolkens for their unlimited support. The level of freedom Hans has given has encouraged me to use my own approach during the project, which has been essential for my motivation and the development of my personal view on the subject. Also, the contact with Dennis has been essential for all aspects of the thesis. He has not only been able to tell me everything about modern optical design and ray tracing (albeit not in the comments of his code), but he also could be reached for feedback on fresh simulation results at any time of the day. Thanks to him, many missteps have been avoided and the number of design iterations I could perform has been much higher than when I would have done the project on my own.

This brings me to the word of thanks for the other DST project members. Although Víctor Villalba is the youngest person working on the project, he can proudly say he is already a PhD researcher. Thanks to this, his powerful desktop PC could be confiscated by me at any time to start a new simulation for the greater good of the project. I thank him for accepting this without too much complaints. Unfortunately, even now, I can still not assure him his engineering budgets will be relaxed any time soon.

My fellow students that work on the DST project have supported me throughout the year and have provided a lot of positive comments on the design of the experiments and the presentation of the results. Their *gezelligheid* on the eighth floor will be missed after the graduation.

With a more serious tone, I like to thank Gleb Vdovin and his fellow organisers of the course on adaptive optics. Without their experience and teaching skills, I would have needed many more months to grasp the most important knowledge in this field of research.

Also, I am grateful to Bertrand Charlet from Alpao, Raphaël Cousty from CILAS and Stefan Kuiper from TNO, because the have been so helpful to provide any data I requested in order to develop a realistic model of their deformable mirrors. Without it, the current level of realism of the experiments could not have been achieved.

Because a thesis can take up a lot of personal time, I want to thank my girlfriend Janne for understanding my sudden absence every time I had to check the simulation output on my laptop or when I wanted to implement a new idea in the evening hours.

Finally, I thank my parents, Robert and Cynthia, for always supporting me throughout my studies and never doubting my ability to become a MSc in Space Systems Engineering.

Gijsbert van Marrewijk
Delft, April 2018

Contents

List of Figures

List of Tables

List of Symbols

Symbol	Meaning	Unit
Capital letters		
A	Wave amplitude	$V\,m^{-1}$
$\mathbf{C}$	PDM influence function matrix	multiple
D	Bending stiffness	$N\,m$
D	Aperture diameter	m
E	Phase diversity error	−
F	Spatial frequency	m^{-1}
$\mathcal{F}$	Fourier transform	−
$\mathcal{G}$	Image spectrum	m^{-1}
H	Amplitude Transfer Function	−
$\mathcal{H}$	Optical Transfer Function	−
I	Image	−
M	Magnification	−
$\mathbf{M}$	Modal control calibration matrix	−
N	Number of pixels/measurements	−
O	Geometric image spectrum	m^{-1}
P	PDM actuator force	N
P	Pupil function	−
S	DM sag	m
T	Membrane tension	Pa
U	Light field	$V\,m^{-1}$
V	Voltage	V
$\mathbf{W}$	Zernike term weights of influence function fit	−
Z_n^m	Zernike polynomial of azimuthal freq. m and order n.	varying
Lowercase letters	**Meaning**	**Unit**
c	PDM rigidity coefficient	$N^{-1}\,m^{-2}$
e	Exponential function	−
f	Image sharpness	−
g	Simulated image intensity field	W
h	Coherent PSF	−
$\hbar$	Incoherent PSF	−
i	Intensity value at pixel	−
j	Imaginary unit	−
k	Logarithmic integral	−
k	Scaling term for perturbation variance	−
k_{act}	PDM actuator stiffness	$N\,m^{-1}$
ℓ	on-ground resolution distance	m
n	Index	−
o	Geometric image intensity field	W
p	Power term in sharpness metric	−
p	Actuator pressure on membrane	Pa
r	Radial distance	m
t	Face sheet thickness	m
u	Focal plane x-axis coordinate	m
$\mathbf{u}$	Vector of actuator control signals	multiple

v	Focal plane y-axis coordinate	m
$\mathbf{w}$	weight vector of Zernike terms	–
$\mathbf{x}$	Vector of PDM state variables	multiple
x	Pupil x-axis coordinate	m
y	Pupil y-axis coordinate	m
z	Distance along optical axis	m
z	Complex coordinate $a + bj$	m

Greek letters	Meaning	Unit
α	Direction cosine x-axis	–
β	Direction cosine y-axis	–
Δ_i	Zero-load deflection of PDM actuator i	m
Δ	Difference	–
δ	Mirror deflection	m
δJ	Normalised sharpness change	–
ϵ	Permittivity of material	$F\,m^{-1}$
ζ	Complex coordinates of PDM actuator positions	m
λ	Wavelength	m
λ_0	Reference wavelength of 450 nm	waves
μ	Learning rate of SGD algorithm	–
μ	Sample mean	varying
ν	Poisson's ratio	–
ρ	Correlation coefficient	–
σ	Standard deviation	varying
ϕ	Wavefront (complex phase)	rad
φ	Polar angle	rad

Nomenclature

ACS   Aberration Correction System
ADCS   Attitude Determination and Control System
ADS   Airbus Defence and Space
AHM   Actuated Hybrid Mirror
AO   Active/Adaptive Optics
DCSC   Delft Center for Systems and Control
DM   Deformable Mirror
DOF   Degrees of Freedom
DOT   Design Option Tree
DST   Deployable Space Telescope
EM   Electromagnetic
FBD   Functional Breakdown Diagram
FM   Fold Mirror
FORTA   Fast Optical Ray-Trace Application
FP   Focal Plane
FOV   Field of View
GSD   Ground Sample Distance
IA   Inter Actuator
IQ   Image Quality
JWST   James Webb Space Telescope
M1   Primary Mirror
M2   Secondary Mirror
M3   Tertiary Mirror
MDM   Monomorph Deformable Mirror
MEMS   Microelectronic Mechanical System
MTF   Modulation Transfer Function
OPD   Optical Path Difference
OTF   Optical Transfer Function
PDM   Push-Pull actuator DM
PSF   Point Spread Function
PV   Peak-to-Valley
RDT   Requirements Discovery Tree
RMS   Root Mean Square
SH   Shack-Hartmann
SLM   Spatial Light Modulator
SNR   Signal-to-Noise Ratio
TBD   To Be Determined
TDI   Time Delay Integration detector
TRL   Technology Readiness Level
WF   Wavefront
WFS   Wavefront Sensor

1

Introduction to the Report

This report treats the research and design for a new Aberration Correction System (ACS) for the Deployable Space Telescope (DST) project at Delft University of Technology. It has been written as part of the MSc thesis work at the Faculty of Aerospace Engineering for the MSc programme in Space Systems Engineering.

This report consists of two main parts. The first part of the report consists of Chapters 2 to 5 and focuses on the context of the system, the derivation of system requirements and the generation of different ACS concepts.

Hence, the DST project and its context are introduced in Chapter 2. This chapter also treats the existing market for Earth observation, the goals of the DST project and the goals of this thesis, which logically follow from the project goals. Also, the current design baseline and functions of the instrument are introduced.

To ensure the reader understands the optical theory required for the ACS design, Chapter 3 has been written. With the basic geometrical optics and Fourier optics treated here, the possibilities and limitations of the ACS should become more clear.

Before the system design can be approached in a structural, logical way, the requirements should be derived. This is done in Chapter 4. A preliminary analysis into the optical aberrations in the DST and the space environment are presented, as well as a sensitivity analysis that uses a correlation between the optical budgets and the aberrations to find the most important parameters of the telescope design. At the end of this chapter, an overview of the derived requirements is presented.

With this set of requirements at hand, five conceptual system elements have been derived in Chapter 5. Each of these elements contributes to the overall performance and budgets of the system. The system elements are the *OPD corrector hardware*, the *Location of OPD correction*, the *Aberration detection method*, the *Wavefront control strategy* and the *Optical tolerance drift compensation*. For all of them, different design options are introduced and worked out with the help of Design Option Trees. From the remaining building blocks, five clearly different concepts have been created. These concepts are compared to each other in a trade-off in the same chapter, to determine which concepts are most applicable in the current DST design.

The second part of this report treats the detailed simulation of deformable mirrors and the aberration control system. It consists of Chapters 6 to 9. With the models and results presented in this part, a final design is proposed.

As first part of the simulation, the selected deformable mirrors have been modelled. Hence, the theory and the resulting mirror models are treated Chapter 6. To create the models treated here, manufacturers of deformable mirrors have contributed with their knowledge. This chapter also shows the performance that can theoretically be achieved by the different mirror designs.

With the deformable mirror models in place, the actual control method could be simulated. The theory and a realistic implementation of the control simulation are treated in Chapter 7. Most importantly, a variant of a machine learning algorithm for in-orbit sharpness optimisation is introduced for the first time. At the end of the chapter, the tuning parameters of the control algorithm are explained, and their typical values are defined.

With the modelled mirror and control method, the full ACS simulation could be performed. The results from different case studies and Monte-Carlo simulation results are presented in Chapter 8. It is shown in these results that the performance of the system meets the expectations and that even drifts can be actively compensated during scanning operations.

At the end of this report, in Chapter 9, the design research conclusions and recommendations are presented. The first section treats the final design options that have been selected and the rationale behind this selection. The second section provides a clear overview of the achievement of thesis goals and system requirements. Also, more generally applicable conclusions are drawn for active optics in space instruments. Finally, this chapter closes with a series of recommendations for further research.

I

Theory and Conceptual Design of the Aberration Correction System

Introduction to the First Part

This thesis report consists of two parts to distinguish between the conceptual design of the Aberration Correction System (ACS) and the opto-mechanical simulation of the detailed system design. To explain the design context and the required theoretical background, this first part provides a general introduction to the DST project in Chapter 2, followed by a a short introduction to optical theory in Chapter 3.

With the context and theory known, the system requirements can be derived. This derivation and its corresponding requirements analysis are done with the current state of the DST project taken into account. This means that existing budgets and design choices are used as a baseline. However, it is assumed they are not set in stone. The requirements discovery and analysis is done in Chapter 4.

Finally, this part introduces the five elements of the ACS conceptual design in Chapter 5. Every element is subsequently treated in its own section. These sections all make use of a Design Option Tree for that specific system element. By elimination of design options and by comparing different use cases of the system, five ACS concepts are ultimately generated. With a concept trade-off, it is shown that three different ACS concept are considered as potential candidates for the final design. These candidates are taken to the next part of this report, which focuses on the digital modelling of the different ACS components.

Introduction to the Deployable Space Telescope Project

This chapter introduces the Deployable Space Telescope (DST) project that forms the context of this thesis. Attention is paid to the Deployable Space Telescope project and the role of the current thesis in this project. The status of the project is given in Section 2.1. A short analysis of the existing market for high-resolution Earth observation space telescopes is provided in Section 2.2, followed by an introduction of the need statement, mission statement and the research goals in Section 2.3. The current concept of operations of the DST is explained in Section 2.4. A final note is that some parts of this text are adapted from the Literature Study preceding this thesis [1].

2.1. Status of Deployable Space Telescope Project

The DST project is a research and design project at Delft University of Technology in the Netherlands. A first proposal for this research has been done by Dennis Dolkens in his Msc thesis project [2]. At the time of writing, two PhD researchers and around seven Msc students are working on this project, while two students have already finished their Msc thesis on the DST project. The current team breakdown structure is shown in Figure 2.1. For this project, the FORTA ray trace software is being developed in

Deployable Space Telescope Project
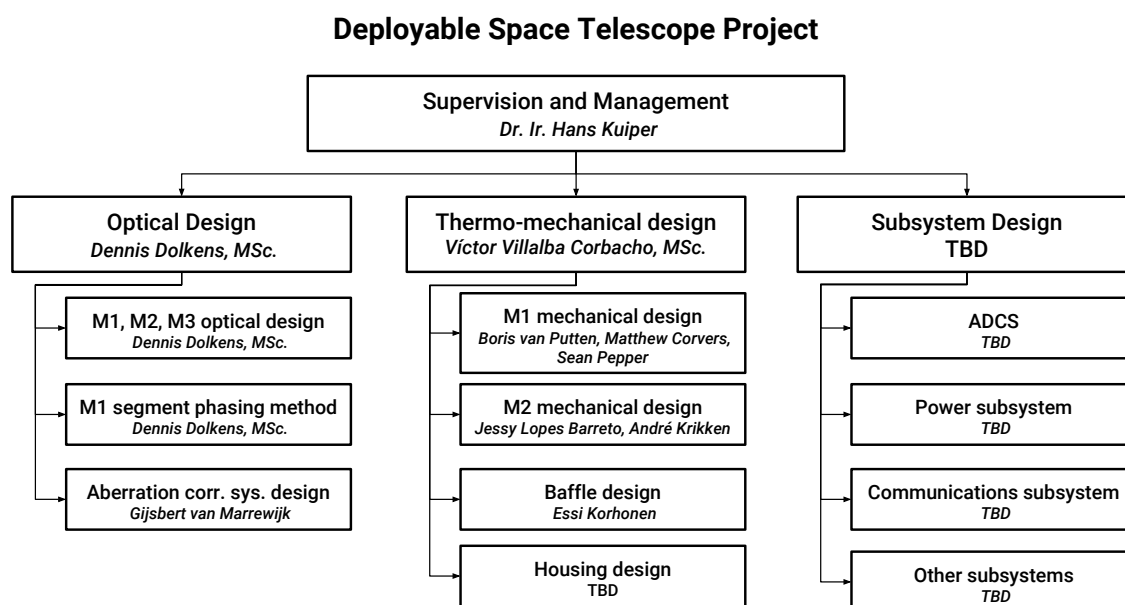
Figure 2.1: Breakdown structure of the DST project team.

MATLAB® by Dolkens [3]. With this software, optical telescopes and control loops can be simulated. Other works that are related to this project are sources [4], [5] and [6].

2.2. Existing Earth Observation Market

Since the advent of satellites, observation of the surface of the Earth from space has become more and more common. National and international defence and security agencies, companies and researchers rely on high-resolution imagery with an almost global coverage.

The major player in the Earth observation market is DigitalGlobe, which is the only company to offer near 30 cm image resolution with its Worldview-3 and Worlview-4 satellites. The Worldview-3 capacity is mainly reserved by the U.S. government, so that services are limited for other parties. However, a few months before the new WorldView-4 satellite went into service, DigitalGlobe has reported an increase in non-U.S. government (commercial) customers[1]. Furthermore, DigitalGlobe has recently been acquired by the Canadian MDA corporation for $ 2.4 billion[2]. This is a clear indication that there is a widespread and growing market need for high-resolution imagery.

However, current Earth observations satellites with a 30 cm ground sampling distance have a mass in the range of 2000 kg[3]. The high mass related to high-resolution telescopes comes from the required telescope aperture diameter, as explained in Chapter 3. An increase in resolution by a factor x will require an aperture increase by the same factor, naturally leading to higher system mass. This relationship has been plotted in Figure 2.2. The design point of the DST is far from the mass trend. Note that subsystem mass has not been included in the DST design point yet.
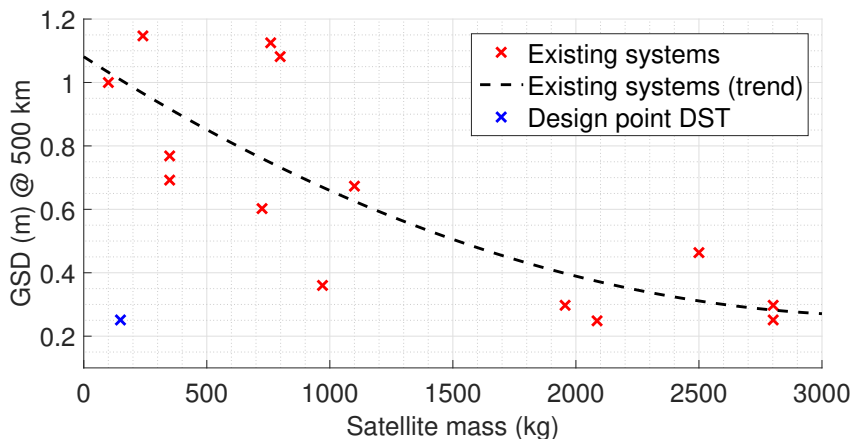
Figure 2.2: Ground Sampling Distance (GSD) versus system mass for the space telescopes listed by Dolkens [2, Table 2.2]. It can be seen that the design mass of the DST is an order of magnitude below that of existing systems. Note that subsystems have not yet been taken into account for the design point.

Regarding the costs for high-resolution telescopes, the following is known: for WorldView-3, development and integration was valued at $307 million in 2010[4]. For WorldView-4, previously known as GeoEye-2, costs were ca. $850 million[5], taking into account ground network upgrades. Of this cost, the launch costs are up to several hundreds of millions of dollars [1]. So, currently, the price of the launch is significant with respect to the price of development and integration. Hence, a reduction in satellite mass and stowed size enables the launch of multiple spacecraft in one launcher, or the reduction of launcher size. This greatly reduces the mission cost. Also, the price per unit will go down when multiple telescopes are integrated at the same time.

---

[1] http://spacenews.com/digitalglobe-reports-broad-commercial-growth-ahead-of-worldview-4-launch, published: 1-8-2016, retrieved: 6-5-2017

[2] http://spacenews.com/mda-to-acquire-digitalglobe, published: 24-2-2017, retrieved: 6-5-2017

[3] www.digitalglobe.com/resources/satellite-information, retrieved: 6-5-2017

[4] http://spacenews.com/digitalglobe-awards-307m-contracts-worldview-3-satellite, published: 31-8-2010, retrieved: 6-5-2017

[5] http://spacenews.com/geoeye-2-price-tag-rises-ground-system-upgrades-0, published: 12-11-2010, retrieved: 6-5-2017

2.3. Research Goals from Need and Mission Statements

From the previous section and from Dolkens [2], it follows that there is an increasing demand for high-resolution Earth imagery, but that the supply of new instruments is limited. A lower cost of the instrument will result in more Earth-observation telescopes in orbit, which in turn increases the ground location revisit frequency. With this information, the following need statement for a space telescope mission has been derived by the author:

Need statement
There is a need for a dramatic decrease in launch costs of high-resolution Earth observation telescopes to provide data with a higher temporal resolution and at a lower price than what is currently possible.

Dolkens proposes to reduce launch mass and cost by developing a Deployable Space Telescope (DST) with a GSD of less than 30 cm per pixel and a mass and stowed volume that are below that of existing designs [2]. The mission goal can thus be stated as follows:

Mission goal
To design and develop a Deployable Space Telescope (DST) that is capable of achieving the same GSD as state-of-the-art Earth imaging satellites, but at a fraction of the stowed volume and mass.

To achieve this goal, a bottom-up systems engineering approach is used. With this approach, it has been found that stringent deployment tolerances are required for the deployable mirrors. This has been illustrated in the need and solution flow diagrams in Figure 2.3. However, even with these tolerances, the optical performance of the telescope will still be lower than that of existing heavy and large telescopes. This is caused by so-called optical aberrations that are introduced when the optical components are not perfectly aligned or when they deform. See Chapter 3 for more information on aberrations.

To remove aberrations in the DST, an Aberration Correction System (ACS) is proposed. This system shall remove the aberrations to such an extent, that diffraction-limited performance is possible on the DST. Hence, the following research question and research objectives are formulated.
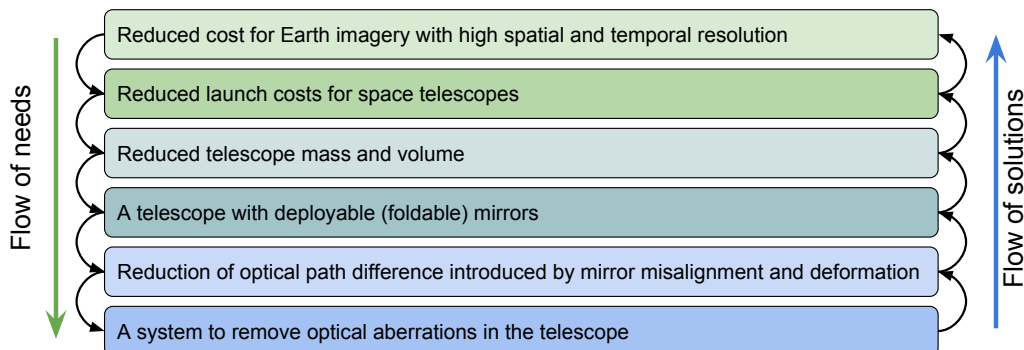
Figure 2.3: Derivation of needs and solutions to fulfil these needs, from high to low order problems. It can be seen that the need for an aberration correction system (ACS) is derived from the need for low-cost imagery.

Research question
What is the maximum performance gain that can be achieved by an Aberration Correction System on the Deployable Space Telescope, while staying within the existing telescope engineering budgets?

Research objective
The objective of the research project is to find the maximum performance gain of an aberration correction system on the Deployable Space Telescope by making a simulation to obtain the performance of different designs and by experimentally testing a breadboard version of the design that performs best with respect to the trade-off criteria.

The framework which will support this objective is shown in Figure 2.4. With the objective and the approach from this framework, the following subgoals are set.

Subgoal 1 To find the system functions and design options for an Aberration Correction System (ACS) on the DST by collecting and confronting knowledge obtained from a literature study, the Delft Center for Systems and Control, the current DST design and existing ACS systems.

Subgoal 2 To write an ACS simulation program that can be implemented in the existing FORTA software.

Subgoal 3 To assess the performance of different ACS concepts by simulating them in FORTA.

Subgoal 4 To deduce trade-off criteria by analysing the engineering budgets and ACS requirements and subsequently to perform a trade-off by confronting the ACS concepts with the criteria and selecting the winner of the trade-off.

Subgoal 5 To validate the performance of the selected concept by comparing the simulation output with experimental measurements from a breadboard system in a laboratory setup.

Subgoal 6 To establish recommendations on a detailed ACS design for the DST by applying an iterative design process on the selected concept(s) and involving the DST requirements, DCSC knowledge and available technologies.

MSc Thesis Research Framework

An Aberration Correction System (ACS) for the Deployable Space Telescope (DST)
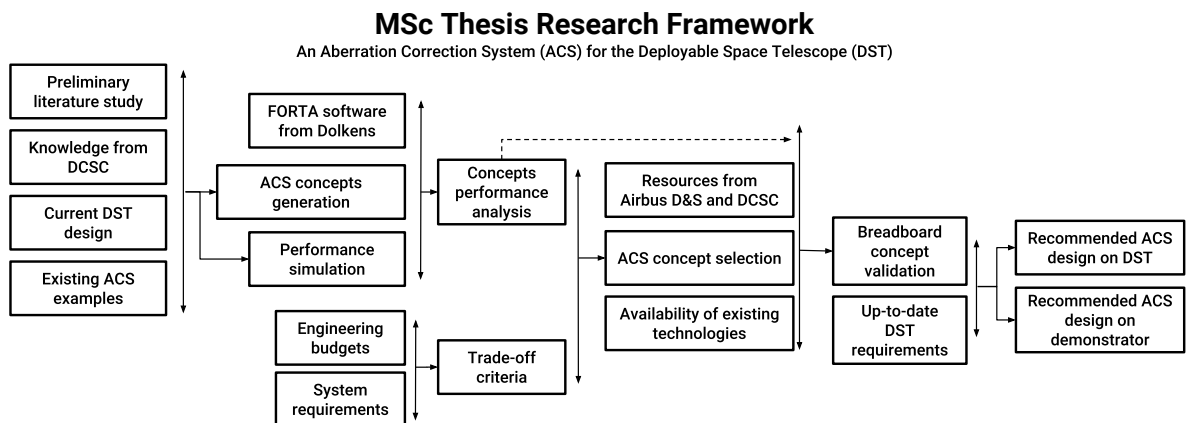
Figure 2.4: Research framework of the project. Vertical lines indicate confrontations between different sources of information. The horizontal axis indicates the logical order of the research. DCSC is Delft Center for Systems and Control, ACS is Aberration Correction System.

2.4. Telescope and Mission Design Concepts

The basic concept of the DST system architecture is shown in Figure 2.5, while a render of the most recent mechanical design iteration (without baffle) is shown in Figure 2.6. Furthermore, a functional flow diagram for a typical mission is given in Figure 2.7. Regarding the functional flow diagram, this thesis project deals with function F-12 and optionally F-14, if this is found to be required.

A short description of the key elements of the architecture in Figure 2.5 is provided below.

1. To create high-resolution Earth imagery, the telescope mirrors accept incoherent, polychromatic light from Earth and focus it on the detectors in the focal plane array (FPA).

2. To save mass and volume, the primary and secondary mirrors are stowed during launch and deploy in space.

3. To remove discontinuities from the optical wavefront that reaches the detector, a segment phasing system brings the primary mirror segments in phase with sub-micrometer accuracy.

4. To remove remaining aberrations from the wavefront, an aberration correction system controls a deformable mirror or other OPD corrector. These aberrations can be caused by e.g. misalignment and thermal expansion of materials.

5. To prevent both straylight and large thermal gradients in the deployable mirrors, a deployable baffle can be included in the design.

6. To digitally restore imagery, a wavefront estimate is required. For this, data from the image detectors can be used. Raw data or restored data can be downlinked to Earth.

7. To handle power distribution, data and communications with Earth, a spacecraft bus is required for the instrument. The bus also holds an attitude determination and control system for pointing and ground location tracking. At this point in the instrument design project, the bus is not included.
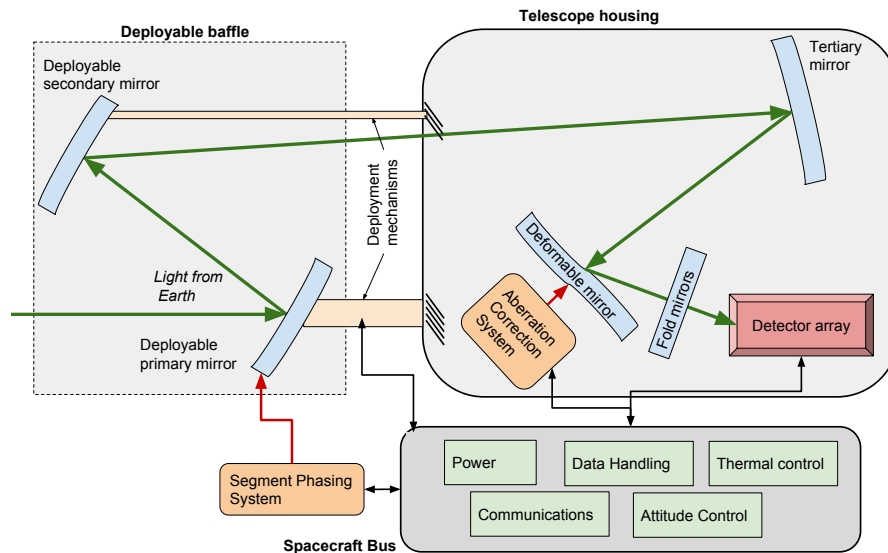
Figure 2.5: Conceptual architecture of the DST and spacecraft bus.
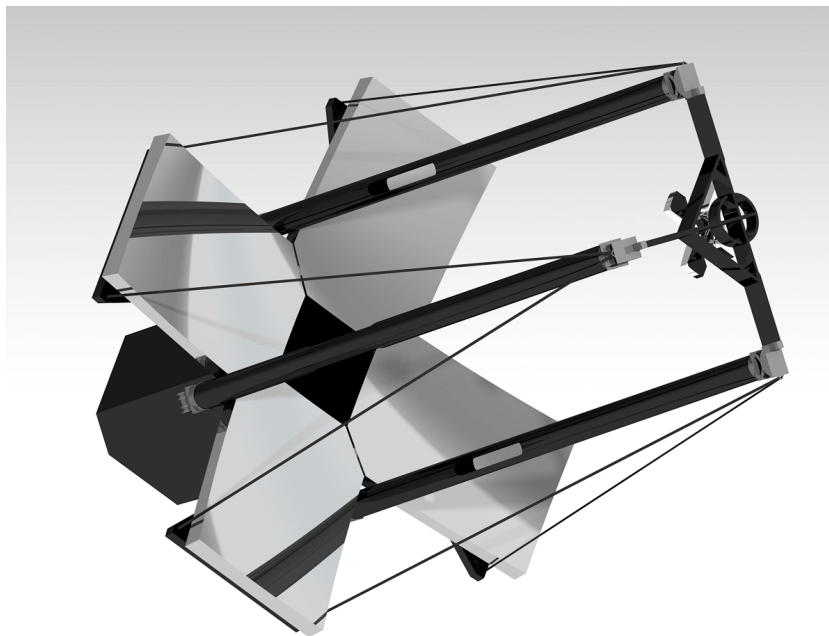
Figure 2.6: Render of the DST design, without baffle and spacecraft bus and with deployed mirrors. Courtesy André Krikken and Matthew Corvers.

As explained in Section 2.2, existing space telescopes use relatively heavy and stiff optical components and support structures. This keeps the misalignment and deformation budgets within the
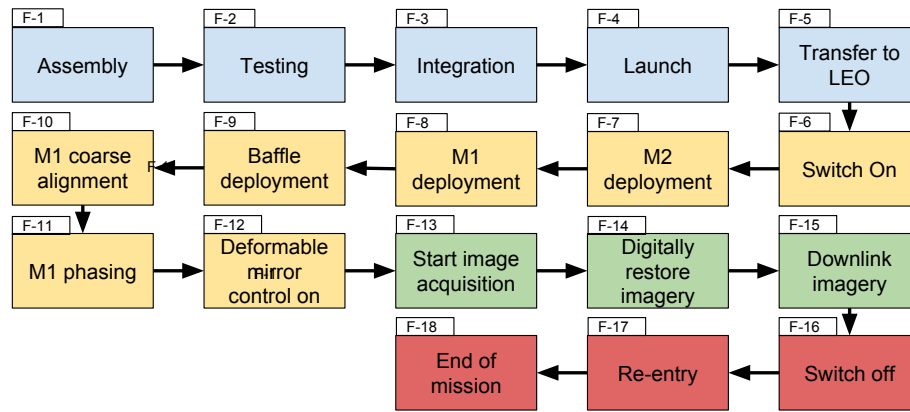
Figure 2.7: Functional flow for a typical DST mission. Sub-functions such as drift compensation are not shown in this top-level flow diagram.

tolerance bounds for diffraction-limited imaging. Considering that the goal of the DST project is to minimise the mass and volume of the high-resolution telescope, another design philosophy is required. Instead of relying on passive mechanical stability, the telescope uses active compensation of the optical path difference (OPD) of the light rays. This design philosophy has become practically applicable with the increase in available low-cost, low-mass active optical components [7] and has been adopted by different projects for space optics engineering [8–11]. Besides this, an increase in computational power during the past few decades has made digital wavefront estimation a possibility, for example with the phase diversity method [12]. More information on the optical theory that drives the DST design is provided in the next chapter.

3

Theory on Optics and Image Simulation

This chapter aims to provide a concise overview on topics in the field of optics, which are relevant for understanding the role of the ACS in the DST and its principles of operation. Some of the text in the next sections has been adapted from the Literature Study [1]. The information provided is primarily obtained from sources [13–16]. Section 3.1 treats basic geometrical optics, followed by an introduction into angular spectrum propagation in Section 3.2. Subsequently, imaging theory and diffraction are treated in Section 3.3. Finally, the basics of the optical design of the DST are provided in Section 3.4.

3.1. Geometrical Optics Basics

This section contains information on some basic geometrical optics principles. In an optical system, the *object* or *source* is located on the object plane, while the *image* is located on the image plane. The object side is normally shown on the left in a figure of an optical system, the image side is shown on the right. For an Earth observation space telescope, the object is the *scene* on the ground.

The *aperture* limits the size of the cone of light that originates from an object point and reaches the image plane detector. The image of the aperture on the object side is the *entrance pupil*, while the image of the aperture on the image side is the *exit pupil*. For an Earth observation space telescope, the aperture stop is usually the primary mirror. Hence, this is also the entrance pupil. The dimensions of the aperture determine the spatial resolution of the telescope, while the area of the aperture is one of the factors that determine the maximum power that can be received from a source.

The *chief ray* is the ray of light from an object point that crosses the aperture stop on the optical axis. A *marginal ray* is a ray that is just passing by the edge of the aperture stop (and hence also the edge of the entrance and exit pupils). If the size of the cone of light is not constant over all object points, the system suffers from *vignetting*, which is unwanted for *radiometric* performance, as it makes the energy received from a beam dependent on the field location where it originates.

The *field size* of the system and the object distance define the maximum dimensions that can be imaged. The field size can be limited by the *field stop*, but this is usually the detector in Earth observation space telescopes. The *magnification* of the system is the ratio between the image and the object size. For Earth observation telescopes, this can be closely approximated by the ratio of focal length f to orbital height h, assuming the telescope looks to nadir:

$$M = \frac{f}{h}. \tag{3.1}$$

To include the physical phenomenon of *diffraction* in the optical analysis, the propagation of light is not described by rays but by wavefronts. A perfectly spherical wavefront will focus the light from an object on a *diffraction-limited* point, see the next sections. The *Rayleigh criterion* gives an indication on the maximum resolution that can be achieved, considering diffraction. Here, resolution is defined as the distance between two point sources, when one maximum of the diffraction-limited point spread function (PSF) is at the first minimum of the second diffraction-limited PSF. This can be approximated by

$$\Delta \ell \approx 1.22 \frac{\lambda h}{D}, \tag{3.2}$$

where $\Delta\ell$ is the on-ground resolution, λ the wavelength, h the distance to the scene and D the diameter of a circular telescope.

Deviations from the spherical wavefront are called *aberrations*. They are usually described by *Zernike polynomials*, Z_n^m, where n is the *order* and m is the *azimuthal angle*. Figure 3.2 shows these polynomials. The shape indicates the offset from the perfectly spherical wavefront. *Spherical aberration, coma* and *astigmatism* are the three classical aberrations. They can theoretically be removed in *three-mirror anastigmat* optical designs, such as the Korsch telescope design used for the DST. See Section 3.4.

When aberrations are present, the maximum intensity in the image of a bright point at infinite distance is lower than when the system is aberration-free. The ratio between the maximum brightness and the ideal maximum brightness of this point is called the Strehl ratio [7]. Although is is used often as a measure for system performance, its value is not easily determined in practice [17]. See also Section 3.3.

3.2. Angular Spectrum Propagation

When it is assumed that a plane wave with wavelength λ travels under an angle with respect to some axis Z, a plane parallel to the XY-axes gets a pattern of maxima and minima that changes with time. See Figure 3.1.
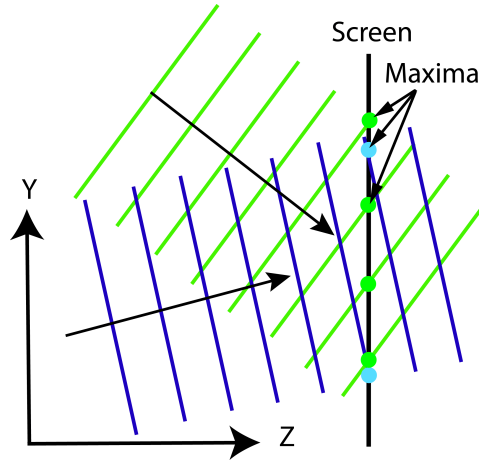
Figure 3.1: Two plane waves propagating under an angle with respect to the Z-axis cause a pattern of maxima and minima on the screen. The frequency and phase change per unit distance along Z depend on the angle of propagation, leading to a relation between the bending of light by a lens or mirror, and the Fourier transform of the light distribution of the source.

When α is the direction cosine w.r.t. the X-axis and β the direction cosine w.r.t. the Y-axis, the frequency of these maxima and minima can be given by $F_x = \alpha/\lambda$ and $F_y = \beta/\lambda$. So, the angles from which the plane waves arrive at the screen at $z = 0$ determine the frequency components that are used in a Fourier transform [16]. Therefore, the Fourier transform of the field is given

$$A\left(F_x, F_y, 0\right) = \iint_{-\infty}^{\infty} U(x, y, 0) \exp\left(-2\pi j\left(F_x x + F_y y\right)\right) dx dy. \tag{3.3}$$

and $A(F_x, F_y, 0)$ is considered the *angular spectrum* of the amplitude field $U(x, y, 0)$. It can be seen as the weighting function of plane waves from different directions to obtain the amplitude field. Note that the phase of the spectral components changes when the screen is moved in Z-direction. In that case, high frequencies (higher angles) will see a larger shift in phase.

Let us consider an aperture with pupil function $P(x, y)$ at the plane under consideration. Then $P(x, y) = 1$ if the light can pass at (x, y) and $P(x, y) = 0$ if the light is blocked. In this case, the angles from which the planar waves can reach the plane under consideration are limited. The aperture can thus be said to be a filter on angular frequencies.

Index	Noll's ordering	Name	Expression	Shape	PSF
$Z_0^0(x,y)$	1	piston	1		
$Z_1^1(x,y)$	2	tip	x		
$Z_1^{-1}(x,y)$	3	tilt	y		
$Z_2^0(x,y)$	4	defocus	$2x^2 + 2y^2 - 1$		
$Z_2^2(x,y)$	5	astigmatism	$x^2 - y^2$		
$Z_2^{-2}(x,y)$	6	astigmatism	$2xy$		
$Z_3^1(x,y)$	7	coma	$3x^3 + 3y^2x - 2x$		
$Z_3^{-1}(x,y)$	8	coma	$3y^3 + 3x^2y - 2y$		
$Z_3^3(x,y)$	9	trefoil	$x^3 - 3xy^2$		
$Z_3^{-3}(x,y)$	10	trefoil	$3x^2y - y^3$		
$Z_4^0(x,y)$	11	spherical	$6x^4 + 12y^2x^2 - 6x^2 + 6y^4 - 6y^2 + 1$		
$Z_4^2(x,y)$	12		$4x^4 - 3x^2 - 4y^4 + 3y^2$		
$Z_4^{-2}(x,y)$	13		$8yx^3 + 8y^3x - 6yx$		
$Z_4^4(x,y)$	14		$x^4 - 6y^2x^2 + y^4$		
$Z_4^{-4}(x,y)$	15		$4x^3y - 4xy^3$		

Figure 3.2: First fifteen Zernike polynomials, expressed in Cartesian coordinates. The index is given as Z_n^m, where n is the *order* and m is the *azimuthal angle*. Adapted from [18].

3.3. From OPD to Simulated Image

The differences between the optical path lengths of rays in the exit pupil is called the optical path difference (OPD). The OPD can be calculated by *ray tracing*, which is done by e.g. the FORTA software developed by Dennis Dolkens at Delft University of Technology. This section describes how the OPD can be used to determine optical performance and simulate images.

The OPD can be converted to the phase error in the exit pupil via:

$$\phi\left(x, y\right) = \frac{2\pi}{\lambda} \cdot OPD\left(x, y\right) \tag{3.4}$$

where x, y denote exit pupil coordinates and λ is the wavelength. From Fourier optics [16], it follows that the *Amplitude Transfer Function* (ATF) is

$$H\left(F_x, F_y\right) = P\left(\lambda z_i F_x, \lambda z_i F_y\right) e^{-j\phi\left(\lambda z_i F_x, \lambda z_i F_y\right)} \tag{3.5}$$

where z_i is the image distance from the pupil. If the OPD is zero everywhere, eq. 3.5 reduces to $H\left(F_x, F_y\right) = P\left(\lambda z_i F_x, \lambda z_i F_y\right)$ and there are no aberrations. In this ideal case, the system is diffraction-limited. To achieve this goal with a deformable mirror (DM), the deformation or sag of the DM should be

$$S(x, y) = -\frac{OPD(x, y)}{2}, \tag{3.6}$$

because the wavefront travels the local deformation distance twice, due to its reflected path.

The coherent *Point Spread Function* (PSF) of a space-invariant system is found with an inverse Fourier transform of the ATF. It is expressed at image plane coordinates u, v:

$$h\left(u, v\right) = \mathcal{F}^{-1}\left\{H\left(F_x, F_y\right)\right\} \tag{3.7}$$

Since the Earth observation telescope receives light from an incoherent source [2], the incoherent PSF is required to simulate images. The incoherent PSF defines intensity instead of wave amplitude and is found via

$$\hbar\left(u, v\right) = \left|h\left(u, v\right)^2\right| \tag{3.8}$$

As stated before, the Strehl ratio of the system is the maximum intensity of the PSF, relative to the maximum intensity of the diffraction-limited PSF:

$$Strehl = \frac{\max\left(\hbar\left(u, v\right)\right)}{\hbar_{diff}\left(0, 0\right)} \tag{3.9}$$

However, the Strehl ratio can also be approximated directly from the OPD. From Mahajan [19], it is found that the approximation is given by

$$Strehl \approx e^{-\mathrm{RMS}(\phi)}, \tag{3.10}$$

where $\mathrm{RMS}\left(\phi\right)$ is the RMS value of the wavefront phase over the pupil.

The *Optical Transfer Function* (OTF), denoted $\mathcal{H}$, is the autocorrelation of the ATF. From the Wiener-Khinchin theorem, it is thus derived that:

$$\mathcal{H}\left(F_X, F_Y\right) = \mathcal{F}\left\{\hbar\left(u, v\right)\right\} \tag{3.11}$$

The absolute value of the complex OTF is called the *Modulation Transfer Function* (MTF) and describes the relative change in contrast at different spatial frequencies. The image formed on a specific field of a detector is found by convolving the ideal image $o\left(u, v\right)$, which is predicted by geometrical optics, and the incoherent PSF of that optical field. In the frequency domain, this becomes a multiplication of the OTF with the geometric image spectrum $O\left(F_x, F_y\right)$:

$$\mathcal{G}\left(F_x, F_y\right) = \mathcal{H}\left(F_x, F_y\right) \cdot O\left(F_x, F_y\right) \tag{3.12}$$

Finally, the simulated image $g\left(u, v\right)$ is found by inverse Fourier-transforming the spectrum;

$$g\left(u, v\right) = \mathcal{F}^{-1}\left\{\mathcal{G}\left(F_x, F_y\right)\right\} \tag{3.13}$$

3.4. Optical Design of the DST

To minimise the three main optical aberrations, i.e. spherical aberration, coma and astigmatism, three mirrors are required. Such telescopes are called three-mirror anastigmats. Such a design is chosen, because the goal of the DST is to acquire diffraction-limited imagery. Initially, a full-field Korsch design [20] was taken as design basis. In such a design, the light is guided away from the optical axis of a Cassegrain telescope part by a fold mirror in the exit pupil. However, this design was found to be sensitive to alignment errors in the primary and secondary mirrors. The main reason for this is the short focal length of the Cassegrain part of the telescope. Furthermore, the full-field Korsch design features an exit pupil fold mirror, which constrains the minimum size of the central hole in the primary mirror. This becomes especially limiting when a larger field-of-view is required.

Therefore, an annular-field Korsch design is used in a more recent design iteration [3], as shown in Figures 3.3 and 3.4. An off-axis optical system is selected for the DST: firstly, the longer focal distance of the Cassegrain part lowers the sensitivity of the primary and secondary mirror alignment. Secondly, the off-axis design makes the exit pupil more accessible for the ACS and allows for a higher cross-track field-of-view (FOV). Thirdly, the off-axis light path allows for more convenient ways to block straylight with baffles, as these need can be placed outside other light paths. See also Lampton [21].

The focal plane array of detectors (FPA) is shown in Figure 3.4. The cross-track FOV is 0.6° and the along-track FOV is 0.25°. In the current design, the FPA features two time delay integation (TDI) detectors for scanning operations, a sensor for staring operations or sharpness optimisation and a region for the placement of multispectral channels to retrieve color information from a scene. From the sideview in Figure 3.3, it can be seen that fold mirrors can be used to move parts of the FPA to different physical locations.
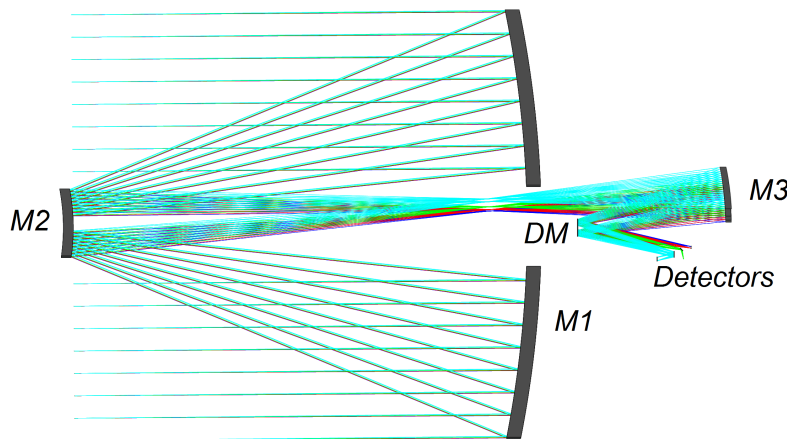
Figure 3.3: Optical lay-out of the Deployable Space Telescope. M1: primary mirror. M2: secondary mirror. M3: tertiary mirror. DM: location for fold mirror or, optionally, a deformable mirror.
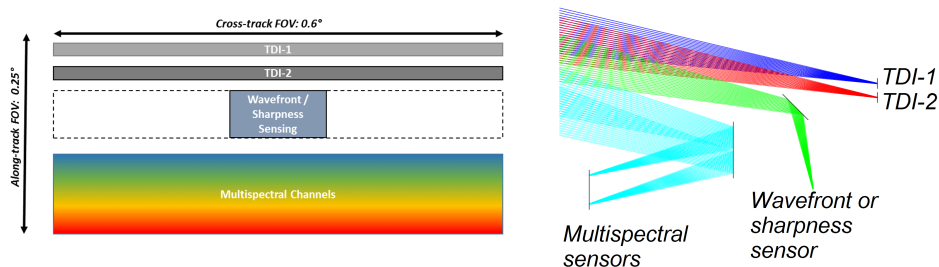
Figure 3.4: Optical lay-out of the focal plane of the Deployable Space Telescope FPA. TDI: Time Delay Integration detector.

4

Requirement Generation

The first step in the design procedure for an Aberration Correction System is to establish system requirements. This chapter is dedicated to that step. Requirements are derived from an analysis of the system context in Section 4.1. The problem of aberration reduction is explained in Section 4.2 and the sensitivity of the aberrations to various design parameters is treated in Section 4.3. Finally, an overview of the requirements is provided in Section 4.4 and the ACS functions are derived in Section 4.5.

4.1. Context of the System
This section treats the context of the Aberration Correction System (ACS). The ACS context can already be determined, because it will be a subsystem of the specific DST system. A lack of understanding of this context may lead to an incorrect or incomplete set of system requirements.

A context diagram can be seen in Figure 4.1. Central in this diagram is the ACS on the DST. The given input of the system is the continuous flow of aberrated light waves, that it receives from the telescope. The desired output of the ACS is a data stream containing diffraction-limited imagery, corresponding to the ground scene on Earth. However, more inputs and outputs are present between the system and its context. To operate the ACS as a subsystem, the other spacecraft subsystems need to provide the required power (also for thermal control) and orientation of the telescope. To control the system, an operator needs to be able to download health and performance data and to upload updates for the on-board software and its settings.

Compared to ground systems, active optics in space are in a different environment. During the mission, the launch and space environments will consist of changing temperatures, pressures and motions such as shock and vibration. Besides this, space radiation, micrometeorites and other particular contamination must be considered.

4.2. Problem Analysis
In Section 2.1, it is explained that the M1 segments are brought in phase after deployment. However, multiple sources can cause optical performance degradation after M1 phasing:

- Misalignment of the M1 segments in the XY-plane are not actively corrected in the current design. This may lead to a loss of circular symmetry of M1.
- The deployment of M2 on its extendable boom has a limited accuracy. In the current design, no active control of the M2 position is envisaged. Therefore, misalignments may occur.
- The limited manufacturing and assembly tolerances of the mirror surfaces may lead to imperfect optical performance.
- Even when no initial misalignments or production tolerances are taken into account, thermal deformations, material creep, outgassing and vibrations in the system can cause time-varying optical performance called *drift*.

See Dolkens [6] for more information on the origin of the tolerances.

The main requirements of the ACS stem from the main project requirement of delivering diffraction-limited imagery with a Deployable Space Telescope. From this starting requirement and from a study
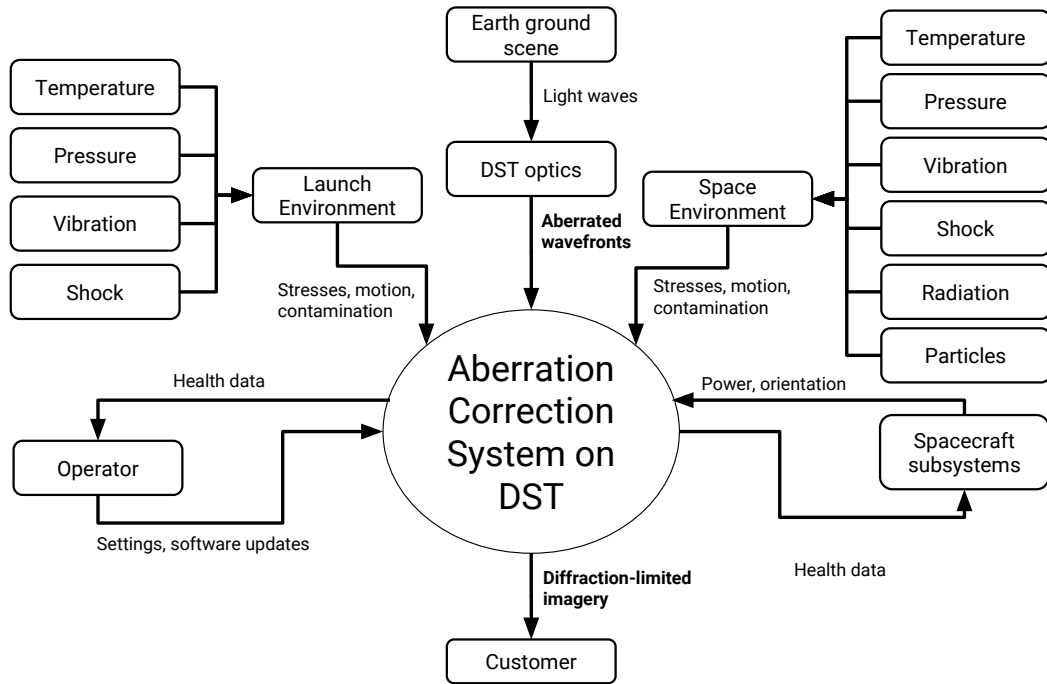
Figure 4.1: Context Diagram of the Aberration Correction System on the Deployable Space Telescope.

of literature on active optics [1], the Requirements Discovery Tree in Figure 4.2 has been established. The main branches of the tree stem from the requirements to detect the quality of the telescope image (either directly or indirectly) and to improve this image quality. The relevant ACS requirements can be generated from the preliminary requirements in the figure (T1, ..., T11). These requirements are discussed in Section 4.4. The two main branches of this tree show that the problem of delivering diffraction-limited imagery has two branches: one for the detection of optical aberrations that deteriorate the image and one for the improvement of the images. For the detection of aberrations, a sensor should achieve a sufficient signal-to-noise ratio and resolution to detect image quality or measure the wavefront with sufficient accuracy to remove the aberrations. It is important that the imagery from Earth scenes can be used, to avoid the need for pointing at stars or to install an artificial point source of light in the telescope.

For the improvement of images, optical aberrations or their effects need to be removed. To remove aberrations, an OPD correction needs to be applied. This correction requires a certain stroke or amplitude of the correcting device and a sufficiently high spatial frequency. Furthermore, temporal drifts and space environment effects should not deteriorate the performance. The Aberration Correction System needs to fit in the existing telescope design to avoid a full redesign of the telescope. Eventual post-processing done on ground should not amplify noise or introduce artefacts.

4.2.1. Aberration analysis

The coarse alignment tolerances of the DST optical components have been established by Dolkens [6] and are shown in Table 4.1. The values shown are the two-sigma bounds of the normal distributions of the alignment, radius and shape errors of the first three telescope mirrors. At this stage of the design, alignment and shape of the other (flat) mirrors is not yet taken into account, because optical performance is much less sensitive to misalignment errors of fold mirrors. The tolerances are determined top-down from maximum allowed error budgets, derived from the optical design point of view. This means that they may change as the detailed design of the DST progresses and more estimates of the thermo-mechanical behaviour of the system become available.

With the coarse alignment tolerances, the DST performance can be simulated in FORTA. From earlier work by Dolkens, [3] and preliminary experiments in FORTA, it is found that the relative misalignments between the four M1 segments cause discrete steps in the wavefront OPD, with Peak-to-Valley

Aberration Correction System
Requirements Discovery Tree

```
                    ┌──────────────────────────────────────┐
                    │  Diffraction-limited imaging on the DST │
                    └──────────────────────────────────────┘
```

| Image quality detection | Image quality improvement |

- Detection hardware
  - T1. Sufficient S/N ratio
  - T2. Sufficient resolution
  - T3. Works in space
- Detection metric
  - T4. Can work with Earth imagery
  - T5. Can be transformed to control signal that corresponds with global error minimum

- Optical Path Difference correction
  - T6. Sufficient amplitude
  - T7. Sufficient WF order
  - T8. Little influence of drift
  - T9. Fits in existing design
- Residual correction in post-processing
  - T10. Low-noise restoration
  - T11. Negligible introduction of artefacts

Figure 4.2: Requirements Discovery Tree of the Aberration Correction System. From this tree, the ACS requirements have been derived.

Table 4.1: Top-down tolerances for coarse alignment. From [6]

Element	Position (µm)			Tilt (µrad)			Radius (%)	Shape Error (nm)
	X	Y	Z	X	Y	Z		
M1	2	2	2	2	4	50	$1 \cdot 10^{-3}$	50
M2	15	15	10	100	100	100	$1 \cdot 10^{-2}$	25
M3	4	4	4	10	10	50	$1 \cdot 10^{-3}$	10

(PV) OPDs of 5 to 50 λ_0, where $\lambda_0 = 450\,\text{nm}$. Hence, to obtain the highest performance from the telescope, the primary mirror segments need to be brought in phase. Different M1 phasing methods are currently being investigated by Dolkens. For the sake of problem analysis in this section, the effects of M1 phasing are simulated in FORTA by subtraction of a plane estimate from the OPD for each segment. The estimate is created from OPD data points at both segment boundaries as shown in Figure 4.3 (left). In this way, only a residual and continuous OPD remains in the exit pupil, as shown in Figure 4.3 (right)[1].

To acquire a more general estimate of the exit pupil OPD after phasing, a combination of Zernike polynomials is fitted to the corresponding wavefront, as illustrated in Figure 4.4. It is found that a combination of Zernike polynomials up to the seventh azimuthal and radial order (36 terms) are required to represent the OPD. An example of the Zernike weights for a seventh-order fit is shown in Figure 4.4 (bottom right).

To find the magnitude and order of the aberrations in the exit pupil after phasing, 1000 coarse alignment and phasing trials are performed in FORTA. Subsequently, Zernike polynomials are fitted to the resulting exit pupil OPD, leading to the boxplot in Figure 4.5. It can be seen that the probability distribution of Zernike terms is nearly symmetrical for positive and negative weights. There is a decreasing

---

[1] At the time of writing, the phasing algorithm that has been developed by Dolkens was not yet available in FORTA, such that this phasing approximation was required

trend towards higher-order terms, with exemptions for Zernike terms with symmetry that is similar to the DST pupil shape, such as term 27 (tetrafoil). Therefore, it can be concluded that a correction of the OPD needs to take into account at least these first 36 terms.
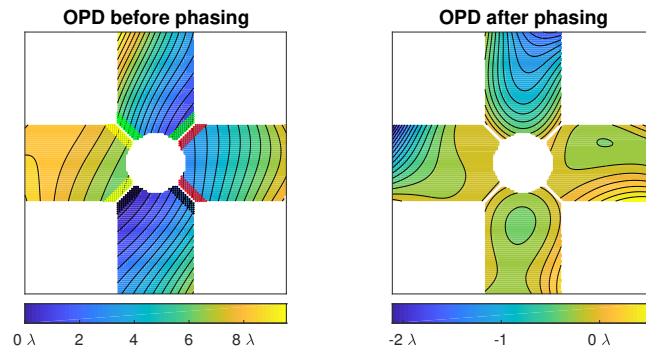
Figure 4.3: Typical exit pupil OPD (in wavelengths at 450 nm) before and after the first-order piston, tip, and tilt are removed. The coloured regions at the segment boundaries (left) indicate the location of the data points used for the estimation of the plane to subtract for phasing simulation. Note the difference in scale between the colour scales.
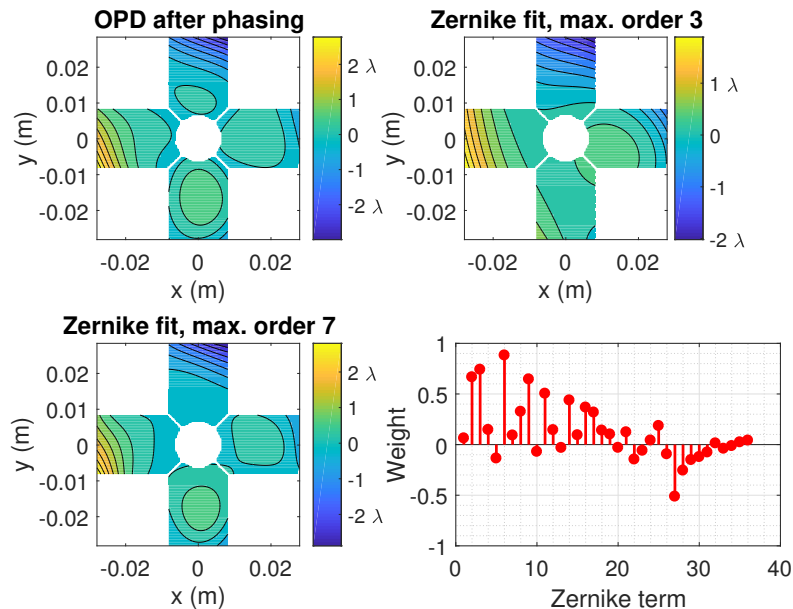
Figure 4.4: Top left: typical OPD (in wavelengths of 450 nm) in the exit pupil after phasing, but before drifts and stability effects are applied. Top right: a fit with Zernike polynomials up to the third order. Some local maxima are missing in the fitted WF. Bottom left: a fit with Zernike polynomials up to the seventh order. Local maxima can be seen in the fitted WF. Bottom right: weights of the normalized Zernike terms for achieving the seventh-order fit.

4.3. Sensitivity of Tolerance Budgets on the ACS Requirements

This section presents the results of a requirements sensitivity study carried out in FORTA. The goal of the study is to find how the OPD correction performance can influence the optical tolerances of the DST and vice versa: on one hand, the relaxation of optical tolerance budgets increases the required OPD correction capability over the entire telescope field of view. On the other hand, it reduces the stringent requirements on the deployment system elements, such as hinges, booms and the deployable baffle for thermal protection. Therefore, the sensitivity of the budgets can be found in this tolerance analysis.

The effects of the different coarse alignment and radius budgets are retrieved from a Monte-Carlo analysis in FORTA. Surface errors are excluded from the simulation, as these highly depend on the
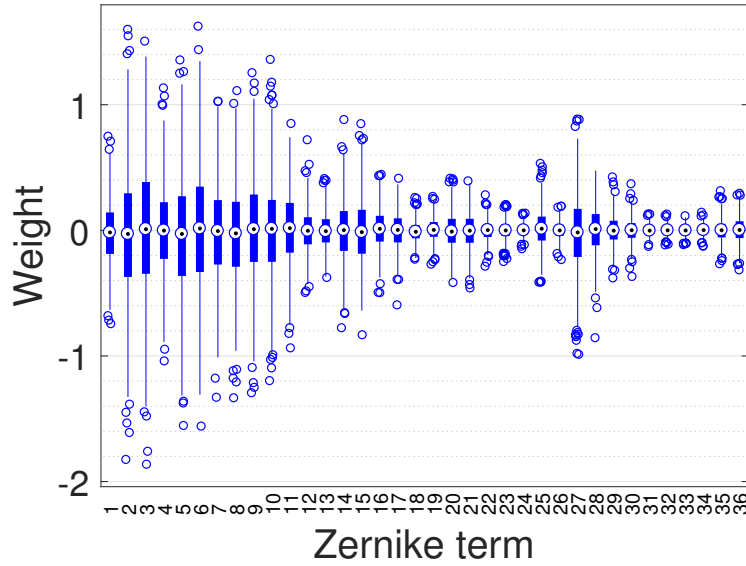
Figure 4.5: Boxplot of the distribution of relative weights of the first 36 Zernike terms in ANSI ordering, for a seventh-order fit of the exit pupil OPD, after phasing. The normalised radius of the Zernike polynomials is the minimum radius that contains all points on the pupil. One thousand trials are run in FORTA, with tolerances as shown in Table 4.1. The range of the vertical bars contains 50% of the datapoints, the range of the whiskers contains ca. 99.3% of the datapoints. Outliers are points beyond this range.

thermal environment in orbit and on the production processes of the mirrors. Furthermore, the computational cost of the FORTA ray tracing algorithm increases when the surface is approximated by e.g. Zernike polynomials.

4.3.1. Correlation between OPD and optical budgets

In the FORTA analysis, a Pearson correlation coefficient is calculated between the RMS OPD samples and the absolute values of the misalignments and radius errors. This correlation coefficient indicates the linear dependence of variables A and B. It is defined by

$$\rho\left(A, B\right) = \frac{1}{N-1} \sum_{i=1}^{N} \left(\overline{\frac{A_i - \mu_A}{\sigma_A}}\right)\left(\overline{\frac{B_i - \mu_B}{\sigma_B}}\right). \tag{4.1}$$

In this equation, N is the number of trials, μ is the sample mean, σ is the standard deviation of the data. When ρ is around zero, it indicates that there is little correlation between the two random variables, while values of ρ closer to -1 or 1 indicate a negative or positive linear correlation, respectively.

4.3.2. Simulation with original tolerance budgets

The coarse alignment budgets, given in Table 4.1 and obtained from Dolkens [6], are used for a first Monte-Carlo analysis of 500 trials. The results of the analysis are given in Figure 4.6. Here, subfigure (a) shows the correlation coefficients between the M1, M2 and M3 optical alignments and radii, versus the RMS OPD. It can be observed that the M2 radius budget has a correlation coefficient of 0.35 to the RMS OPD. This indicates that the effect of the M2 radius tolerance on the optical performance is relatively high. It is found from a decomposition into Zernike polynomials that this M2 radius error is mainly responsible for a significant defocus term.

Figure 4.6 (b) shows the distribution of the PV OPD and RMS OPD after phasing of the M1 segments. At a reference wavelength of $\lambda_0 = 450$ nm, the highest PV OPD is 18.2λ, and the mean PV OPD is 3.1λ. The highest RMS OPD is 3.7λ, and the mean RMS OPD is 0.7λ.

While the RMS OPD expresses the wavefront error in a single number, the maps in Figure 4.6 (c) show the actual OPD of sixteen random trials. The dominant circular fringe patterns that can be seen in

these maps support the finding that a large contribution of the OPD originates from the defocus terms caused by an error in the M2 radius.

From the above results, it is concluded that a reduction of the M2 radius tolerance allows for larger tolerances in the M2 and M3 positions and tilts. Adaptations in the M1 tolerance budgets are not considered at this stage, as these depend on the performance of the segment phasing algorithm, which is currently under development. The next subsection presents the results of an analysis with altered tolerances.

4.3.3. Simulation with adapted tolerance budgets

After three manual iterations, a new suggestion for the budgets is done. These are shown in Figure 4.7 (d). The M2 and M3 position, tilt and radius tolerances are increase by a factor three, apart from the M2 Z-position tolerance, which is kept constant, and the M2 radius tolerance, which is halved. The results of the analysis are given in Figure 4.7 (a, b, c).

Subfigure (a) shows the updated correlation coefficients between the M1, M2 and M3 optical alignments and radii, versus the RMS OPD. Since the M2 radius tolerance is halved, its defocus effect on the RMS OPD has decreased. In turn, the increase in M2 tolerances has resulted in a stronger effect on higher-order aberrations. Especially the errors in M2 X- and Y-axis tilt (α and β) have a correlation coefficient of above 0.15.

Figure 4.7 (b) shows the distribution of the PV OPD and RMS OPD after phasing of the M1 segments, at the central field of TDI 1. At a reference wavelength of $\lambda_0 = 450$ nm, the highest PV OPD is 19.8λ, and the mean PV OPD is 4.2λ. The highest RMS OPD is 4.16λ, and the mean RMS OPD is 0.75λ. So, with the new budgets, the simulated central field PV and RMS OPD distributions increased slightly for the main detector.

The maps in Figure 4.6(c) show the actual OPD of sixteen random trials. Due to the tightening of the M2 radius budget, the defocus terms from Figure 4.6(b) are less common. Instead, higher-order aberrations originate from M2 position and tilts, e.g. in the top-left OPD map.

For telescopes, normally the Rayleigh criterion must be met (eq. 3.2). From Smith [13, p. 376], it is found that a Strehl ratio of at least 0.80 is required to reach this criterion, and that this occurs for an RMS OPD of ca. $0.07\lambda_0$. Without compensation of the typical OPD in the DST instrument, the optical performance will be insufficient for high-resolution ground imaging purposes. For example, the best-case RMS OPD after phasing is $0.2\lambda_0$. This already results in a low Strehl ratio of 0.2, according to eq. 3.10. So, even in the best case, the wavefront corrector of the Aberration Correction System is essential to reduce the RMS OPD to at least the aforementioned $0.07\lambda_0$.

4.3.4. Conclusions from sensitivity study

It is decided to keep the tolerance budgets at their original value. Although the budget changes presented above given an interesting insight in the origin of aberrations, no accurate estimate for the mechanical tolerances is known at this point. Therefore, the tolerance budgets are not changed, until it is investigated what will be the effect on the mechanical design.

Besides this, an important note is that the results are strongly dependent on the optical field. The analysis presented here only holds for the central optical field of detector 1, while the optical performance at other fields may be more sensitive to certain budget changes. Therefore, this analysis can only be regarded as a preliminary study. More information and a map of the Strehl ratio on the focal plane of the DST w.r.t. the optical field can be found in [6].

Turning back to the original goal of this chapter, the next subsection treats the Aberration Correction System (ACS) requirements, as derived from the RDT in Figure 4.2, the problem analysis and the aberration severities found in this sensitivity study.

(a) Correlation coefficients of the RMS OPD and the absolute error of the design. α, β, γ denote rotations about the X,Y and Z-axes respectively, whereas R denotes the mirror radius.

(b) Histograms of PV OPD (left) and RMS OPD (right) after phasing of the M1 segments.

(c) Maps of the OPD in the exit pupil of the central field of TDI 1. M1 phasing has been applied. One fringe indicates a distance of 450 nm. The numbers top-left and bottom-left indicate the RMS and PV OPD (in wavelengths) respectively.

Element	**Position** (µm)			**Tilt** (µrad)			**Radius**
	X	Y	Z	X	Y	Z	(%)
M1	2	2	2	2	4	50	$1 \cdot 10^{-3}$
M2	15	15	10	100	100	100	$10 \cdot 10^{-3}$
M3	4	4	4	10	10	50	$1 \cdot 10^{-3}$

(d) Original coarse alignment and radius error budgets that are used as simulation input, from [6]. The budgets denote the two-sigma value of the zero-mean normal distribution that is used for error generation in FORTA.

Figure 4.6: Results of the initial coarse alignment budget analysis. All results shown are for the central field of the primary detector.

(a) Correlation coefficients of the RMS OPD and the absolute error of the design. α, β, γ denote rotations about the X,Y and Z-axes respectively, whereas R denotes the mirror radius.

(b) Histograms of PV OPD (left) and RMS OPD (right) after phasing of the M1 segments.

(c) Maps of the OPD in the exit pupil of the central field of TDI 1. M1 phasing has been applied. One fringe indicates a distance of 450 nm. The numbers top-left and bottom-left indicate the RMS and PV OPD (in wavelengths) respectively.

Element	Position (µm)			Tilt (µrad)			Radius (%)
	X	Y	Z	X	Y	Z	
M1	2	2	2	2	4	50	$1 \cdot 10^{-3}$
M2	45	45	10	300	300	300	$5 \cdot 10^{-3}$
M3	12	12	12	30	30	150	$3 \cdot 10^{-3}$

(d) Adapted coarse alignment and radius error budgets that are used as simulation input for the sensitivity study. The budgets denote the 2-sigma value of the zero-mean normal distribution that is used for error generation in FORTA. These budget changes are not implemented until more is known about their impact on the mechanical design.

Figure 4.7: Results of the Monte-Carlo simulation in FORTA after a change in the alignment and radius budgets.

4.4. ACS Requirements

The main functional requirement of the ACS is that it delivers diffraction-limited imagery on the DST. From this main function, the previous aberration analysis and the RDT in Figure 4.2, the requirements are derived. See Table 4.2.

Derivation of system requirements

For example, requirements ACS-OPT-01 and ACS-OPT-02 stem from RDT items T.1 and T.2 and refer to the image quality detection system. This system must be sufficiently accurate and sensitive to detect small improvements in optical quality for feedback control. Furthermore, ACS-OPT-01 to ACS-OPT-06 are functional requirements that follow from mission requirement MIS-REQ-07 and the existing telescope design for which the ACS is designed. For example, since the DST will observe Earth scenes, polychromatic and incoherent light will reach the detector [2]. Hence, the quality metric shall be applicable to this type of imagery and shall be sensitive over the expected range of aberration severities.

Digital restoration of the acquired imagery can be done via e.g. Wiener deconvolution when a PSF (or OTF) estimate is available [12]. However, wrong application of digital restoration theory could lead to image degradation. Therefore, functional requirement ACS-OPT-07 is introduced.

Finally, ACS-OPT-08 to ACS-OPT-08 refer to the qualities or non-functional optical requirements of the system. They include performance degradation and operational lifetime. Likewise, requirements ACS-STR-01 to ACS-STR-03, and ACS-ELE-01 specify the requirements on mass, volume and power consumption.

Deformable mirror optical requirements

From the OPD distributions of Figure 4.6 (b), 4.7 (b) and analysis with FORTA, it is found that failure of the M1 phasing step results in the outlier cases where the PV OPD is above 10λ and the RMS OPD above 2.5λ, see for example Figure 4.7 (c), bottom left. It is assumed here that the current budgets result in a maximum PV and RMS OPD of ca. 10 and 2λ respectively, since further development on this algorithm is ongoing[2].

For the required local deflection of the DM, it holds that $S(x,y) = -\frac{OPD(x,y)}{2}$. Hence, the PV and RMS deflection of the DM need to be $5\lambda_0 = 2.25\,\mu m$ and $1\lambda_0 = 0.45\,\mu m$ respectively. In case the coarse alignment tolerances remain fixed, the in-orbit drifts can be compensated with the remaining OPD correction capability of the OPD corrector. Hence, these numbers are taken into account during the conceptual and detailed design. See requirements ACS-OPT-03 and ACS-OPT-04.

---

[2]A few months after this analysis had been performed, improvements in the M1 phasing algorithm indeed increased the reliability, such that these outliers do not occur in current FORTA simulations.

Table 4.2: Requirements overview for the Aberration Correction System. MIS-REQ-07 is the main mission requirements from which the functional system requirements follow.

Identifier	Description	Function or Quality?
MIS-REQ-07	After calibration, the DST shall deliver images with diffraction-limited quality, meaning a Strehl ratio > 0.80 and an RMS OPD $< 0.07\lambda_0$ over the entire field-of-view, during the entire mission, in a space environment.	F
ACS-OPT-01	The ACS shall be able to detect an absolute change of 0.05 in the Strehl ratio, on at least 50% of the possible global ground scenes.	F
ACS-OPT-02	The ACS shall accept incoherent, polychromatic light from extended scenes and use this for optical quality assessment.	F
ACS-OPT-03	The ACS shall be able to detect and correct exit pupil aberrations with a peak-to-valley optical path difference of up to $10\lambda_0$ (4.5 µm)	F
ACS-OPT-04	The ACS shall be able to detect and correct exit pupil aberrations with a root-mean-square optical path difference of up to $2.0\lambda_0$ (900 nm)	F
ACS-OPT-05	The ACS shall be able to reduce an OPD with components up to the seventh Zernike order.	F
ACS-OPT-06	The ACS shall be able to remove the optical effects of the drifts defined in Table 4.1.	F
ACS-OPT-07	Post-processing restoration of the image shall not introduce detectable artefacts.	F
ACS-OPT-08	The ACS performance shall not degrade during assembly and transportation in the Earth, launch and space environments.	Q
ACS-OPT-09	The ACS operational lifetime shall be 2 yr.	Q
ACS-STR-01	The ACS shall fit within the existing optical design of the telescope.	Q
ACS-STR-02	The ACS mass shall be below 1.0 kg.	Q
ACS-STR-03	The ACS shall not increase the stowed volume of the DST.	Q
ACS-ELE-01	The ACS power consumption shall be below 10 W (Nominal) / 20 W (Max.).	Q

4.5. Functions and Architecture of the ACS

From the previous requirements section, some main functions for the ACS are derived. These are shown in the Function Breakdown Structure (FBS) in Figure 4.8. The three main branches of system functions are: 1) to detect an image quality deficit, 2) to convert this detected deficit into a control signal for the OPD corrector and 3) to actually correct the image via OPD correction and digital restoration. The required system elements are derived in the FBD as well, and these are used in Section 5.2 to generate system concepts. Note that the coloured blocks in the FBD refer to the corresponding Design Option Tree (DOT), found in the next chapter.
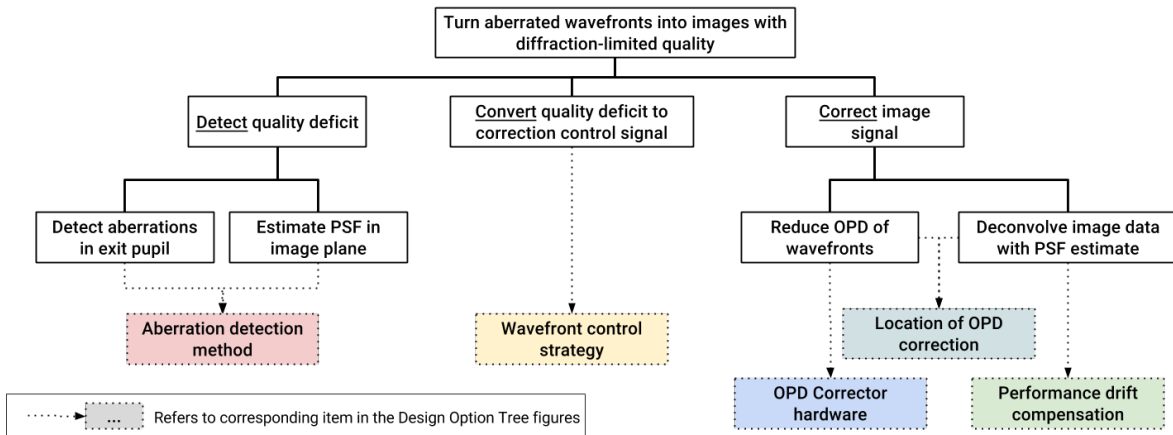
Figure 4.8: Function Breakdown Structure (FBS), from which the system elements are derived. See also the five Design Options Trees (DOTs) in the next five sections.

The functional elements of the ACS can be placed in a physical architecture that is based on existing adaptive optics and active optics system architectures, such as described in [7], [18, ch. 1] and [22, ch. 5]. Figure 4.9 shows this architecture, applied to the DST. It can be seen that an aberrated wavefront enters the system. An OPD corrector removes aberrations, such that a flat wavefront reaches the image sensor(s). The OPD corrector receives a control signal from a digital controller. This controller can receive two types of input. The first type is a direct wavefront estimate from an explicit wavefront sensor. The second type is an image quality metric from an implicit wavefront sensor, which can be the normal sensor used for acquiring imagery. In case an explicit sensor is used, a beam splitter must be placed in the optical train or a part of the optical field should be used to acquire an exit pupil image for this sensor.

There may be aberrations in the wavefront that have a modal frequency that is too high to correct with the OPD corrector. For this, digital restoration by a post-processing computer may correct the blurring effects of these high-order aberrations [3]. This computer can be situated in the spacecraft or on the ground.
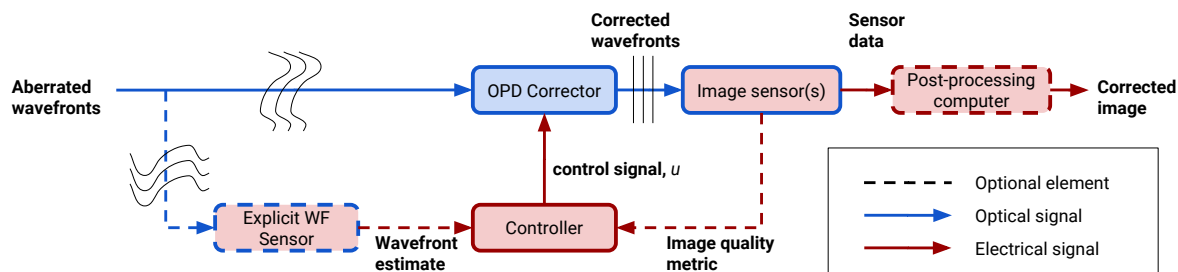
Figure 4.9: Signal flow in the Aberration Control System architecture. Blue represents optical elements and signals, red represents elements that work with digital data. Dashed lines indicate optional physical elements, depending on the choice of ACS concept.

Concepts for an Aberration Correction System

This chapter presents the generation and trade-off for five ACS concepts. The trade-off criteria are treated in Section 5.1. Subsequently, Sections 5.2 to 5.6 treat the design choices for each of the elements derived in Figure 4.8. The use of these elements as building blocks facilitates the generation of ACS concepts. Finally, Section 5.7 shows the generated concepts, which are evaluated in a trade-off in Section 5.8.

An overview of the interaction between these elements is shown in Figure 5.1. For example, the location of image correction cannot be chosen freely for a given type of OPD corrector: a deformable mirror can only effectively correct for all aberrations in one of the pupils of the system. Also, an implicit aberration detection method will limit the choices for the wavefront control strategy, while an explicit detection method may allow the use of all control strategies.

Aberration Correction System
Design Option Trees
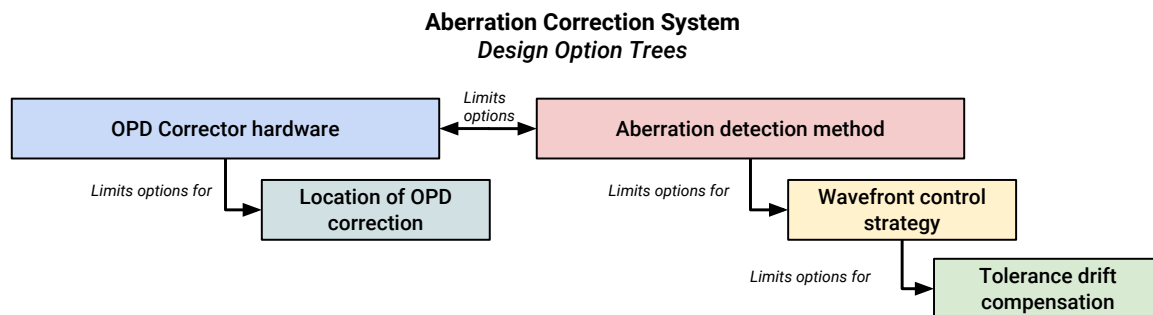
Figure 5.1: Interactions between the system elements, as deduced from Figure 4.8.

5.1. ACS Trade-off Criteria

The trade-off of the concepts at the end of this chapter are based on the criteria treated below. A distinction is made between primary trade-off criteria and secondary trade-off criteria. Primary criteria stem from the driving mission requirement of delivering diffraction-limited imagery, MIS-ACS-07. Secondary trade-off criteria do not directly affect image quality, but they do affect the feasibility of the full DST concept: these criteria are related to the qualitative requirements; see Table 4.2. The following trade-off criteria are considered:

1. **Initial misalignment and error compensation (primary)**
   The compensation of aberrations due to initial misalignments and surface errors is one of the primary tasks of the ACS. If the concept does not meet the aberration compensation requirements

stated in Chapter 4, the telescope will not meet its optical performance requirements. It will deliver imagery with a resolution and contrast that is insufficient for target applications.

2. **Drift compensation (primary)**
After correction of the initial misalignments, the system needs to actively compensate for changes in the OPD that arise from thermal deformations or effects such as out-gassing and material creep. The magnitude of the drift compensation requirements for the ACS are still TBD, depending on the location and magnitude of the drifts. These can be estimated when the thermo-mechanical design of the DST instrument advances. In any case, the drifts will cause an OPD change with a certain probability distribution and temporal behaviour that is linked to the orbital parameters of the satellite. Until they are better estimated, the budgets from Dolkens [6] are applied. These budgets cause a considerable performance drop to below the required optical performance, if they are not corrected. Hence, the drift compensation capability is one of the primary trade-off criteria of the ACS.

3. **Total mass of the spacecraft (secondary)**
A major objective of the DST design is to lower the total spacecraft mass for high-resolution Earth observation. Therefore, deployable, lightweight optical elements are implemented. An active optics system should enable the telescope to achieve diffraction-limited resolution without heavy structures. This means that the ACS mass is considered a secondary trade-off criterion.

4. **On-board power consumption (secondary)**
On-board power is always limited on a spacecraft. The first effect of an increase in on-board power consumption by the ACS is an increase of the energy dissipation in the telescope. The telescope will be heated with varying power, because the ACS duty cycle will vary over time. To prevent optical degradation due to power consumption variations, thermal housekeeping of the spacecraft will become more complicated. Secondly, the power generation subsystem of the spacecraft needs to increase in mass and size when more power is required, thereby partly undoing the benefits of a small, lightweight instrument design.These two reasons affect the ACS feasibility for the DST, but do not change optical performance directly. Therefore, the on-board power consumption is considered a secondary trade-off criterion.

5. **Cost (secondary)**
The lower mass and volume of the DST should result in a lower launch cost of the system. This will be partly undone by the increased cost of the ACS. The total cost of the ACS involves the development, production, testing, assembly, launch and operations of the system. For example, deformable mirrors are complicated and expensive components, particularly when they are not space qualified. When a custom design, a space qualification campaign or an alignment procedure are taken into account, the system costs will vary considerably between the concepts. To support the low-cost DST concept, cost is considered a secondary trade-off criterion.

6. **Risk (secondary)**
The novelty of an active optics system for space applications is linked to a low spaceflight TRL for the system components. This means that the risk of mission failure increases when more new system elements are combined. Although risk can be reduced with an increase in costs for research and testing, this is not considered feasible for all risks within the scope of the DST project at this stage. Therefore, risk is considered a secondary trade-off criterion.

7. **Interruption of scanning operations (secondary)**
Even when an aberration correction system can deliver the sufficient optical performance during normal push-broom-like scanning operations, it may require a fixed ground scene or astronomical point source to update the aberration estimate every few minutes. In such a case, the scanning operations need to be interrupted to actively track one target while the spacecraft is orbiting the Earth. This interrupts normal scanning operations, leading to a loss in valuable observation time. Therefore, the worth of the DST decreases when it has to interrupt push-broom scanning. So, the amount of time that the ACS interrupts normal operations is a relevant secondary trade-off criterion.

5.2. OPD Corrector Design Options

This section elaborates on the OPD corrector options, given in the first Design Option Tree (DOT) in Figure 5.2. The *OPD corrector hardware* is the set of physical components that enable the reduction of the OPD in the optical system. Different types of hardware do exist that can change the OPD in a controlled way. See Figure 5.2. The following subsections treat these OPD corrector types.
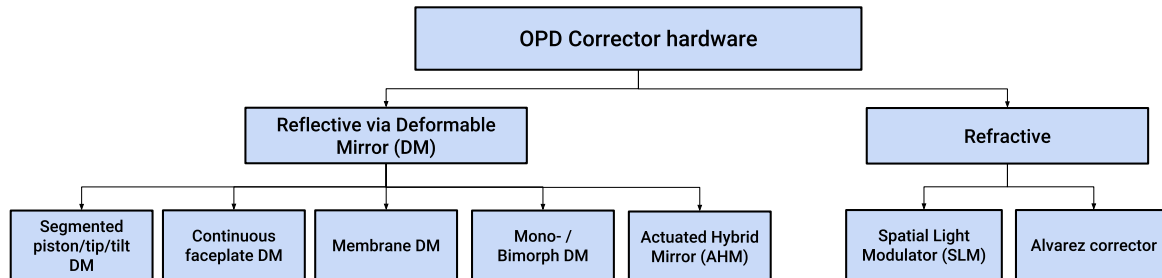
Figure 5.2: DOT for OPD corrector design options.

5.2.1. Segmented correctors

Segmented deformable mirrors currently exists in two varieties. The most simple variant is the piston DM or piston segmented corrector. It works by introducing relative piston changes at different locations in a wavefront, as shown in Figure 5.3 (left). The piston DM is simple in design, but introduces discontinuities in the OPD and does not allow to correct for global wavefront tilt. Furthermore, the discontinuous wavefronts reflecting from such a DM will suffer from diffraction, reducing the optical quality of the system. Finally, piston errors between the M1 segments are already removed in the M1 phasing step. The residual wavefront aberrations will thus originate from higher-order misalignments in the optical system, requiring a wavefront corrector than can smoothly correct for higher order aberrations.

Piston/tip/tilt segmented mirrors can partly solve the discontinuous wavefront correction with two extra degrees of freedom, illustrated in Figure 5.3 (middle). Piston/tip/tilt mirrors based on MEMS technology are developed by Iris AO[1]. Amongst others, they offer a segmented mirror with 163 piston/-tip/tilt segments and 8 μm stroke per actuator. The MEMS actuators are relatively small and low-cost, making it possible to place many piston/tip/tilt segments in a small aperture. This advantage allows the MEMS segmented corrector to have a high actuator density, leading to performance comparable to existing continuous mirrors [23]. However, again, care must be taken that the edges between the segments do not cause optical deterioration by introducing extra diffraction.

Loktev et al. [24] show that a DM consisting of discrete piston segments has a residual correction error of at least 22% of the total wavefront variation. Doble et al. [25] compare the piston-only segmented corrector with a piston/tip/tilt segmented corrector and a continuous deformable mirror. They show that, for a given Strehl ratio, the piston-only corrector requires ca. seven times more actuators than the continuous mirror. In the same research, the segmented corrector with piston/tip/tilt segments performs slightly worse than the continuous DM for a given number of actuators.

From the above, it is concluded that segmented correctors with only a piston degree of freedom are considered impractical for application to the Aberration Correction System. However, segmented correctors with MEMS piston/tip/tilt actuators may be competitive to other wavefront correctors, when the number of actuators is sufficiently high and diffraction effects can be limited. However, due to their limited aperture size, discussion with Iris AO should point out if it is possible to up-scale the MEMS DMs in the future.

5.2.2. Continuous plate DM

The continuous face sheet DM with push-pull actuators (abbreviated PDM) consists of a single plate of material, deformed by actuators that are in direct contact with the sheet and exert a force perpendicular to it, as illustrated in Figure 5.3 (right). The PDM can be designed with different types, strokes and

---

[1]http://www.irisao.com, retrieved 3-7-2017
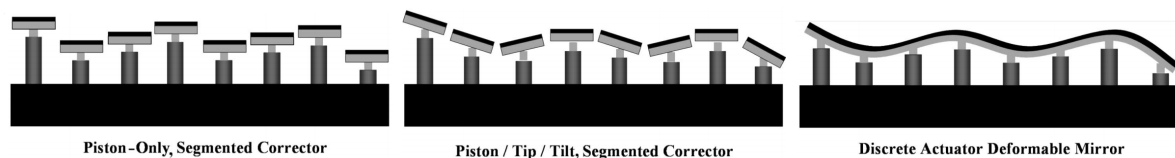
Figure 5.3: Working principle of continuous, piston and piston/tip/tilt wavefront correctors. The last two have worse performance than the continuous corrector. From [25].

configurations of actuators. Besides this, the dimensions and material of the face plate can be optimised for the application of interest. The continuous plate is supported by actuators, such that the edge of the mirror need not be fixed. This allows for a larger effective correction area on the PDM than on the membrane or monomorph DM, as shown in Loktev et al. [24].

Existing examples of plate DMs are piezoelectric DMs from OKO Technologies[2], "surface-normal" mirrors from AOA Xinetics[3], the E-ELT Adaptive Mirror M4 from Microgate[4] and mirrors from CILAS[5]. Furthermore, academic research is done on the design of a low-order PDM for space application by Laslandes et al. [10].

A wide range of actuators can be used on continuous plate DMs: piezoelectric actuators and electrostrictive actuators [26], voice coil actuators [27], variable reluctance actuators [28] and thermal actuators [29]. It is expected that a PDM can be selected or developed for the Aberration Correction System, because many materials and actuator types can be applied. To evaluate the performance of PDM designs, a model has been made for use in the FORTA software. See Section 6.1 for details on this model.

Existing PDMs that may fulfil the ACS requirements are the *SAM* mirrors from CILAS, mirrors in the surface-normal series from Xinetics and the electromagnetic mirror being developed at TNO for space applications [30].

5.2.3. Membrane DM

A membrane DM consists of a membrane under tension, coated with reflective material. A conventional membrane DM works with electrostatic actuators that can exert a pulling force on the membrane, thereby deforming the surface. Membrane DMs are manufactured by (amongst others) Boston Micromachines[6] and OKO Technologies[7].

For application to the DST design, the most relevant differences between the membrane DM and the PDM discussed before, is the mirror edge. For the first type, the membrane must be kept under a uniform tension. This requires the edge of the membrane to be fixed [24]. On the other hand, it can be seen in Figure 4.4 that the outer edge of the cross-shaped exit pupil typically suffers from the highest OPD. This is caused by the optical design and phasing method described by Dolkens [6]. To be able to deform the extremes of the exit pupil light, the membrane must be larger than the actual pupil. According to Vdovin [31], the size of the light beam reflecting on the membrane surface should be maximum 50% of the total membrane area to account for the inability of the regions near the edge to move. This area ratio corresponds to a membrane/pupil ratio of $1.4/1$.

In case of the DST optical design, the exit pupil diameter is 60 mm. This means that the minimum membrane diameter is ca. $60 \cdot 1.4 = 84$ mm, such that at least 12 mm extra radius is required around the exit pupil. However, it can be seen in Figure 5.4 that only 14 mm is available for the DM above the exit pupil, including support structure for the membrane and actuators. So, it may not be possible to use a membrane DM because of dimensioning limitations. Adapting the telescope design to create more space for the DM is possible, but this results in sub-optimal optical performance according to simulations in FORTA. The high diameter of the membrane DM is not the only disadvantage: because the electrostatic actuators can only exert a pulling force on the membrane, a bias deformation is requi-

---

[2]http://www.okotech.com/pdm, retrieved 3-7-2017
[3]http://www.northropgrumman.com/BusinessVentures/AOAXinetics/IntelligentOptics/Products/
  Pages/SurfaceNormalMirrors.aspx, retrieved 3-7-2017
[4]http://www.microgate.it/Engineering/Adaptive-Deformable-Mirrors, retrieved 3-7-2017
[5]https://www.cilas.com/en/adaptive-mirrors, retrieved 3-7-2017
[6]http://www.bostonmicromachines.com/deformable-mirrors.html, retrieved 6-7-2017
[7]http://www.okotech.com/mmdm, retrieved 6-7-2017
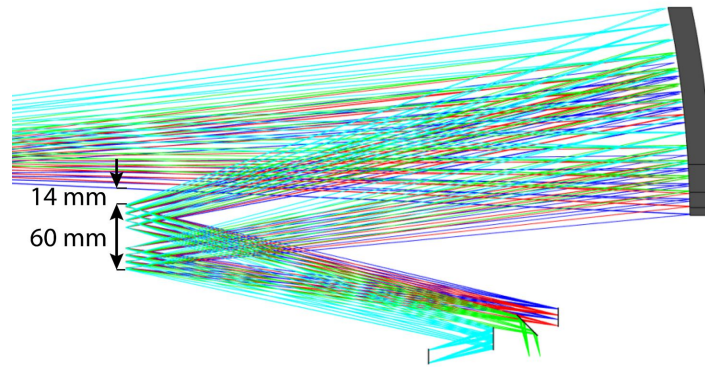
Figure 5.4: Exit pupil size and available space for the deformable mirror in the DST design.

red to allow for bi-directional aberration correction, such that the membrane becomes concave. This introduces a static defocus aberration that needs to be counteracted by an extra lens or mirror [18]. However, extra optical components are undesired in the instrument design: a lens behind the DM will introduce chromatic aberration, while an extra mirror after the DM increases the complexity and size of the telescope.

However, an advantage of membrane-type DM is that their low surface and actuator mass makes them more robust against shock loads than PDM type mirrors [32], so that they are more suitable for launch in a rocket that experiences high accelerations and separation shocks.

Ultimately, because of the two disadvantages (dimensioning and bias defocus), application of a membrane DM is currently not considered as a feasible solution for wavefront control. However, in case other wavefront correctors are found to under-perform later in the design project, a model of the membrane DM can be made using the Poisson equation described in [18, Sec. 6.4] with the finite difference method described in [33].[8]

5.2.4. Mono- and bimorph DM

Monomorph (or unimorph) deformable mirrors (MDMs) and bimorph deformable mirrors have actuation that runs parallel to the mirror surface, instead of the perpendicular push-pull actuation found on PDMs. Bending of the mirror surface is controlled by the in-plane expansion and contraction of one piezoelectric layer in a monomorph mirror, and of two piezoelectric layers with opposite polarity for bimorph mirrors [34], see Figure 5.5. The required electric field is applied by a pattern of high-voltage electrodes and a ground plane, in between which the piezo material is placed.
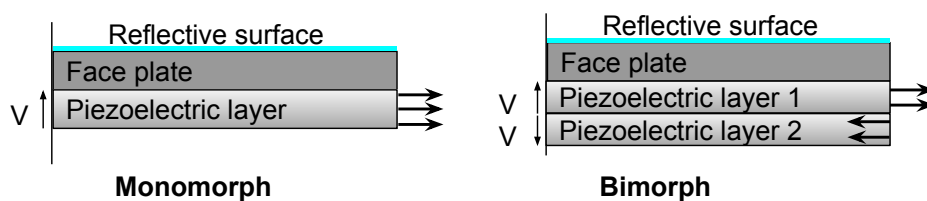
Figure 5.5: Working principle of mono- and bimorph deformable mirrors. The piezoelectric material layer contracts or expands under an applied voltage, resulting in a curvature of the surface. For monomorph mirrors, a stiff faceplate or substrate is required to allow for reaction forces. In bimorph mirrors, the two active layers are given an opposite polarity, so that a lower reaction force is present in the substrate or faceplate, at the cost of an increased number of electrodes.

The deformations in mono- and bimorph mirrors are governed by the Poisson equation, just as is the case for the membrane mirror [24]. However, while the membrane DM needs to be supported at its edges, mono- and bimorph mirrors can be supported by a central support structure in the central "hole" of the telescope pupil [35]. Therefore, the edges are free to move, such that the mono- or bimorph

---

[8]A start has been made with this model in MATLAB, but the development was halted when the disadvantages of a membrane DM for the ACS were found.

mirror can be smaller than the membrane DM described before. Manufacturers of mono- and bimorph mirrors include AKA Optics[9] and CILAS[10].

The CILAS *MONO* series features MDMs with up to 200 electrodes. The mirror can be seen in Figure 5.6. This enables the compensation of Zernike terms up to 10th order on mirrors with a diameter up to 250 mm. According to this company, these mirrors are suitable for use in space [36]. More details on the space qualification campaign are given by Rausch, Verpoort and Wittrock, who tested a mirror based on technology from CILAS with support from the European Space Agency [37]. This mirror features 44 actuators and a 50 mm aperture. It was found that only a Z-axis random vibration test is too severe for this mirror, but that this can be solved by increasing the frequency of the first eigenmode of the surface.

A disadvantage of the piezoelectric materials involved, is that high voltages need to be generated in the spacecraft [26]. This can lead to electro-static discharges and other damaging effects [38, p. 529]. Furthermore, application to the cross-shaped exit pupil of the off-axis DST design is likely to require a custom electrode layout, with respect to those that are already on the market: existing DM are mainly used in circular pupils and optimised for high strokes at a low-order aberration compensation.

5.2.5. Actuated hybrid mirror

The Actuated Hybrid Mirror (AHM) concept has been developed to make it possible to actively control the surface shape of large (space) telescope primary mirrors. The AHM concept integrates different surface normal and surface parallel actuator types into a one-meter-sized mirror to achieve maximum control over a wide range of amplitudes and spatial frequencies [8]. A high surface quality for these mirrors has been achieved without difficulty, but developments have not been published after 2010 [39].

Patterson and Pellegrino have proposed an adaptation of the AHM concept without the backing structure and surface-normal actuators [40]. These so-called ultralightweight deformable mirrors for space applications have been under development at Caltech[11]. An illustration of this large monomorph type of mirror can be seen in Figure 5.7.

Figure 5.6: Commercially available monomorph mirror (MDM) *MONO63* from CILAS.
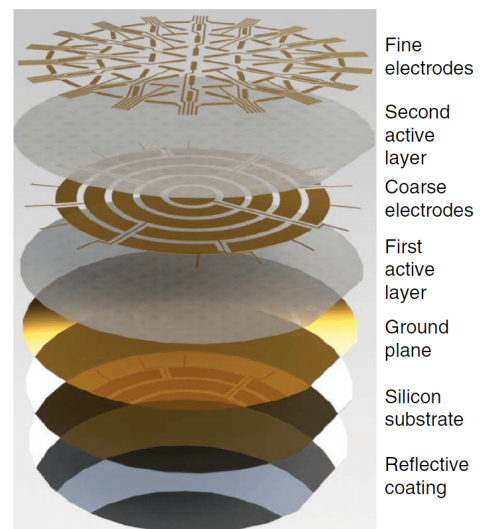
Figure 5.7: Ultra-lightweight MDM with two active layers for coarse and fine control [11].

Fine electrodes

Second active layer

Coarse electrodes

First active layer

Ground plane

Silicon substrate

Reflective coating

OPD corrections in the entrance pupil (i.e. the primary mirror) require large deformable structures, with several hundreds of actuators [8, Fig. 8]. When aberration correction is done in the smaller exit pupil, the thermo-mechanical environment can be more controlled. Also, correction in M1 makes the deployable system more complex. As mentioned before, the TRL of the mirrors described above is low: no academic or commercial party can currently be found that still develops these mirrors, and no shock and vibration test documentation is available. Given the large and thin surfaces of the AHM and

[9]http://www.akaoptics.com/bdm.php, retrieved 3-7-2017
[10]https://www.cilas.com/en/adaptive-mirrors, retrieved 3-7-2017
[11]http://www.pellegrino.caltech.edu/thin-active-mirrors, retrieved 8-7-2017

ultralightweight DMs, the launch environment can pose a serious risk. It is outside the scope of the DST project to continue the development of this new type of mirror. Therefore, unless new developments are initiated by other parties, they are not applicable to the conceptual design of the ACS.

5.2.6. Spatial light modulator

On the right-hand side of the OPD corrector DOT in Figure 5.2, a branch of refractive OPD corrector concepts can be seen. All the reflective correctors, discussed above, change the OPD by moving their reflective surface over a physical distance. Refractive correctors, however, can also change the OPD by increasing the refractive index. This is done in the Spatial Light Modulator (SLM).

Liquid Crystal SLM technology is based on the birefringent nature of liquid crystals. This means that the refractive index of the crystals depends on the polarization of the entering light. A locally applied electric field changes the orientation of the crystals in the SLM, so that the refractive index can be controlled. SLM devices can make use of transmissive or reflective screens.

The SLM has the advantage that a very high spatial resolution can be achieved, for example the 10 megapixel SLM promoted by Holoeye[12]. However, a major disadvantage for the use of SLMs in the DST is that the SLM is sensitive to polarised light only, meaning that most of the signal to the detector is lost. Furthermore, because the SLM is a refractive element, its optical path length will be different for different wavelengths, hence introducing chromatic aberration. Finally, the maximum OPD that can be achieved is in the order of 2λ. This is insufficient for the expected exit pupil OPD. Therefore, aberration correction with an SLM is not feasible in the DST.

5.2.7. Alvarez corrector

The second class of refractive correctors is the Alvarez corrector. This type of corrector consists of a set of optical elements that can be moved relative to each other to provide aberration compensation. Its design requires that the relative amplitudes of the aberrations are known beforehand [41], which is not the case for the DST optical system. Besides this, since Alvarez correctors consist of refractive elements, the introduction of chromatic aberration cannot be avoided. This is why existing devices are especially used in laser systems. Due to this, the Alvarez corrector is not considered feasible for application in the aberration correction system of the DST.

5.2.8. Overview of wavefront corrector options

As stated before, there are no resources in the DST project that allow the development of a new DM technology. Therefore, commercially available mirrors are sought that can fulfil the requirements from Chapter 4 without many adaptations. Given this constraint, not all DM manufacturers could offer a mirror suitable for the DST.

For example, *Boston Micromachines* does not manufacture mirrors with a pupil size larger than 25 mm. Options have been discussed where multiple mirrors are combined to create the DST exit pupil size and shape. However, during discussion with the manufacturer it has been found that a multi-mirror configuration cannot completely fill the pupil. It also requires expensive adaptations to the fabrication of products. The same holds for *Iris AO*, *Adaptica* and *Imagine Optic*, which cannot produce apertures above 20 mm with their current designs and production technologies. This has been concluded from correspondence with these parties.

Another manufacturer, the *Microgate* company, is only specialised in large deformable secondary mirrors for ground-based telescopes, based on voice-coil technology and capacitive sensors. They offer no products that are in the DST design range.

The remaining manufacturers have been contacted and design options have been discussed. Table 5.1 shows the properties of most suitable deformable mirrors that are found to be available from this discussion. Companies that offer mirrors with a maximum pupil size of 50 mm are also considered, because the optical design of the DST can still be slightly adapted in the future.

Interestingly, the mirrors that are selected are based on different conceptual designs. Alpao offers mirrors with a membrane and electromagnetic coil actuators, normal to the surface. In that sense they are a mix between the PDM (explained in Subsection 5.2.2) and the membrane DM (explained in

---

[12]https://holoeye.com/spatial-light-modulators/gaea-4k-phase-only-spatial-light-modulator, retrieved 3-7-2017

Subsection 5.2.3). Also interesting is CILAS, which offers monomorph mirrors that have been tested for space qualification in cooperation with ESA [37].

Note that the row showing mirror strokes shows the maximum inter-actuator stroke. It does not take into account that mono- and bimorph mirrors have a lower stroke for higher-order corrections, due to the curvature-changing nature of the actuators.

Table 5.1: Overview of most suitable commercially available DMs for the DST. For each manufacturer, the pupil size that is closest to 60 mm diameter is selected. Most manufacturers can offer a customised pupil shape and actuator configuration for additional cost. CILAS and TNO have developed mirrors for space-based applications, but this does exclude other mirrors from becoming space qualified in the future.

Manufacturer	Alpao[1]	CILAS[2]	AKA[3]	TNO[4]	Xinetics[5]	OKO[6]
Surface	Membrane	Monomorph	Bimorph	Plate	Plate	Plate
Actuator type	EM coil	Piezo	Piezo	EM coil	Piezo	Piezo
Pupil (mm)	50	60	65	TBD	60	50
Housing (mm)[7]	70	TBD	88	TBD	88	TBD
Actuator count	97	TBD	48	TBD	97[8]	79[9]
Space TRL[10]	4	7	4	5	4	4
IA Stroke (μm)[11]	5	3	1	12	4	2
PV Stroke (μm)[12]	80	60	2	46	10	8
Quality (nm)[13]	7	<10	6	TBD	13	TBD

[1]www.alpao.com, [2]www.cilas.com, [3]www.akaoptics.com, [4]www.tno.nl,
[5]www.northropgrumman.com/BusinessVentures/AOAXinetics, [6]www.okotech.com
[7]smallest dimension in mirror plane. See Figure 5.4.
[8]Other option: 37 actuators, [9]Other options: 37, 69, 109 actuators
[10]Technology Readiness Level, estimated using ISO standard 16290 and manufacturer data.
[11]Maximum inter-actuator stroke given by manufacturer, [12]Maximum peak-to-valley stroke given by manufacturer.
[13]RMS Optical quality when the system is placed in closed-loop control.

(a) AKA Optics   (b) AOA Xinetics   (c) TNO [30]

(d) CILAS   (e) Alpao   (f) OKO Flexible Optical
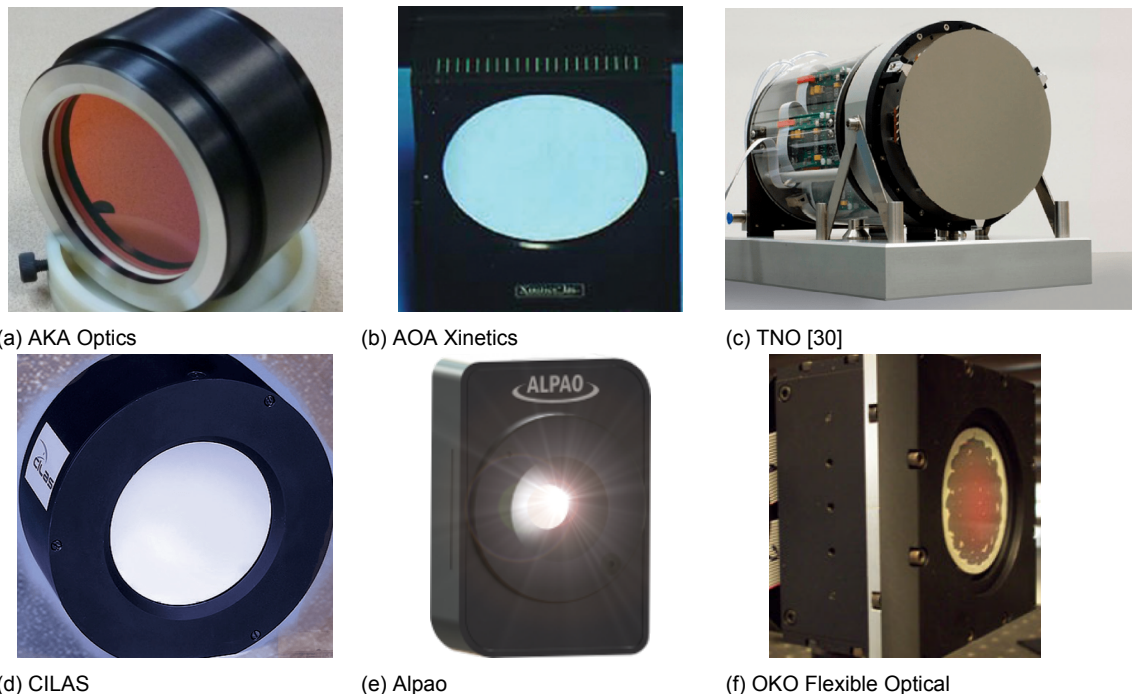
Figure 5.8: Deformable mirrors from different manufacturers, corresponding with the mirror technologies in Table 5.1. Retrieved from manufacturer's websites given below Table 5.1.

5.3. Location of Correction Design Options

The second DOT treated here is shown in Figure 5.9 and treats the *Location of OPD correction*. "Location" is considered here in the broadest sense: it can be a physical location for OPD correction (left DOT branch) or the location where image corrections are performed on digital data (right DOT branch). Design options from both branches can be combined, depending on whether physical and/or digital aberration correction is implemented. The following subsections treat the options shown in the Location of Correction DOT.
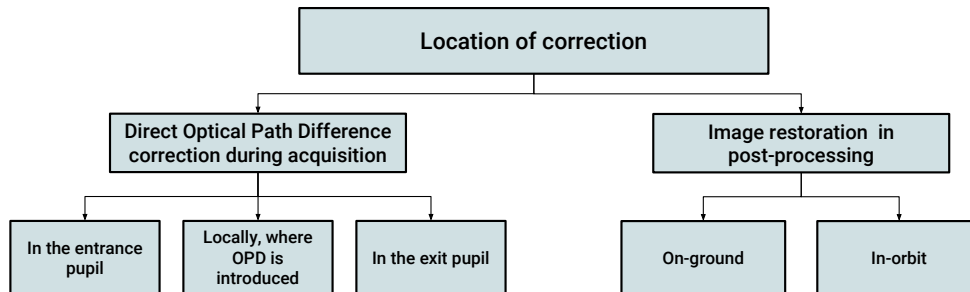
Figure 5.9: DOT for location of OPD correction design options.

5.3.1. OPD correction in the entrance pupil

The entrance pupil of the telescope is the primary mirror (M1). The aberrations that can theoretically be corrected in the entrance and exit pupil are the same, since the exit pupil is an image of the entrance pupil. The main difference is the dimension of the OPD corrector in the entrance pupil: while the exit pupil has a diameter of 60 mm, it is 1500 mm for the entrance pupil. Furthermore, the segments of M1 are not deployed in stowed configuration. This means that OPD correctors in the entrance pupil have large and deployable structural elements as well. The Actuated Hybrid Mirror (AHM) technology discussed in Subsection 5.2.5 has specifically been developed to provide OPD corrections in the entrance pupil.

5.3.2. OPD correction at location of introduction

The following example explains the origin of field-dependent aberrations. In Figure 5.10, two rays from different fields have been highlighted (pink and black). While both rays reflect on the same surface location of M1 and of the exit pupil mirror, they encounter a different surface point in M2 and M3. This indicates that an OPD that is introduced at M1 may be corrected for all fields in the exit pupil mirror. However, when a (thermal) deformation in M2 or M3 introduces a local OPD to one ray, the other ray has have a different OPD due to the different location of reflection. In that case, an OPD corrector in the entrance pupil or exit pupil cannot fully restore the wavefront of all optical fields at the same time. This means that M2 and M3 can introduce field-dependent aberrations [42], even when the ACS is active.

Theoretically, a logical way to compensate the locally introduced OPD is to put an OPD corrector at the location of M1, M2 and M3. This allows for full control over the three optical surfaces that form the off-axis telescope. However, in practice, such a system requires many parallel control systems, all with sensors and actuators. This dramatically increases the complexity and development costs of the space telescope and is therefore considered infeasible.

5.3.3. OPD correction in the exit pupil

To evaluate whether corrections in the entrance or exit pupil are sufficient, or whether local corrections in M2 and M3 are required, 25 optical simulations are performed with an idealised wavefront corrector in the exit pupil. The expected two-sigma optical tolerances from Table 4.1 are applied to the system and the resulting optical properties are compared. The idealised wavefront corrector consists of a continuous plate DM with a 10 × 10 actuator grid on a square mirror with 60 mm side length and a 0.8 mm aluminium face sheet. It is modelled following the equations described Section 6.1. The mirror is ideal in the sense that no actuator stroke limitations are applied, and that perfect control is assumed
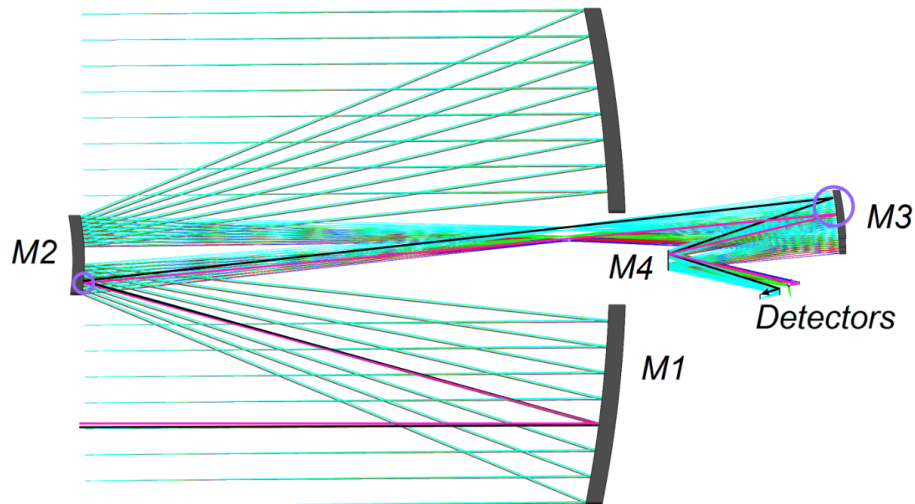
Figure 5.10: Field-dependent aberrations can be introduced by M2 and M3 when wavefront correction is performed in the entrance pupil (M1) or exit pupil (M4).

to achieve the least-squares fit of the mirror to the required deformation. The actuator stiffness is set to $2\,\mathrm{N}\,\mu\mathrm{m}^{-1}$.

Although the number of trials for this Monte-Carlo simulation does not yield statistically significant results, it gives a general idea on whether a DM in the exit pupil can help with achieving diffraction-limited imagery over the entire field-of-view. Table 5.2 shows the outcome of this small experiment.

Firstly, it can be seen that there is a variation in the optical performance over the FOV, which in accordance with the Strehl ratio map by Dolkens [6]. For this experiment, the mirror is controlled to minimise the OPD of the sharpness sensor, which is closest to the spectral channels. See Figure 5.11. As a result of this, the central field of the spectral channels has the highest optical performance, with 24 out of 25 simulations giving a Strehl ratio above 0.95.

Regarding main system requirement DST-MIS-07 in Table 4.2, it can be observed in the table that the Strehl ratio is indeed above 0.8 for most of the simulations. However, at the outer field of TDI-1, 6 out of 25 trials resulted in a Strehl ratio below 0.8, compared to 1 out of 25 for the central field. The minimum Strehl ratio is even below 0.7. This means that field-dependent aberrations play a large role in the telescope performance, up to the extent that they may cause a violation of the Strehl ratio requirements. Therefore, field-dependent effects shall be taken into account during detailed design at all times.

Finally, it must be noted that the exit pupil DM does indeed help, as the mean Strehl ratio on TDI-1 is brought from 0.16 to 0.93. The worst-case Strehl ratio on TDI-1 is 0.68, while this was 0.10 before DM application. Hence, the use of an exit pupil DM definitely has potential for the aberration correction system.

Table 5.2: Exit pupil wavefront correction performance, for a least-squares fit of the preliminary PDM model to the desired exit pupil deformation. The results are obtained with the simulation of a square DM with 60 mm sides, a rectangular pattern of 10 × 10 actuators, and aluminium face sheet material of 0.8 mm thickness.

Sensor (field)	TDI 1 (0, 0)	TDI 1 (0.3, 0)	Spectral (0, 0)	Spectral (0.3, 0)	Spectral (0.3, 0.06)
Max. Strehl	0.97	0.98	0.99	0.94	0.94
Mean Strehl	0.93	0.89	0.98	0.89	0.87
Min. Strehl	0.68	0.67	0.88	0.78	0.72
No. trials > 0.8	24/25	19/25	25/25	23/25	20/25
No. trials > 0.9	22/25	15/25	24/25	16/25	10/25
No. trials > 0.95	12/25	8/25	24/25	0/25	0 /25
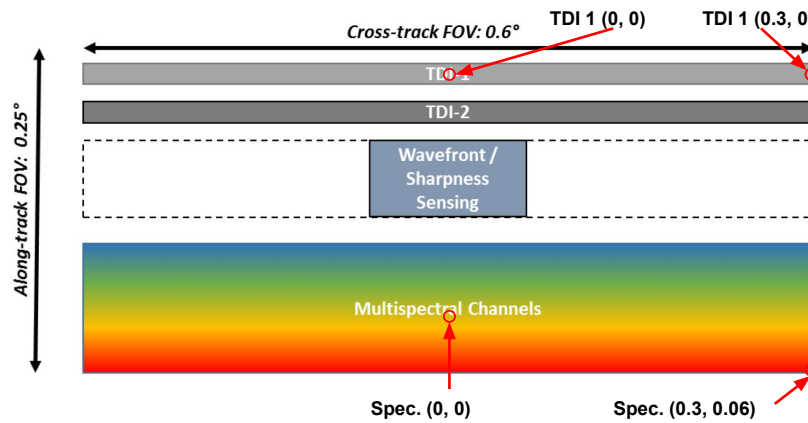
Figure 5.11: Indication of fields on FPA. Strehl ratios in Table 5.2 are calculated for the FPA locations indicated in this figure.

5.3.4. On-ground versus in-orbit image restoration

When images are acquired with a system that suffers from aberrations, image restoration techniques can be applied. The effect of aberrations on the image can be partly undone by e.g. Wiener deconvolution of the image with the PSF of the system [16]. The PSF can be estimated using different techniques, such as phase diversity [43].

When images are restored on-ground, the PSF estimation and deconvolution can be executed on ground-based computers. When processing is done in-orbit, the computer could take up a significant part of the telescope mass and power budgets. However, a disadvantage of on-ground processing is that more data needs to be transmitted: in case of phase diversity, the raw output of two TDI detectors needs to be transmitted, instead of the processed output figure that results from the image restoration process.

Instead of a microprocessor, an on-board Field Programmable Gate Array (FPGA) may be used for this real-time image deconvolution [44]. FPGA's have a configurable logic behaviour and many parallel input/output ports, so that custom operations can be implemented in a highly parallel way. Therefore, an FPGA can increase the deconvolution speed of the aberrated imagery.

5.4. Aberration Detection Method Options

The *Aberration detection method* covers the process that relates the collected light to the estimated aberrations. To detect aberrations, the wavefront phase of the incoming light needs to be estimated. Both explicit and implicit wavefront detection methods exist, see the Design Option Tree in Figure 5.12 and the ACS architecture in Figure 4.9.
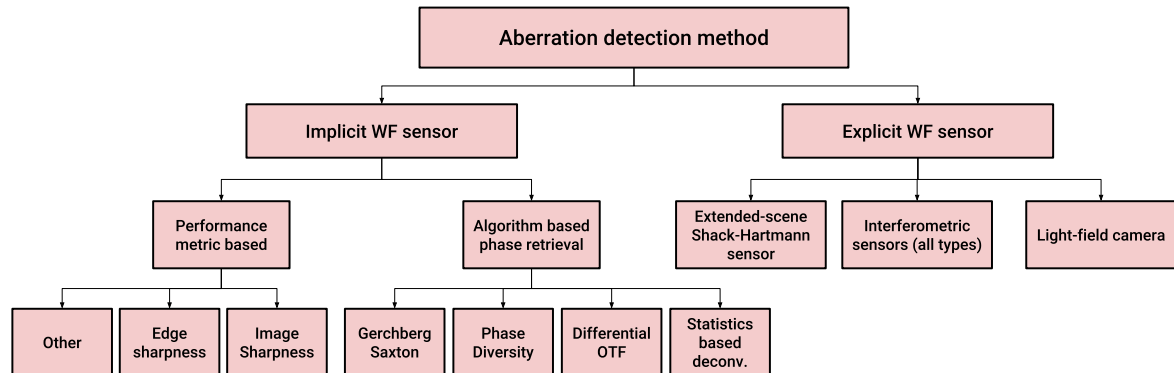
Figure 5.12: DOT for Aberration Detection Method options.

This section firstly treats the implicit detection methods and secondly the explicit detection methods. Implicit methods rely on image sensor data only. They use an image performance metric or algorithm to estimate the aberration that produces the acquired image. On the other hand, explicit methods use a dedicated non-imaging wavefront sensor. These types of wavefront sensors have been in use for more than twenty years in military and astronomical applications [7].

5.4.1. Implicit sensor: performance metric based

An intuitive method to find and minimise the aberrations consists of optimising the image quality. Rather than explicitly deriving the wavefront phase error and deforming the DM to remove it, the system directly controls the DM until some metric is maximised. The control algorithms behind this implicit DM control are given in Section 5.5.

Different performance metrics can be implemented, but all of these need to fulfil at least two conditions: firstly, the metric must have a maximum value when the aberrations are zero. Secondly, the metric must be convex around the zero-aberration condition, such that optimisation algorithms can converge [18].

Additionally, when a performance metric cannot work with extended scene image data, the DST will need to point at a star to obtain a PSF image. This manoeuvre hinders normal operations and may introduce additional aberrations, because re-orientation of the spacecraft will change the thermal environment of the telescope. Therefore, a third requirement on the image metric is that it can work with extended scene image data. On top of this, metrics that can work with low-contrast ground image data are preferred above those that can only work with high-contrast scenes.

Image sharpness

The image sharpness metric, f_{power}, is found by computing the sum of the pixel intensities to a given even power p [18]. The general sharpness metric also includes a weighting factor w [45] and can be written as:

$$f_{power} = \sum_{n=1}^{N} w_n i_n{}^p \tag{5.1}$$

Where w_n is a weighting factor for pixel n and i_n is the image intensity at pixel n. Normally, $w_n = 1$ and $p = 2$ [45]. When the object does not change, maximisation of the sharpness leads to maximum contrast in the image. This is related to the zero-aberration condition. Sharpness metrics have been studied for over forty years [46], as they are relatively robust and easy to implement.

Edge sharpness

Contrary to image sharpness, which relies on the sum of pixel intensities, the edge sharpness criterion calculates the local intensity derivative in the spatial coordinates of the image:

$$f_{edge-sharpness} = \frac{\sum_{n,m} \left(i_{n+1,m} - i_{n,m}\right)^2 + \left(i_{n,m+1} - i_{n,m}\right)^2}{\sum_{n,m} i_{n,m}} \tag{5.2}$$

it has been proven by Muller and Buffington [46] that this metric reaches its absolute maximum when the image is fully restored. The metric may be suitable for the extended scenes captured by the DST, since it uses all information in the image and is intuitively related to the image quality. The metric may also be combined with the *power* sharpness criterion.

High-frequency Fourier content

From Fourier optics, it is known that the MTF of a system is maximum over the spatial frequency range when the system is diffraction-limited. When aberrations are introduced, the high-frequency MTF shows the largest relative decrease. Therefore, maximisation of the high-frequency image content can minimise the optical aberrations. A filter function is required, so that only spatial frequencies below the cut-off frequency of the system are considered. The frequencies that are used for the metric determine the sensitivity and range for with it can be used: the higher the frequencies under consideration, the lower the signal-to-noise ratio will be. Also, higher frequencies may only be measurably affected when the aberrations are not too severe.

Mathematically, the frequency content metric, $f_{fourier}$, is written as the filtered Fourier transform of the image intensity [18]:

$$f_{fourier} = \sum_{\sqrt{F_x{}^2 + F_y{}^2} \geq F_l}^{\sqrt{F_x{}^2 + F_y{}^2} \leq F_u} \mathcal{F}\left\{i(x,y)\right\}(F_x, F_y) \tag{5.3}$$

where $\mathcal{F}$ denotes the Fourier transform and F_l and F_u are the upper and lower bounds of an annular filter for spatial frequencies F_x and F_y. In Section 8.1 it is shown that a lower and upper bound of 60% to 80% of the spatial Nyquist frequency of the detector are chosen, respectively.

Maximum Intensity

The maximum intensity metric has the value of the highest-intensity pixel in the region of interest. Maximum intensity in a PSF image occurs when there are no aberrations, so the image is diffraction-limited. It is a simple metric to implement and primarily useful for images of point sources. However, for extended scenes with low contrast, this metric may be noise sensitive, as only small gains in intensity are achieved. By only using the value from one pixel, most of the image sensor data is ignored. Therefore, the maximum intensity metric is not considered useful, compared to the sharpness metrics discussed before.

Sharpness sensor type and location

Contrary to the point source observed in ground-based astronomical telescopes, the sharpness sensor in the DST (see Figure 3.4) will observe an extended scene that is changing with a ground speed of ca. $7\,\mathrm{km\,s^{-1}}$. A conventional solution is to activate the attitude control system to point the instrument to one ground scene. The sharpness optimisation can then be performed during the time that the viewing angle of the ground scene does not change too much.

To enable the application of the image sharpness optimisation without active pointing, overlapping images could perhaps be used. Figure 5.13 shows that the sharpness of a specific overlapping area can be compared, such that each overlap allows for one optimisation step. Another option proposed here, is that the sharpness sensor consists of a secondary TDI detector, optically in series with the primary. The relative sharpness of the ground scene will then change when the DM is controlled, and the effect is detected as a difference in image sharpness between both detectors. See Figure 5.14. Since the TDI detector integrates the signal over multiple lines of pixels, the SNR will be higher than for the overlapping image technique described above. However, the application of only TDI detectors means that scene-staring is not directly possible. Hence sharpness optimisation algorithms that use a static scene, such as Nelder-Mead simplex, may require a different detector configuration.

Figure 5.13: Four partly overlapping images, acquired by the sharpness sensor. Each area of overlap can be used for one sharpness optimisation step. Satellite image © DigitalGlobe.
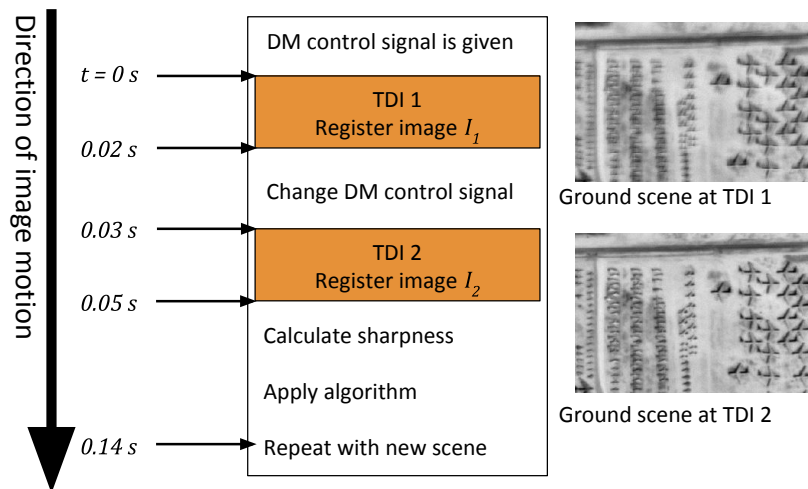
Figure 5.14: Differential sharpness principle: a ground scene, imaged on the focal plane, will be scanned by TDI 1 and TDI 2 at different times. When the wavefront corrector changes during this time, a difference in sharpness between the images from both detectors will be observed that can be used as input for optimisation algorithms.

5.4.2. Implicit sensor: algorithm based

Rather than physically optimizing a performance metric, a computational algorithm can be used to estimate the wavefront phase error from an acquired image. Subsequently, the DM can be controlled to remove this phase error.

Compared with the performance metric optimisation explained above, the main advantage of algorithm-based detection is that only a single image or set of images is required, instead of a continuous stream of new image data. Even when it is actively pointing, the telescope can never observe the exact same ground scene for more than a few seconds: the change in viewing angle will change the image contents.

When the image quality on the detector cannot physically increase any more, the phase error estimate can still be used for digital image restoration by deconvolution. This is another advantage of algorithm based wavefront retrieval.

As for the performance metric maximisation, a requirement for algorithm-based detection is that extended scenes can be used, to avoid pointing at stars for PSF retrieval.

Gerchberg-Saxton algorithm

The Gerchberg-Saxton algorithm, explained by e.g. Goodman [16], iteratively estimates the wavefront phase in the exit pupil by generating a PSF estimate from a pupil phase estimate, and subsequently replacing the amplitude of the generated PSF with that of the measured PSF. These steps are repeated until the phase estimate has converged. Although it has been proven to converge and has been useful for astronomical space telescopes, this algorithm requires a PSF image. Therefore, it is not considered applicable for the DST, which only acquires extended Earth scenes.

Phase diversity algorithm
The phase diversity (PD) algorithm uses one pair of images from two different detectors. One of these detectors is placed slightly out of focus, hence the name of this algorithm. When a wavefront estimate minimises the PD error metric [47], the algorithm has converged. Extended scene images can be used in this algorithm, which makes it suitable for the application under study. A useful source on Phase Diversity is [48].

The PD error metric E is mean-squared error between the predicted image data and the actual image data:

$$E = \sum_{F_x, F_y} \left| \mathcal{G}_i(F_x, F_y) - \hat{\mathcal{H}}(F_x, F_y)\hat{\mathcal{G}}_o(F_x, F_y) \right|^2 + \sum_{f_x, F_y} \left| \mathcal{G}_{i,d}(f_x, F_y) - \hat{\mathcal{H}}_d(F_x, F_y)\hat{\mathcal{G}}_o(F_x, F_y) \right|^2 \quad (5.4)$$

where $\mathcal{G}_i$ denotes the image spectrum, $\hat{\mathcal{H}}$ the PSF estimate and $\hat{\mathcal{G}}_o$ the object estimate, all in the Fourier domain. Subscript d indicates that phase diversity has been applied. As shown in Chapter 3, the PSF spectrum is the Optical Transfer Function (OTF), $\hat{\mathcal{H}}$, which can be estimated initially. The diversity OTF $\hat{\mathcal{H}}_{i,d}$ can then be calculated with respect to this estimate. Parametric optimization of the OTF can then be performed until the following error is minimised:

$$E = \sum_{(F_x, F_y)} \frac{\left| \mathcal{G}_i(F_x, F_y)\hat{\mathcal{H}}_d(F_x, F_y) - \mathcal{G}_{i,d}(F_x, F_y)\hat{\mathcal{H}}(F_x, F_y) \right|^2}{\left| \hat{\mathcal{H}}(F_x, F_y) \right|^2 + \left| \hat{\mathcal{H}}_d(F_x, F_y) \right|^2} \quad (5.5)$$

which is not dependent on the object $\mathcal{G}_o(F_x, F_y)$. For the optimisation, the conjugate gradient method is proposed [12]. Therefore, phase diversity can be applied to estimate the OTF of a system.

The application of PD on the DST has already been simulated and described in more detail by Dolkens [3]. Two TDI detectors are modelled in the telescope focal plane, both having slightly different field locations. It has been shown that the PD algorithm correctly retrieves the wavefront in over 70% of the modelled cases.

Since the phase diversity error is minimised via optimisation techniques, computational power is required in-orbit or on the ground. However, as also described in Subsection 5.3.4, an FPGA may be used for this. For example, particle swarm optimisation techniques have been implemented in FPGAs, leading to an order of magnitude decrease in execution time when compared to a conventional PC [49]. Also the two-dimensional Fast Fourier Transform (FFT) algorithm that is required for many algorithms has been implemented in an FPGA, showing a high reduction in execution time [50].

An example of wavefront control with PD is given by Georges et al. [51]. With an experimental test setup, an RMS OPD of ca. 0.3λ could be reduced to 0.002λ at a control bandwidth of $100\,\text{Hz}$. This suggests that a wavefront sensor based on PD can be a feasible alternative to other sensors.

Differential OTF algorithm
The differential OTF algorithm, described by Codona [52], has been developed to allow for phase estimation without the need of an explicit wavefront sensor. The algorithm uses two PSF images, obtained from the original pupil and a pupil with a small and masked part, respectively. From the differential OTF obtained from the two PSF images, a phase estimate can be reconstructed. Since the differential OTF algorithm requires PSF images, it is not considered applicable in the DST.

5.4.3. Explicit wavefront sensors
Explicit wavefront sensors do not make use of normal imaging sensors and image data, but rather require extra optical surfaces to directly relate the sensor output to a local wavefront shape. This can remove the problem of non-unique solutions found in implicit wavefront detection, but may also lower the computational cost of wavefront determination.

There are two large disadvantages of explicit detection methods. Firstly, an additional non-imaging optical channel needs to be implemented. This channel adds complexity to the telescope, but cannot be used for imaging purposes. Explicit sensors often require a high signal, so that the explicit wavefront sensor may reduce the signal that is available for imaging purposes. Secondly, the maturity of extended-scene explicit wavefront sensors is not high. Many of these sensors are designed for astronomical research. They are therefore only able to estimate the wavefront that originates from a distant point source, such as a star.

Shack-Hartmann sensor

Shack-Hartmann sensors are widely used in astronomy. Their main working principle is relatively straightforward: the sensor consists of a lenslet array and a detector, which are placed in the pupil of an optical system. The local tilt of the wavefront causes a shift in the local image, as illustrated by Figure 5.15. So, the derivative of the OPD is directly measured. With this information, the wavefront phase can be recovered. The sensor is well suited for the continuous correction of atmospheric aberrations. Ideally, one point source is used to produce a distorted grid of points on the detector. For the extended
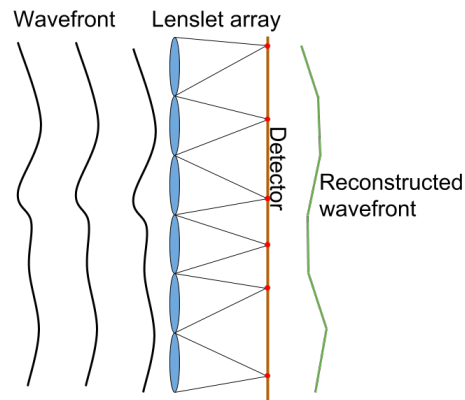
Figure 5.15: Conceptual working of a Shack-Hartmann wavefront sensor. The lenslet array forms subimages on the detector, of which the position is determined by the local wavefront tilt. Algorithms can construct a wavefront estimate from the local slope measurements.

Earth scenes captured by the telescope, different algorithms can be applied on the output of a SH-WFS to estimate the subimage shifts. Poyneer [53] shows that a periodic correlation method can be used to estimate subimage shifts within fractions of a pixel size, thus enabling wavefront slope reconstruction. In case the subimages are distorted with respect to each other, more advanced algorithms can be implemented [54].

While the direct measurement characteristics, relative simplicity and high TRL make the SH-WFS seem advantageous, there are drawbacks. The major issue with application of the SH-WFS to the DST is that the system needs a planar-like wavefront from the pupil of the telescope. Hence, from Figure 5.4, it can be seen that this requires a beam splitter or collimating optics in the optical path. The use of a beam splitter results in a strong decrease of available signal to the TDI detectors, driving the need for a larger aperture. On the other hand, a collimator before the SH-WFS cannot be incorporated in the current optical design without adding mass and complexity. Also, additional optics introduce field-dependent aberrations, so that the actual common-path aberrations cannot be derived with certainty.

A second drawback is that the high ground velocity means that a short integration time of the SH-WFS is required, or that the spacecraft needs to actively point to one location. When the SH-WFS subimages take up 0.05° of the field in the along-track direction, the entire scene changes every 57 ms when orbiting at 500 km. A rough assumption is that the integration time is one or two orders of magnitude below the full scene change to prevent smear effects, leading to an integration time between 0.57 ms and 5.7 ms.

Interferometric sensors

Interferometry uses interference patterns of monochromatic coherent light to measure distances and surface deformations. In this way, optical surfaces can be characterised. So, when such a sensor is applied in the DST design, an on-board laser and interferometry sensor are required on each mirror to be characterised. This results in a complex and heavy solution for deducing the phase error, compared to the other solutions that use the already available light.

Light field camera

Plenoptic cameras or light field cameras are devices with a normal main camera lens and an array of micro-lenses in the image plane. It can thus be regarded as a Shack-Hartmann wavefront sensor with an additional main lens. This camera generates a large collection of pupil images, which can be used to determine the distance to an imaged object and to reconstruct the wavefront over the entire pupil [55].

In addition to the capabilities of the SH-WFS, the light field camera can reconstruct a three-dimensional light field. This is especially useful for the correction of atmospheric distortions and aberrations [56] or re-focussing after an image has been taken.

Regarding application to the DST, aberrations do not originate from a three-dimensional aberration volume. The light field camera capabilities are not required. On top of this, the sensor has a low TRL in active optics and space applications. It also requires careful calibration to allow proper working of the algorithms on the image data. Furthermore, the same integration time disadvantage as with the SH-WFS applies. Therefore, the use of a light field camera as wavefront sensor has no advantages over the use of a SH-WFS. It is therefore not considered in the concept generation.

5.4.4. Overview of aberration detection methods

The aberration detection methods described in this section are summarised in Table 5.3. As the aberration detection method shall be able to work with extended scene input, the Gerchberg-Saxton and Differential OTF methods are not applicable. Furthermore, a Shack-Hartmann sensor can only be used with an algorithm for determining shifts of extended scene subimages. The advantages of using a light-field camera for wavefront reconstruction are mainly relevant for atmospheric aberrations, so also this detection method will not be included in the conceptual designs. The three sharpness metrics in the top rows of Table 5.3 are further analysed in Section 8.1.

Table 5.3: Overview of aberration detection methods. Whether the accuracy is high or tracking is required is dependent on the actual implementation of the methods.

Method	Extended scenes	Accuracy	Computational power	Physical components	Requires tracking
Intensity sharpness	Yes	High	Low	Image detector	TBD
Edge Sharpness	Yes	High	Low	Image detector	TBD
Fourier content	Yes	TBD	Medium	Image detector	TBD
Phase Diversity	Yes	TBD	High	2nd detector	No
Gerchberg-Saxton	No	TBD	Medium	None	Yes
Differential OTF	No	Low	Medium	Pupil modification	Yes
Conventional Shack-Hartmann	No	Medium	Low	Collimator, sensor	Yes
Extended-scene Shack-Hartmann	Yes	TBD	Medium	Collimator, sensor	TBD
Light-field camera	Yes	TBD	Medium	Camera	TBD

5.5. Wavefront Control Options

The *Wavefront control strategy* is linked to the aberration detection method. It is defined as the relationship between the output data from the aberration detection and the input signal to the image correction hardware or software.

The left branch in the DOT, Figure 5.16, shows direct wavefront control options, while the right branch contains design options for control via indirect measurements. Given that indirect aberration detection (sharpness sensing) and direct aberration detection (extended scene SH-WFS) are considered in this design stage, both branches are treated here. See also Figure 4.9.
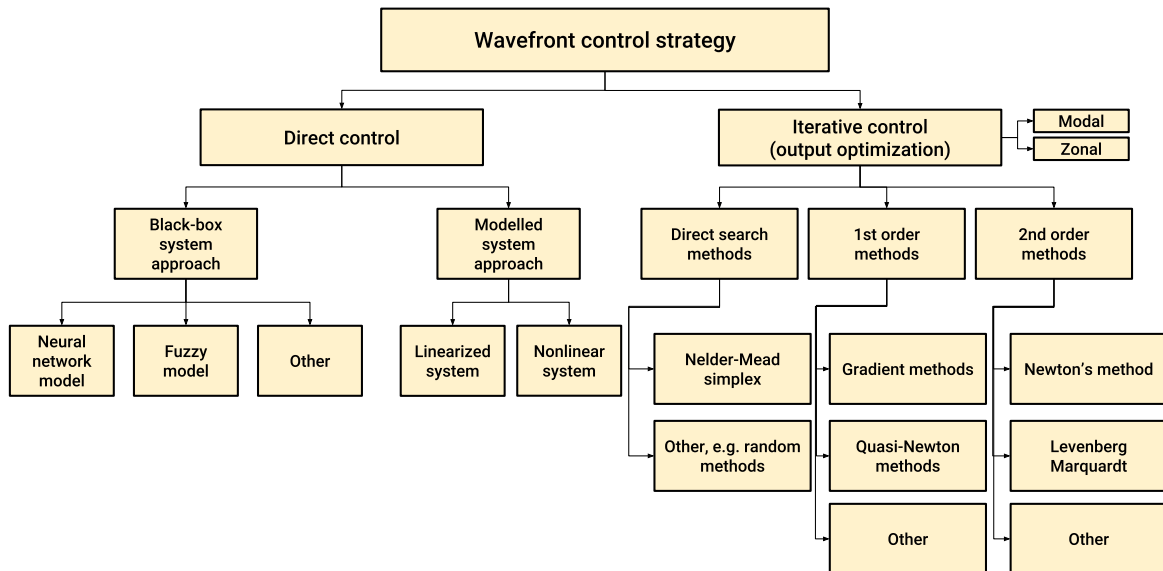
Figure 5.16: DOT for Wavefront Control options.

5.5.1. Direct wavefront control

In the left branch of the DOT, the *direct wavefront control* methods are shown. Direct control methods are considered here as methods where sensor output y can directly be mapped to a wavefront corrector input u, without the need for iteratively optimising the sensor output. Two direct control approaches are discerned: the black-box system and the modelled system.

Black-box system

In the first approach, the system is considered as a black-box where aberrations and sensor outputs are related in an implicit way. By calibrating the system with known aberrations, a non-linear mapping can be found between the aberrations and sensor output. Subsequently, a stream of sensor output data y can be used to directly calculate the control signal u that most likely removes the aberrations. Theory and experiments by Song et al. [57] show that it is possible to achieve faster control with black-box model-based aberration correction than with a simplex algorithm. However, the output metric must contain sufficient information to accurately estimate the combination of input terms. It is therefore mainly useful for laser systems or other PSF imaging systems.

Explicitly modelled system

The second direct control approach in the DOT uses an explicitly modelled system approach. This is the most conventional control approach for ground-based adaptive optics systems with Shack-Hartmann WF sensors. The main advantage of direct control with a modelled system is that the incoming wavefront is explicitly reconstructed, such that a control signal can be calculated without iterative processes. For wavefront reconstruction with wavefront slope measurements, zonal algorithms [58] or modal algorithms [59] can be used. See also Section 7.1.

The reason why the direct control approach with explicit modelling is used for ground telescopes, is that atmospheric aberrations are rapidly changing; this leads to a high control bandwidth requirement, in the order of tens of Hertz. A disadvantage of this type of systems is that an explicit wavefront sensor is required, which may not be optimal for the DST. See also Section 5.4 and Figure 5.19.

5.5.2. Iterative wavefront control algorithms

The right branch of the wavefront control strategy DOT is called *iterative control*, because the design options given there are all based on optimisation algorithms. When applied to the wavefront corrector, the goal of these algorithms is to maximise the optical performance metrics discussed in Section 5.4. This is done by iteratively changing the control signal u to the wavefront corrector, until the algorithm converges and the optical performance has been maximised.

Note that the black-box system approach described on page 46 also uses a performance metric, without the need for optimisation algorithms. The difference between iterative control and black-box control, is that the first does work without knowledge of the system, while the latter needs a black-box model that must be created with calibration and disturbance measurements.

The algorithm which will be implemented to control the wavefront corrector can best be selected and configured after the wavefront corrector has been designed. There is no need to treat all algorithms in the conceptual phase already, since different algorithms can relatively easily be tested in FORTA simulations. However, a general overview of methods is presented below to explore the options.

Zonal or modal control

Before the optimisation algorithms are presented, it must be noted that not only the control algorithm, but also the type of control variables can be chosen. Figure 5.17 shows the difference between zonal and modal control. When the actuators of a wavefront corrector are all independently controlled, this is called *zonal control*. The change in a single control variable leads to a surface shape that can only be accurately fitted with high-order Zernike polynomials. When mainly low-order errors are present, such as in the typical OPD shown in Figure 4.4, it may take many optimisation iterations to achieve a good fit with zonal control.

Therefore, *modal control* may be a better option in such cases: groups of actuators are controlled collectively, such that surface shapes with increasingly higher Zernike orders are the control variables [60]. In this way, the optimisation can only take into account the relevant modes, up to the highest mode that is supported by the actuators. This allows optimisation methods to reduce the number of control variables and increases the convergence rate. After this modal control optimisation process, zonal control can be applied to remove the local residual OPD. See also Chapter 8 for practical experiments.
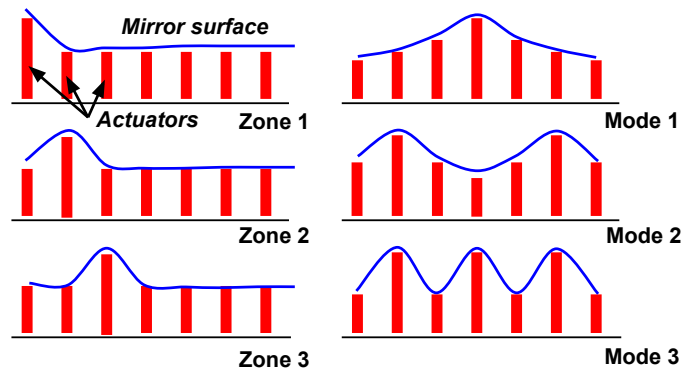
Figure 5.17: Examples of zonal control (left) and modal control (right) on a deformable mirror surface. Depending on the wavefront corrector design, expected aberrations and optimisation algorithm, modal or zonal control may be chosen. In this example, three variables cover the entire mirror with modal control, whereas they only provide local correction with zonal control.

Direct search methods

An optimisation method belongs to the group of *direct search methods* when no derivative information is used in the algorithm. This has the advantage that no numerical derivative estimates need to be

generated, so less function evaluations may be required. An example function evaluation can be: sending a control signal to the wavefront corrector and calculating the sharpness metric update.

The Nelder-Mead simplex method is often used as a direct search method, for example by Dolkens in the FORTA optimisation function [3]. The Nelder-Mead simplex method has successfully been applied to the phase diversity problem [12] for the DST in simulations [3], but more efficient algorithms may be available.

A more specific set of direct search methods are the random methods. The common property of different random methods, is that they generate random points in the optimisation space that are to be evaluated and select the best performing point. The most straightforward form is the random jumping method, which just evaluates the optimisation function at purely random points and stores the best performing point in memory. A variant of this is the random walk method, which generates random direction in the optimisation domain and makes a step with a given size in this direction. When this leads to a better function output, the step is stored as the new starting point. Other examples of random methods are simulated annealing or particle swarm optimisation.

Direct search methods may be useful for (nearly) discontinuous functions, or functions with many local optima, such as is the case for e.g. phase diversity [3]. However, direct methods require relatively many function evaluations and do not guarantee convergence to the global optimum.

First order derivative methods
When an optimisation method uses local derivative estimates, this method belongs to the group of first order methods. By using gradient information, convergence to a (local) optimum can be guaranteed. For example, the steepest descent method uses the local gradient to find the direction of fastest function decrease [61]. In some cases, the steepest descent method will require many zig-zag iterations. In such a case, a faster method may be the Fletcher-Reeves conjugate gradient method [62].

First-order methods that make use of the advantages of second-order methods are quasi-Newton methods. For example, the Broyden–Fletcher–Goldfarb–Shanno algorithm (conveniently abbreviated BFGS) uses an iterative scheme to update the Hessian of the function [63]. BFGS has rapid convergence for functions that are twice differentiable and convex, but may also work effectively on other classes of problems [64].

First order derivative methods can be very useful for the control of the wavefront corrector, as they can converge more rapidly to a minimum than direct optimisation methods. However, care must be taken that the optimisation algorithm does not get trapped in a local optimum.

Finally, a combination between random methods and first-order methods also exists in the form of stochastic gradient descent methods. These methods apply a random step to estimate the gradient. Such methods have been used since the 1980's in the training of neural networks, i.e. machine learning, because they can work with a large number of control variables in a computationally efficient way [65].

Second order derivative methods
When a second order derivative is used in an optimisation algorithm, this is a second order derivative method. The classical example is Newton's method, which uses a local second-order Taylor series to approximate the function. The minimum of the Taylor series then converges towards the function minimum. A more robust variant of this is the Levenberg-Marquardt method, which interpolates between the steepest descent method and Newton's method. It is especially useful for certain types of least-squares fitting problems [66].

For control of the wavefront corrector, second order derivative methods may be useful in certain concepts. However, this entirely depends on the design of the corrector and control variables. When the number of control variables is high, many iterations are required to compute the Hessian information in e.g. Newton's method. Using first order or second order derivative information may only increase the convergence towards the local optima in sharpness optimisation.

5.6. Tolerance Drift Compensation Options

The *Tolerance drift compensation* element is associated to the performance of the ACS with respect to temporal variations, i.e. drift, in the telescope optics. It is the final ACS system element to be considered for concept generation.

In an ideal situation, the wavefront corrector shape is optimised after in-orbit deployment and does not need to be optimised again. However, the thermal environment continuously changes during the orbit, which may lead to structural deformations and hence a deterioration of the OPD in the exit pupil. The severity of this drift determines how often the wavefront corrector shape must be updated. The DOT in Figure 5.18 shows the design options to deal with these drifts. Furthermore, Figure 5.19 graphically shows the different bandwidths of drift, creep, jitter and the solutions that are proposed.
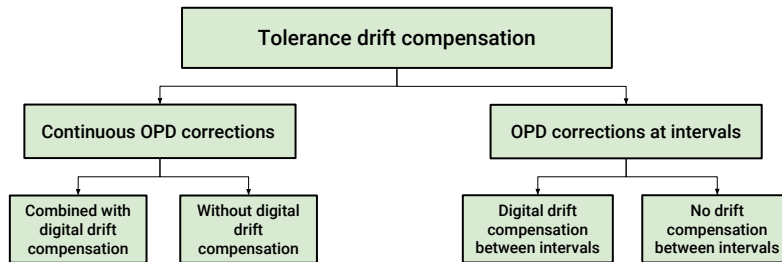
Figure 5.18: DOT for Wavefront Control options.

5.6.1. Continuous or intermittent wavefront control

The first design option choice is between continuous OPD corrections and intermittent OPD corrections. With continuous corrections, it is meant that the wavefront correction system operates continuously in a closed control loop, irrespective of the actual severity of the aberrations. When intermittent OPD corrections are implemented, the drifts are only compensated when this is necessary and feasible.

The severity and temporal frequency of the drifts can be estimated by thermo-mechanical simulations of the structural and optical design. However, no detailed thermal model of the telescope is available at the time of writing this thesis. Therefore, it cannot be determined in this design stage whether continuous control for drift compensation is required or whether intermittent control is sufficient. To ensure the ACS performance will be sufficient, it is assumed that the drift tolerances from Table 4.1 are introduced over a period of ca. 10 minutes.

Next to drift, changes in the structure occur because of finite optical stability. The stability budget contains high-frequency effects from vibrations, called jitter, which may be introduced by the attitude control subsystem. From future bottom-up analysis of the stability, it will be determined whether the ACS should also correct for the vibrations in the optics. If this is required, it will increase the required control bandwidth from a few times per hour to several Hz: From Barreto [4], it is found that the first resonant frequency of the M2 deployment boom is in the order of 6 Hz and from Van Putten [5, Table 22], it can be seen that the first resonant frequency of the M1 structure is ca. 204 Hz. It is unlikely that these vibrations can be compensated by a system which iteratively optimises the wavefront corrector shape. So, if required, a dedicated wavefront sensor has to be implemented to create a closed-loop feedback system. Nevertheless, a well-designed stiff deployment structure is preferred above active compensation of vibrations, because field-dependent aberrations are introduced by mirror misalignments. These cannot always be corrected with an OPD corrector, as was shown before in Figure 5.10.

So, whether it is feasible and desired to implement closed-loop wavefront control depends on the selected wavefront sensing method from Section 5.4 and the required bandwidth of the control system. For example, methods that require active pointing of the telescope to a selected spot on Earth do not allow for continuous wavefront control, since active tracking of a ground scene hampers normal operations. Therefore, the correction interval design choice is also coupled to the choice of aberration detection method and the vibration compensation requirement.

5.6.2. Digital drift compensation

Besides physical OPD corrections, digital corrections can be applied by e.g. Wiener deconvolution of the imagery with the system PSF. This is especially useful to reduce the effect of optical drifts on the image quality, when the OPD corrector cannot be continuously controlled. Also, the effect of high-frequency vibrations that are not physically compensated can be reduced in this way.

As explained in Section 5.4, the PSF can be retrieved from a phase diversity algorithm that uses data from the two TDI detectors. However, because both TDI detectors are positioned at slightly different locations, this algorithm will be influenced by spatial variations and temporal variations in the PSF. However, these effects are considered negligible. Furthermore, depending on its rate of change, the PSF estimate from phase diversity is to be updated. In the most extreme case, this can be done on every set of images, if the computing power is available.

It is important to note that digital reconstruction of the image is not useful for all Earth observation applications: while the image resolution may increase, deconvolution methods are known to amplify noise, so that radiometric accuracy is reduced and other quantitative image data can become lost. For this reason, physical correction of the aberrations in the instrument itself is preferred above digital reconstruction.
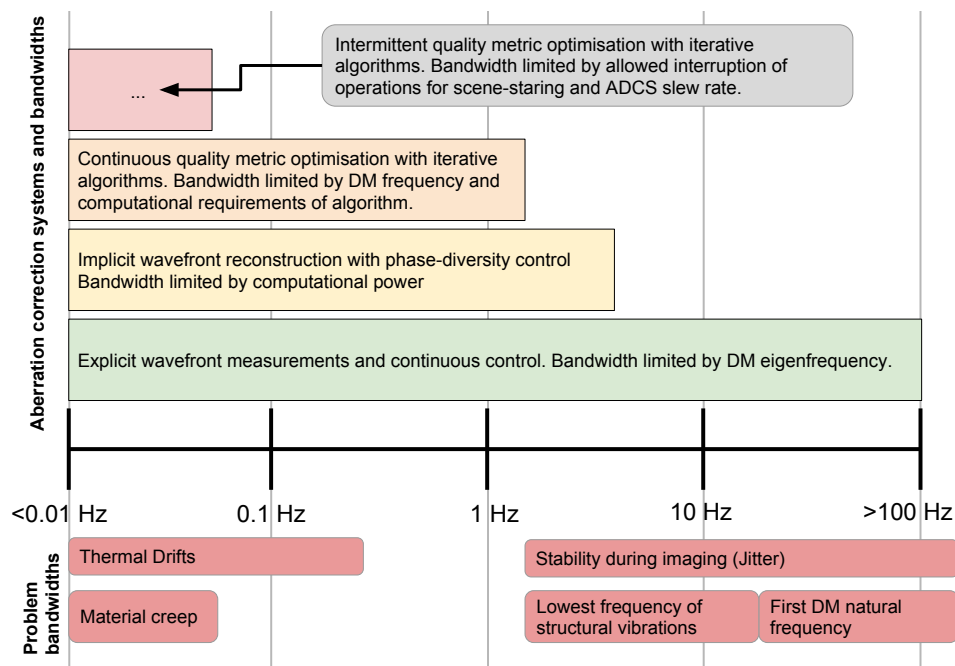
Figure 5.19: Approximate bandwidths of the different sources of image degradation and the ACS concepts.

5.7. ACS Concept Generation

From the design options that are treated in the previous Sections, five different ACS concepts have been generated. These are shown in Morphological Table 5.4. Many more concepts are possible in theory, but these five are clearly distinguishable in terms of performance budgets, method of operations, mass and (computational) power. The main philosophy behind these concepts is treated below in the same order as the columns from Table 5.4.

Table 5.4: Overview of the five ACS concepts. The philosophy behind the concepts is as follows: concept *LowReqs* has minimum required capabilities, in case little drifts are expected that can be solved with sharpness sensing. It uses a DM with intermittent wavefront control and no drift compensation by phase diversity. Concept *PDDrift* is the same, but includes phase diversity drift compensation on-ground. Concept *PDControl* uses on-board phase diversity algorithms to aid the control system, enabling continuous DM control. When the bandwidth needs to be in the order of 1 Hz, an extended-scene Shack-Hartmann WFS will be used for closed-loop control. This is done in concept *SHControl*. Finally, concept *Entrance* uses lightweight Actuated Hybrid Mirrors as primary mirror segments, thereby minimising the system mass.

Element	Concepts				
	LowReqs	*PDDrift*	*PDControl*	*SHControl*	*Entrance*
WF Corrector[1]	Def. Mirror	Def. Mirror	Def. Mirror	Def. Mirror	AHM
Location of correction	Exit pupil	Exit pupil	Exit pupil	Exit pupil	Entrance pupil
Location of PD[2] drift compensation	None	On-ground	In-orbit	None	On-ground
Aberration detection	Performance Metric	Performance Metric	Performance Metric + PD	Shack-Hartmann	Performance Metric
Control strategy	Optimize metric	Optimize metric	Metric + DM Model	DM Model	Optimize metric
Control variables[3]	Modal	Modal	Modal + Zonal	Modal	Modal
Duty cycle	Intermittent	Intermittent	Continuous	Continuous	Intermittent

[1]Deformable mirror type (e.g. membrane, bimorph) to be determined in later design stage. This also holds for the AHM design.

[2] Phase Diversity

[3] For any concept, the definite choice between modal or zonal control has little influence on the overall hardware design. The choice depends on the WF corrector design and the final aberration distribution in the telescope.

1. **LowReqs**
   The *LowReqs* ACS concept contains a DM in the DST exit pupil. Its name stems from the relatively low requirements on temporal performance of the ACS. This concept has no drift compensation via phase diversity. The DM is controlled via a performance metric, e.g. sharpness, which is optimised during the tracking of ground scenes. Modal control is performed at intervals, which interrupts the normal scanning operations. This concept has the advantages that it requires no second TDI detector, no phase diversity, np telemetry, and little power. However, disadvantages are that normal operations need to be interrupted for DM control and that the effects of thermal drifts cannot be restored digitally.

2. **PDDrift**
   The second concept is called *PDDrift*, since drifts are compensated via phase diversity (PD). This ACS concept contains a DM in the DST exit pupil. It does have on-ground drift compensation via phase diversity. The DM is controlled via a performance metric, e.g. sharpness, which is optimised during the tracking of ground scenes. Modal control is performed at intervals, which interrupts the normal scanning operations. Compared to the *LowReqs* concepts, this concept has the advantage that the effects of thermal drifts can be recovered via PD. However, disadvantages are again that normal operations need to be interrupted for DM control and that the data rate of the communications subsystem needs to increase to allow the raw data of two TDI detectors to be transmitted to ground. So, a ground station needs to be set up for running the PD algorithm and deconvolving the imperfect imagery.

3. **PDControl**
   As with the previous concepts, the *PDControl* ACS concept also contains a DM in the exit pupil. Its name has been chosen to indicate that phase diversity is used to support the wavefront control. This concept does have drift compensation via phase diversity, just like the previous concepts. However, in this *PDControl* concept, the recovered wavefront is used to increase the rate of convergence of the DM. After the most recent PD wavefront estimate has been used to initialise the DM shape, it is controlled via a performance metric, e.g. sharpness, before normal operations start. Ideally, this system then continues to use PD algorithms to keep track of the thermal drifts. It can compensate for these drifts by changing the DM shape, based on an internal mathematical model, thereby ensuring that the aberrations will remain small. This speeds up the PD algorithm compared to the *PDDrift* concept, as it's optimisation domain can be limited to smaller wavefront errors. Modal control is performed initially, after which zonal control is applied to optimise the DM shape.

   The main advantage of this concept is that continuous compensation of thermal drifts can be performed, without interrupting normal operations. Also, is makes use of the benefits of two wavefront sensing systems: performance metric optimisation for the compensation of initial errors, and PD for monitoring the wavefront degradation. A disadvantage is that this system is sensitive to the computational speed and accuracy of the PD algorithm, and that it has not been implemented in telescopes before.

4. **SHControl**
   In case the thermal drifts and/or low natural frequencies of the telescope require rapid optical corrections, the *SHControl* concept can be used. Its name illustrates that an extended-scene Shack-Hartmann wavefront sensor (SH-WFS) is used to provide continuous control to the DM. This removes the need for a sharpness sensor and phase diversity, but requires the addition of a SH-WFS in the exit pupil. With the explicit SH wavefront estimate, a DM plant model can be used to achieve closed-loop modal control. Advantages of this system are that continuous, high-quality corrections are possible at rates of 1 Hz and above. However, the additional sensor in the pupil requires that a significant part of the signal to the detector is taken away, thereby decreasing the signal-to-noise ratio on the FPA. Furthermore, a study needs to be performed to investigate if scanning operations do not limit the applicability of a conventional imaging SH-WFS. Finally, the performance of the sensor depends on the algorithm that correlates the SH subimages, which needs further study.

5. **Entrance**
   The interesting Actuated Hybrid Mirror(AHM) mentioned in Subsection 5.2.5 is used in the *Entrance* concept to provide OPD corrections in the entrance pupil of the telescope. All other design

options have been set to the same as those in the *PDDrift* concept. The *Entrance* concept uses large, lightweight deformable mirrors as the primary telescope mirror. They are controlled via sharpness optimisation at intervals. This concept has major advantages in terms of telescope mass, as it allows for a weight reduction of M1 and removes the need for a DM in the exit pupil. However, the TRL of the AHM technology is low, and it is beyond the current scope of the DST project to reproduce AHMs and increase their TRL. Therefore, unless the project resources increase dramatically, this concept is not considered feasible.

5.8. ACS Concept Trade-off

This section presents a trade-off for the concepts that have been introduced in the previous section. The trade-off criteria that are used have been explained in detail in Section 5.1. Table 5.5 shows the relative performance of the five concepts. Concept *PDDrift* is used as a reference on all criteria. In the first column, the performance of a telescope without any ACS is shown for completeness.

Table 5.5: Trade-off of the given ACS concepts. Column *No ACS* indicates the DST performance in absence of an aberration correction system. Concept *PDDrift* was taken as reference concept.
Meaning of the colours, with respect to the reference concept:

−− = strongly inferior, − = slightly inferior, 0 = neutral, + = slightly superior, ++ = strongly superior

			Concepts			
Primary Criteria	*No ACS*	*LowReqs*	*PDDrift*	*PDControl*	*SHControl*	*Entrance*
Misalignment compensation	−−	0	0	0	0	0
Drift compensation	−−	−	0	+	++	0
Secondary Criteria						
Total mass	+	+	0	0	−	++
On-board power	++	+	0	−−	−	0
Cost	++	+	0	0	−	−−
Risk	−−	+	0	0	0	−
Scanning interruption[1]	++	0	0	+	++	0
Next design stage?	✗	✓	✓	✓	✗[2]	✗[3]

[1]Assumes that normal scanning operations are interrupted by performance metric optimisation or PD, and not by using the SH-WFS. This assumption is to be investigated and is therefore not driving the trade-off outcome.

[2]As explained in the text, the superior drift compensation performance of the *SHControl* concept may be much higher than required for the DST, as this sensor is developed to compensate rapidly changing atmospheric aberrations on ground. Therefore, this concept will only be considered when such extreme drift compensation is really required.

[3]Given the low TRL of this concept and its high development costs, it is considered infeasible to analyse it in more detail in the scope of this thesis. However, when more resources are available, this concept may evolve into something that is really applicable.

5.8.1. Score per criterion

Below, the reasoning behind the scores in the trade-off table is set out.

1. **Initial misalignment and error compensation**
   The initial misalignments and surface errors of the telescope cause aberrations of the light wavefront. As shown in Subsection 4.2.1, not including an ACS will result in an optical performance that is far below acceptable levels. This is indicated in the first column of trade-off table. In all

five ACS concepts, a deformable mirror (DM) is included that compensates for these aberrations. Depending on the capability of the DM, each concept can in principle perform equally well. Judging from the DM performance research, presented in Table 5.1, there are different possible DMs on the market that can comply with the requirements given in Chapter 4. Which DM will be included in each concept, is selected in a later stage of the project: see Chapter 6.

2. **Drift compensation**
While all concepts score equally well on the initial misalignment compensation criterion, their drift compensation capability differs. The *LowReqs* scores a "−", as it has no phase diversity wavefront estimation system and does not allow for continuous sharpness optimisation. Thus, the in-orbit drifts will influence the optical performance of this concept more than for the *PDDrift* concept. The latter makes use of on-ground phase diversity to reconstruct the wavefront drift and deconvolve the aberrated images for quality improvements. This deconvolution step amplifies noise [67] and therefore does not guarantee a stable radiometric performance. The same holds for concept *Entrance*.

To overcome this potential issue, concept *PDControl* uses on-board phase diversity for wavefront error estimation and subsequently uses this to control the DM. By restoring the wavefront physically instead of digitally, the signal-to-noise ratio on the FPA is increased. A proof of this *PDControl* concept has been given by Georges et al. [51]. Therefore, a "+" score is given.

A potential limitation of the *PDControl* drift compensation, are the high computational power and convergence conditions of the PD optimisation algorithm. Concept *SHControl* uses a Shack-Hartmann WFS, which allows the reconstruction of a wavefront at a high temporal bandwidth, but without a high computational load. Also, potential divergence of the PD algorithm is not relevant for this explicit WFS. Therefore, drift compensation capability of *SHControl* has been given a "++" score.

3. **Total mass of the spacecraft**
The spacecraft mass will be minimum for concept *Entrance*, because the mass of the primary mirror segments can be decreased w.r.t. their current, stiff design [11]. Therefore, it is superior even to the DST design that has *No ACS* and scores a "++". Concept *LowReqs* has a lower mass than than the reference concept *PDDrift*, because no PD implementation is included. This allows for savings of mass on the second TDI detector, data handling subsystem, power subsystem and communications subsystem. Hence, it scores a "+".

Concept *PDControl* will require a phase diversity sensor and on-board computing power. However, it is not considered more heavy than *PDDrift*: because the raw data of only TDI 1 needs to be sent to Earth, the mass of the communications subsystem can be reduced. This estimate results in a "0" score. However, the true mass difference of both concepts depends on the TBD control bandwidth (and hence, the power and thermal control) that is required for *PDControl*. These numbers can be estimated in more detail when this concept is found to be viable from simulation experiments.

Concept *SHControl* scores a "−", because it is considered heavier than the other concepts: the signal that is required for the SH-WFS will increase the required aperture. Also, as the sensor needs to be placed in the exit pupil, the optical design needs to be modified. This will further increase the instrument volume and mass.

4. **On-board power consumption**
Power consumption is uncertain at this stage, because it depends on estimations of the power that is required for:

  • Ground-scene tracking during sharpness optimisation
  • On-board phase diversity calculations
  • Downlinking raw data of a second TDI detector for on-ground PD
  • Dissipation by the DM actuators during movement and in a fixed position.

The magnitude of all these estimates are influenced by the required DM update interval and actuator technology: it is unknown at this stage whether the DM needs control updates e.g. every month, every minute, every second, or faster.

As treated in Subsection 5.3.4, on-board PD optimisation algorithms require considerable power. This is why concept *PDControl* is considered most power-consuming and receives a score "− −". The *LowReqs* concept has no phase diversity, and this reduces its power consumption to

a score "+". The power required by the SH-WFS to provide high-bandwidth control in *SHControl* depends on the cross-correlation algorithm for wavefront determination, which is running continuously. This is expected to require more power than the occasional use of PD in *PDDrift*, so *SHControl* receives a "-".

5. **Cost**
The total ACS cost is estimated by considering the full missions costs, from development to end-of-life. The *Entrance* concept will be the most expensive one (score "– –"), because the lightweight actuated hybrid mirror technology needs to be further developed and thoroughly tested before commercial applications are possible. Also the *SHControl* concept is likely to be more expensive than reference concept *PDDrift*, because the telescope volume and mass need to increase to incorporate this sensor. Concept *PDControl* and *PDDrift* are comparable in terms of development effort, number of components, mass and volume. Hence, they both score a "0". The *LowReqs* concept has no second TDI detector, requires less novel components, less on-board power and less mass. This reduces the total cost, so that a score "+" can be allotted.

6. **Risk**
The concepts *LowReqs*, *PDDrift*, *PDControl* and *SHControl* all make use of existing technologies, although they have never been applied in high-resolution space instrumentation. The sharpness optimisation used by *LowReqs* is an established method, such that the risk is relatively low. Therefore, it gets a score "+". The application of PD in closed-loop concepts is much less common, because the PD algorithm can get trapped in a local optimum. This leads to a lower score of "0". Furthermore, concept *Entrance* has never been used commercially on-ground or in space. The large, thin mirrors that are located outside the instrument bus will have to survive the launch environment and need to be deployed. After this, they are more exposed to radiation, micro-meteorites and thermal variations than the DMs in the other concepts. Therefore, the *Entrance* concept scores a "–" on the mission risk criterion. Finally, in case *No ACS* is included, the mission is doomed to deliver insufficient image quality. This almost certain failure causes an allocation of "– –" to the mission risk criterion.

7. **Interruption of scanning operations**
For the trade-off, it is assumed that the SH-WFS will receive sufficient signal to acquire the wavefront estimate without the need for active pointing to a ground scene. Also, it is assumed that the two-TDI sharpness optimisation method presented in Figure 5.14 in Subsection 5.4.1 cannot be implemented due to insufficient optimisation performance. So, sharpness optimisation was assumed to require active tracking of one ground scene. However, as will be shown in Chapter 8, this assumption was false.

The *LowReqs*, *PDDrift* and *Entrance* concepts all require active tracking for sharpness optimisation and score a "0". For concept *PDControl*, interruption of scanning operations is only required when the PD algorithm does not converge, such that sharpness optimisation is required to "reset" the error. Therefore, *PDControl* scores a "+".

Under the current assumptions, *SHControl* never requires scene tracking, hence TDI scanning operations never need interruption. So, a score "++" has been allotted to *SHControl*.

5.8.2. Trade-off outcome
The scores that have been allotted in the previous subsection have been put in a trade-off. See Table 5.5.

The following outcomes are taken from the trade-off. Firstly, as stated already in 4.2, *No ACS* is not an option, as this will lead to an RMS OPD that is roughly an order of magnitude above the maximum allowed RMS OPD.

Secondly, the *Entrance* concept is too risky to implement directly, and too expensive to develop with the resources that are currently available. It is therefore discarded at this stage. However, in case more resources become available in the future, this concept can be studied in more detail.

Thirdly, the *SHControl* concept is only beneficial if all three following conditions are true:

- If optical tolerance drift compensation is required at a bandwidth of ca. 1 Hz or above

- When it is found that the *PDControl* concept uses too much power to achieve this bandwidth.

- When the performance metric optimisation in e.g. *LowReqs* cannot be applied without interrupting scanning operations.

All these conditions are expected to be true, so the *SHControl* concept is not considered for further investigation at this point in the DST project. It will be considered as a back-up option, in case the other remaining concepts are found to have insufficient drift compensation capabilities.

So, finally, three concepts, namely *LowReqs*, *PDDrift* and *PDControl*, are interesting candidates for the detailed ACS design. They can be included in the end-to-end DST simulation in the FORTA software, such that their performance under different conditions can be analysed and a detailed design can be produced.

II

Simulating the Aberration Correction System

Introduction to the Second Part

In the previous part, three out of five concepts have been selected that may fulfil the requirements for an Aberration Correction System on the Deployable Space Telescope. However, a realistic and scientific analysis of these concepts and their design options is essential for a proper evaluation of their performance. Therefore, this part treats the simulation and detailed design of the ACS. Figure 5.20 shows the research steps that are suggested to achieve a fully functional breadboard system.

As shown in the figure, several elements of the ACS concepts need detailed investigation and design. For example, all remaining concepts use DM control via performance metric optimisation. However, there are still questions regarding the application of sharpness sensing and optimisation to a scanning system. Furthermore, different design options, such as the DM layout, can only be evaluated in a quick and low-cost way via simulation of the ACS hardware and controller.

Ideally, a DM reduces the OPD in the exit pupil to zero for all optical fields. However, in reality, this is impossible: to accurately simulate the performance of the different ACS concepts and options, three factors need to be considered in the simulation that cause non-ideal performance.

Firstly, the DM can never perfectly reduce the OPD, even if it is perfectly known. The reason is that the mirror deformation is governed by the influence functions of the actuators. Only deformations that are a combination of influence functions can be produced. A realistic model for the correction ability of two types of mirrors, PDMs and MDMs, has been implemented in FORTA. Details of this model and the performance of the modelled DMs are treated in Chapter 6.

The second nonideality is related to the aberration detection. Effects such as noise, convolution with a ground scene and temporal variations need to be considered for OPD and sharpness sensing simulations. Chapter 7 focuses on this aspect of the ACS.

Finally, a third nonideality in the real ACS is the controller that steers the actuators of the DM. While an ideal DM control setting may be calculated analytically, the true deformation commanded by the control algorithm may not be the same. A simulation of a sharpness controller is also introduced in Chapter 7.

This part closes with the results of case studies and Monte-Carlo simulations of the ACS in Chapter 8 and a conclusion and final design overview in Chapter 9.

Due to the limited scope of this thesis, not all steps shown in Figure 5.20 have been carried out. Step 2.3 has been skipped, as the mirrors under consideration do not suffer from significant hysteresis. Furthermore, step 3 and step 5 were skipped entirely and are assigned to Dirk Risselada as part of his MSc thesis research. Step 4 has partly been carried out, see Section 8.7.

1		**1.1**		**1.2**		**1.3**	
Simulate DMs to find optimum performance		Add influence functions to FORTA		Add maximum stroke limit of each DM		Run Monte-Carlo simulation with LSQ fit of DMs	

2		**2.1**		**2.2**		**2.3**		**2.4**	
Simulate DM control to choose performance metric and optimiser		Configure different performance metrics in FORTA		Write different optimisation algorithms		Include DM hysteresis simulation		Run Monte-Carlo simulation with each metric and algorithm	

3		**3.1**		**3.2**		**3.3**		**3.4**	
Simulate PD algorithm to find achievable image restoration		Simulate DM control with results from step 2 and add drifts		Convolve simulation scene with resulting PSF and add noise		Calculate PSF estimate via PD in FORTA		Deconvolve noisy imagery and assess image quality	

4		**4.1**		**4.2**		**4.3**		**4.4**	
Simulation of PD algorithm for DM control		Simulate PD as in step 3.1 to 3.3		Simulate control signal to DM as obtained from PD WF estimate.		Repeat step 4.1 and 4.2 until convergence		Assess resulting optical performance	

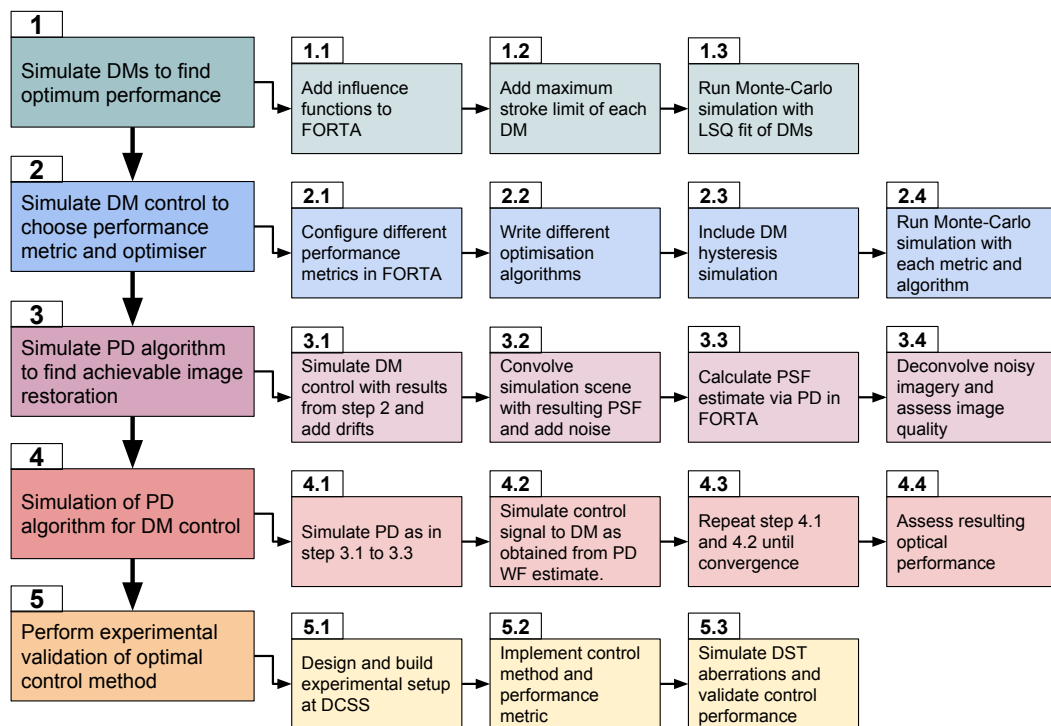| **5**		**5.1**		**5.2**		**5.3**	
Perform experimental validation of optimal control method		Design and build experimental setup at DCSS		Implement control method and performance metric		Simulate DST aberrations and validate control performance	

Figure 5.20: Research steps required for determining the optimal DM, control algorithm, performance metric and PD control viability.

6

Simulating Deformable Mirrors for Ray Tracing

Three aberration correction system (ACS) concepts are selected for more analysis in the previous chapter. These concepts are *LowReqs*, *PDDrift* and *PDControl*. All these concept use a deformable mirror in the DST exit pupil. Hence, to be able to simulate the performance of these systems, realistic DM models are developed as an extension to the FORTA software. The theory and implementation of the models is described in this chapter, while the simulated performance of the different ACS control algorithms is described in Chapter 7.

Section 6.1 provides a description of the mathematical PDM model for FORTA. Section 6.2 treats the simulation of an existing Alpao DM with this PDM model to validate its performance in comparison with a Gaussian function fit. With the validated model, a TNO DM prototype is simulated. This simulation is treated in Section 6.3, together with an optimisation of the actuator pattern for this DM. For the MDM, a model based on Zernike functions is described in Section 6.4, with an implementation for the CILAS MDM in Section 6.5. Finally, the analytically ideal performance of the DMs in the DST is provided in Section 6.6.

6.1. Opto-mechanical Model of a Free Edge Faceplate DM

To find the optical correction capabilities of a free edge faceplate DM, a model has been developed, based on existing plate bending theory. To describe small deflections of a thin circular plate that is under the influence of forces on certain points, analytical equations from Loutye [68] can be used. This source cannot be accessed any more, but the full set of equations is given by Loktev, De Lima Monteiro and Vdovin in [24], where it is used to compare different types of DM. The model has been validated by Apollonov et al. in two papers [69, 70].

Let ζ and z be complex coordinates and $\bar{\zeta}$ and $\bar{z}$ their complex conjugates. Then the polar coordinates (r, φ) of a point can be transformed to complex coordinates via $z = r \cos \varphi + ir \sin \varphi$.

The influence of a force P at location ζ on the deformation S at location z of the circular plate depends on the analytical derivative S_p:

$$
\begin{aligned}
S_p(z, \zeta) = (z - \zeta)\left(\bar{z} - \bar{\zeta}\right) & \Big\{ \ln(z - \zeta) + \ln\left(\bar{z} - \bar{\zeta}\right) \\
& + \frac{1 - \nu}{3 + \nu}\left[\ln\left(1 - z\bar{\zeta}\right) + \ln\left(1 - \bar{z}\zeta\right)\right] \Big\} \\
& + \frac{1 - \nu^2}{(1 + \nu)(3 + \nu)} z\bar{z}\zeta\bar{\zeta} + \frac{8(1 + \nu)}{(1 - \nu)(3 + \nu)} \\
& \cdot \Big[\left(1 - z\bar{\zeta}\right)\ln\left(1 - z\bar{\zeta}\right) + k\left(z\bar{\zeta}\right) \\
& + \left(1 - \bar{z}\zeta\right)\ln\left(1 - \bar{z}\zeta\right) + k\left(\bar{z}\zeta\right)\Big].
\end{aligned}
\tag{6.1}
$$

59

Where v is the Poisson's ratio of the material and the function $k(x)$ is a logarithmic integral, equal to the negative second-order polylogarithm function $\text{Li}_2(x)$:

$$k(x) = \int_0^x \frac{\ln{(1 - \tilde{x})}}{\tilde{x}} d\tilde{x} = -\text{Li}_2(x). \tag{6.2}$$

To increase the FORTA ray trace calculation speed with respect to the original form, equation 6.1 is rewritten to take into account the cancelling imaginary terms and doubling of real terms:

$$\begin{aligned}
S_p(z,\zeta) = \text{Re}\Big[2 \, (z - \zeta) \, (\bar{z} - \bar{\zeta}) \Big\{ \ln{(z - \zeta)} \\
+ \frac{1 - v}{3 + v} \ln{(1 - z\bar{\zeta})} \Big\} \\
+ \frac{1 - v^2}{(1 + v)(3 + v)} z\bar{z}\zeta\bar{\zeta} + \frac{16(1 + v)}{(1 - v)(3 + v)} \\
\cdot (1 - z\bar{\zeta}) \ln{(1 - z\bar{\zeta})} + k\left(z\bar{\zeta} \right) \Big].
\end{aligned} \tag{6.3}$$

The actual deflection magnitude depends on the magnitude of the force P and the bending stiffness D of the plate,

$$D = \frac{Et^3}{12(1 - v^2)}, \tag{6.4}$$

where E is the Young's modulus of the material and t the plate thickness. Furthermore, a piston offset, tip orientation and tilt orientation of the plate need to be added to the analytical deformation function. Finally, the full plate deformation S is given by [68] as

$$S(z) = \frac{1}{16\pi D} \sum_{i=1}^N P_i S_p(z,\zeta) + S_0 + S_1 \text{Re}(z) + S_2 \text{Im}(z), \tag{6.5}$$

where N indicates the number of actuators.

In case multiple actuators are considered, the vector $\mathbf{x}$ is given by the actuator forces and orientation coefficients

$$\mathbf{x} = \left[cP_1, cP_2, \ldots, cP_i, S_0, S_1, S_2 \right]^T, \tag{6.6}$$

where c is used to denote the rigidity coefficient $\frac{1}{16\pi D}$. Influence function matrix $\mathbf{C}$ is given by a repetition of eq. 6.5 for all M coordinates z to be evaluated:

$$\mathbf{C} = \begin{bmatrix} S_p(z_1,\zeta_1) & S_p(z_1,\zeta_2) & \ldots & S_p(z_1,\zeta_N) & 1 & \text{Re}(z_1) & \text{Im}(z_1) \\ \vdots & & & & & & \\ S_p(z_M,\zeta_1) & S_p(z_M,\zeta_2) & \ldots & S_p(z_M,\zeta_N) & 1 & \text{Re}(z_M) & \text{Im}(z_M) \end{bmatrix} \tag{6.7}$$

and hence, it determines the relation between actuator forces and local mirror deflections.

6.1.1. Resulting deflection from actuator control

With the equations above, the response of the mirror to a given control signal can be found. With this model, the closed-loop mirror control procedure can be simulated in FORTA.

The forces that determine the mirror shape cannot directly be controlled in reality: not only do they depend on the actuator control signal, but also on the mirror shape and stiffness. Therefore, the *zero-load actuator deflections* $\left[\Delta_1, \ldots, \Delta_N \right]^T$ are chosen as model input. This keeps the model generally applicable for different types of actuators. The zero-load actuator deflection is defined here as the change in actuator dimension, normal to the flat mirror surface, in case no forces or pressures are applied on the actuator. See Figure 6.1 for a graphical representation.

Model for static equilibrium

The equilibrium of forces on the actuator requires that the force exerted on the mirror plate equals the force caused by the elastic deformation of the actuator. Hence, local mirror deflection S_{ζ_i} and zero-load actuator deflection Δ_i are related via:

$$P_i = k_{act} \left(\Delta_i - S_{\zeta_i} \right), \tag{6.8}$$

where k_{act} is the actuator stiffness. See Figure 6.1 for a graphical explanation. Mirror deflection S_{ζ_i} can now be found as a function of forces $\mathbf{P}$ by substitution of eq. 6.5. For N actuators, this yields N equations. However, $N + 3$ equations are required to find the unknown forces and piston, tip, and tilt coefficients. Therefore, three mechanical equilibrium conditions must be applied that guarantee that the sum of forces and moments are zero. These conditions are added to the matrix equation in rows $N + 1$ to $N + 3$. Altogether, this gives

$$\mathbf{S_p x} = \mathbf{\Delta}, \tag{6.9}$$

where $\mathbf{x}$ is the vector of scaled forces and coefficients as defined in eq. 6.6. The zero-load deflection vector $\mathbf{\Delta}$ is appended with the conditions for zero resulting forces and moments,

$$\mathbf{\Delta} = \left[\Delta_1, \dots, \Delta_N, 0, 0, 0\right]^T, \tag{6.10}$$

and $\mathbf{S_p}$ is given by the $N + 3$ equilibrium conditions for the actuators and general plate orientation;

$$\mathbf{S_p} = \begin{bmatrix} S_p\left(\zeta_1, \zeta_1\right) + \frac{1}{ck_{act}} & \dots & S_p\left(\zeta_1, \zeta_N\right) & 1 & \mathrm{Re}(\zeta_1) & \mathrm{Im}(\zeta_1) \\ \vdots & \ddots & & & & \\ S_p\left(\zeta_N, \zeta_1\right) & \dots & S_p\left(\zeta_N, \zeta_N\right) + \frac{1}{ck_{act}} & 1 & \mathrm{Re}(\zeta_N) & \mathrm{Im}(\zeta_N) \\ 1 & \dots & 1 & 0 & 0 & 0 \\ \mathrm{Re}(\zeta_1) & \dots & \mathrm{Re}(\zeta_N) & 0 & 0 & 0 \\ \mathrm{Im}(\zeta_1) & \dots & \mathrm{Im}(\zeta_N) & 0 & 0 & 0 \end{bmatrix}. \tag{6.11}$$

With this complete set of equations, the actuator forces and orientation coefficients can be found via

$$\mathbf{x} = \mathbf{S_p}^{-1}\mathbf{\Delta}, \tag{6.12}$$

with which the equilibrium mirror deflections $\mathbf{S}$ on coordinates $\mathbf{z}$ can be found for any zero-load control signal with

$$\mathbf{S} = \mathbf{C} \cdot \mathbf{x} = \mathbf{C}\mathbf{S_p}^{-1}\mathbf{\Delta}, \tag{6.13}$$

where $\mathbf{C}$ is defined as in eq. 6.7. So, with eq. 6.13, the mirror responses can be found when a control signal is given.

Computational cost

Since the ray trace simulation of the DM shape optimisation in FORTA requires multiple iterations of the above functions, the computing time needs to be minimised. It is found that the numerical calculation of eq. 6.2 with the built-in Matlab function `polylog(n,x)` is limiting the model performance, taking ca. 50 seconds for a 256×256 matrix of coordinates. Therefore, a polylogarithm function is written, based on the series expansion definition[1]:

$$\mathrm{Li}_2(x) = \sum_{n=1}^{\infty} \frac{x^n}{n^2}. \tag{6.14}$$

To investigate the effect of a finite number of terms on the speed and accuracy of the calculation for large matrices, a performance test is done for 1024×1024 coordinates x in the complex plane, with a mirror radius of $0.1\,\mathrm{m}$. The results of this test are shown in Figure 6.2. It can be seen that five terms are sufficient to achieve a relative accuracy of more than 10^{-4} %. When more than thirteen terms are used, accuracy is not improving any more, due to the limited machine precision. The required time increases approximately linearly with the number of terms. This information can be used to optimise FORTA simulations in the next steps of the process. For the Monte-Carlo simulations presented in Chapter 8, the number of terms is set to two for increased simulation speed.

---

[1]National Institute of Standards and Technology, Digital Library of Mathematical Functions. http://dlmf.nist.gov/25.12

6.1.2. Least-squares fit of PDM surface

To evaluate the best fit of a given mirror to a given target deflection, a system with $N + 3$ degrees of freedom can be set up for any point z. For a vector of known target deflections $\mathbf{S}_{target}$, the required zero-load actuator deflections and resulting surface shape can be approximated via a constrained least-squares optimisation. The target is to minimise the sum of the squares of the errors between the target deflection and true deflection:

$$\underset{\boldsymbol{\Delta}}{\text{minimise}} \quad \left\| \mathbf{C}\mathbf{S_p}^{-1}\boldsymbol{\Delta} - \mathbf{S}_{target} \right\|_2^2$$
$$\text{subject to} \quad \mathbf{A}_{eq} \cdot \boldsymbol{\Delta} = \mathbf{b}_{eq}$$
$$lb \le \boldsymbol{\Delta} \le ub$$

An additional constraint is that the sum of forces and two sums of moments must be zero. These constraints are given in matrix $\mathbf{P}_{eq}$. Hence:

$$\mathbf{P}_{eq} = \begin{bmatrix} 1 & ... & 1 \\ \text{Re}(\zeta_1) & ... & \text{Re}(\zeta_N) \\ \text{Im}(\zeta_1) & ... & \text{Im}(\zeta_N) \end{bmatrix}, \mathbf{b}_{eq} = \begin{bmatrix} 0 \\ 0 \\ 0 \end{bmatrix}, \tag{6.15}$$

where the force constraints can be translated to zero-load deflection constraints via

$$\mathbf{A}_{eq} = \mathbf{P}_{eq}\mathbf{S_p}^{-1}. \tag{6.16}$$

To prevent unrealistic solutions, the solution $\boldsymbol{\Delta}$ is limited to lower bound vector lb and upper bound vector ub. These vectors contain the minimum and maximum zero-load deflections allowed by the actuators.

In Matlab, the command `Delta = lsqlin(C*pinv(Sp),S_target,[],[],Aeq,beq,lb,ub)` has been used to implement the optimization with the inputs described above[2]. Initially, when the rigidity coefficient c was placed in the matrix $\mathbf{C}$, it was found that this led to very small matrix elements and prevented convergence of the optimization algorithm. Relocating this scaling factor to the output vector resolved this issue, but this requires the resulting forces to be scaled back by the same constant.
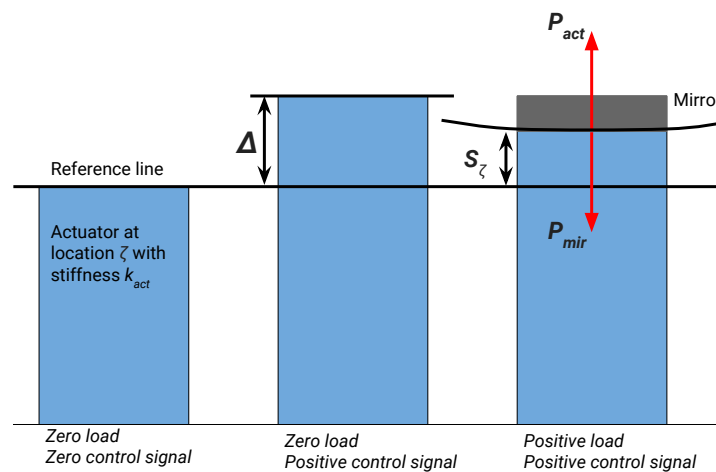

Figure 6.1: Model of an actuator on a plate deformable mirror (PDM). The forces imposed by the deflected mirror and deformed actuator are equal in magnitude and opposite in direction, see equation 6.11

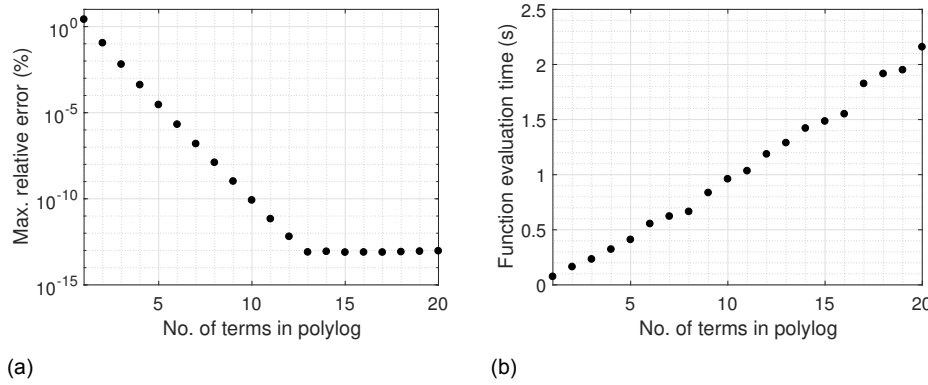[2]Documentation on: `https://nl.mathworks.com/help/optim/ug/lsqlin.html`

Figure 6.2: Left: sensitivity analysis of the number of polylogarithm terms from eq. 6.14 on the surface shape for a point on the complex plane within a distance 0.1 from the origin. The maximum error decreases rapidly, until machine precision is reached at 13 summation terms. Right: Time required for the function to calculate output for a 1024 × 1024 point grid.

6.2. Validation of PDM model with Alpao DM

The PDM model can be matched to the parameters of existing mirrors, to ensure a realistic mirror behaviour is simulated in FORTA. In this section, the model of the Alpao DM is used to validate the PDM model, while the next section treats the simulation of the TNO DM. Firstly, the basis functions used for fitting the known influence functions are determined. Secondly, a validation test of the PDM model is treated.
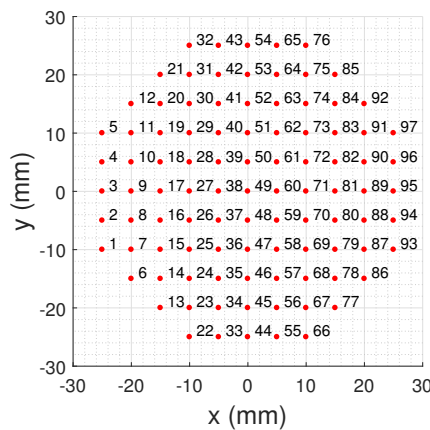

Figure 6.3: Actuator map and numbering scheme of the Alpao DM97-50, with 97 actuators and 50 mm mirror diameter. Actuator coordinates are taken from the Alpao DM97-15 mirror and scaled by a factor 50/15 to achieve an increased DM diameter, so that it can be used in an adapted DST design.

6.2.1. Comparison between Gaussian and PDM model basis functions

Because measured influence functions from the Alpao DM97-15 were received from the manufacturer, a fit can be made in FORTA between the measured functions and the basis functions for modelling the DM.

Some manufacturers, such as Xinetics, mentioned in correspondence that the influence functions of their DM can be approximated by two-dimensional Gaussian functions. However, as shown in Section 6.1, a different set of equations for plate bending can also be used. Therefore, both a Gaussian fit and a PDM model fit are tried on the influence function of an actuator on the Alpao DM. See Figures 6.4 and 6.5 respectively.

From these figures, it is concluded that both sets of basis functions do not fully described the Alpao mirror behaviour. However, both sets of basis functions are two orders of magnitude faster to use in ray tracing than a 2D-interpolation of measured influence functions.

One big advantage of the PDM basis functions over the Gaussian functions, is that the PDM model physically takes into account piston, tip, and tilt. Therefore, when all actuators receive the same input signal, the PDM model shows a resulting piston motion, while the Gaussian approach results in a surface consisting of bumps. Considering this, the PDM model is chosen for the simulation of deformable mirrors with a face sheet.
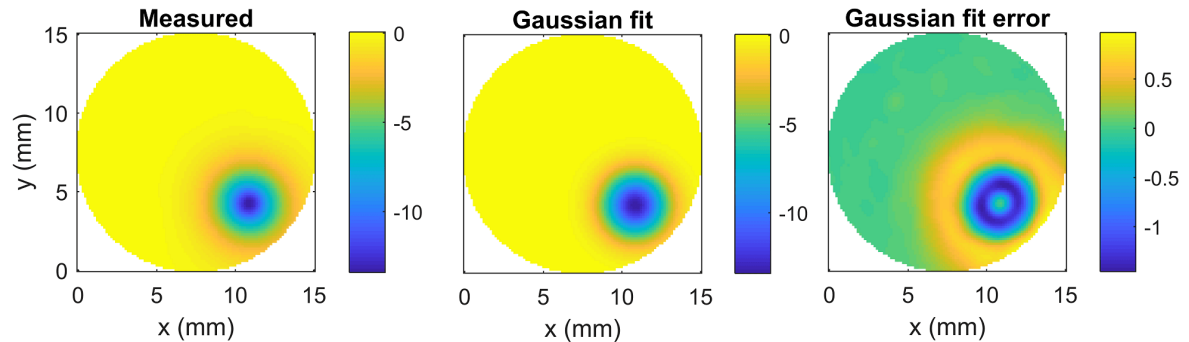

Figure 6.4: Example of the Gaussian function fit to a response function of the Alpao DM97-15. Left: measured wavefront when actuator no. 69. is activated (data from manufacturer). Middle: fitted two-dimensional Gaussian function. Right: fitting error of the function. The optimisation parameters are: location of the peak, amplitude and standard deviations in X- and Y-direction. Colorbar units are relative and scale with actuator input.
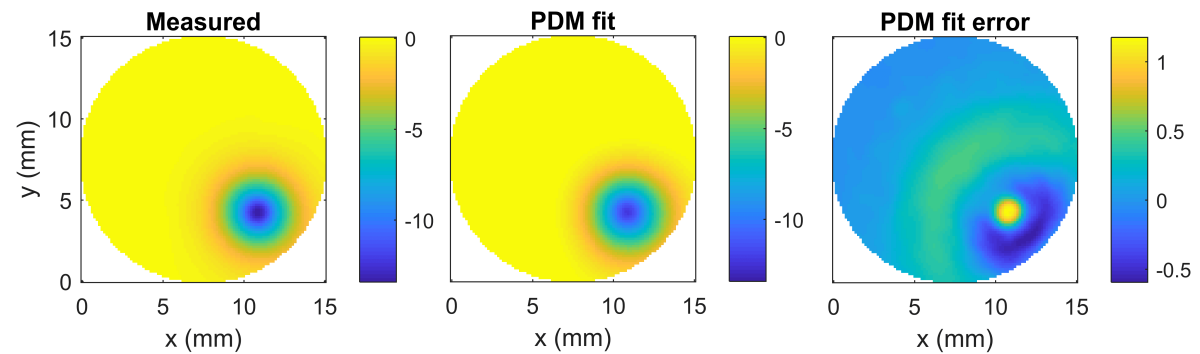

Figure 6.5: Example of the PDM function fit to a response function of the Alpao DM97-15. Left: measured wavefront when actuator no. 69. is activated (data from manufacturer). Middle: fitted PDM surface, with equations from Section 6.1. Right: fitting error of the function. The optimisation parameters are: membrane thickness, actuator stiffness and zero-load deflection of the active actuator. Colorbar units are relative and scale with actuator input.

6.2.2. Validation of PDM model by comparison with measurements

For the PDM fit, an optimisation has been performed to ensure the modelled parameters match the true design parameters as closely as possible, while the fitting error is minimised. The fitting error is defined as the maximum peak-to-valley deformation error, w.r.t. the true peak-to-valley deformation.

Information about the Alpao design parameters have been obtained from a patent [71]. From this, it is found that the face sheet consists of silicon with a thickness of 5 μm to 30 μm. Bulk silicon has a Poisson's ratio of 0.22 and a Young's modulus of 127 GPa. Furthermore, it is given that the actuators are placed on an evenly spaced rectangular grid of 1.5 mm × 1.5 mm.

For all 97 actuators on the up-scaled Alpao97-15 DM, an optimisation is performed with the PDM model and the MATLAB function `lsqcurvefit`. Besides the constraints given above, the actuator stiffness lower and upper limits are set at $10\,\text{N}\,\text{m}^{-1}$ to $1000\,\text{N}\,\text{m}^{-1}$ respectively. Subsequently, all 97 optimisations yield slightly different optimal PDM parameters. Therefore, parameters of the optimisation with the lowest PV-error are considered to be the "true" parameters.

Table 6.1 shows the parameters that result in the lowest surface fit error. Next to the 15 mm diameter mirror, also a 50 mm diameter mirror has been simulated. Such a mirror is also usable in the DST exit pupil and planned as a future Alpao product. The company advises to simulate their future DM

with 50 mm diameter by scaling the influence function domain, but not the range of the 15 mm mirror. Hence, the scaled measurements and a fitted model are shown in Figure 6.6 For actuator 1, note that

Table 6.1: Parameters retrieved from optimisation of the fit of the PDM fit for the Alpao97-15 mirror and the up-scaled version with the same deformation amplitudes and shapes.

Parameter	Symbol	Dia. 15 mm	Dia. 50 mm
Peak zero-load deflection	$\Delta_{0,max}$	60 µm	60 µm
Face sheet thickness	t	29 µm	68 µm
Actuator stiffness	k_{act}	225 N m^{-1}	272 N m^{-1}
Poisson's ratio	ν	0.22	0.22
Young's modulus	E	127 GPa	127 GPa

the difference between the scaled measurement and the PDM model is quite large. The suspected reason for this is the difference between the measured actuator grid and the given grid: the maxima of the measured functions form a warped grid, instead of a rectangular grid. This is likely caused by the measurement technique used by Alpao. Therefore, direct comparison between the measured and calculated influence functions may not be suitable.

(a) Actuator 1

(b) Actuator 49
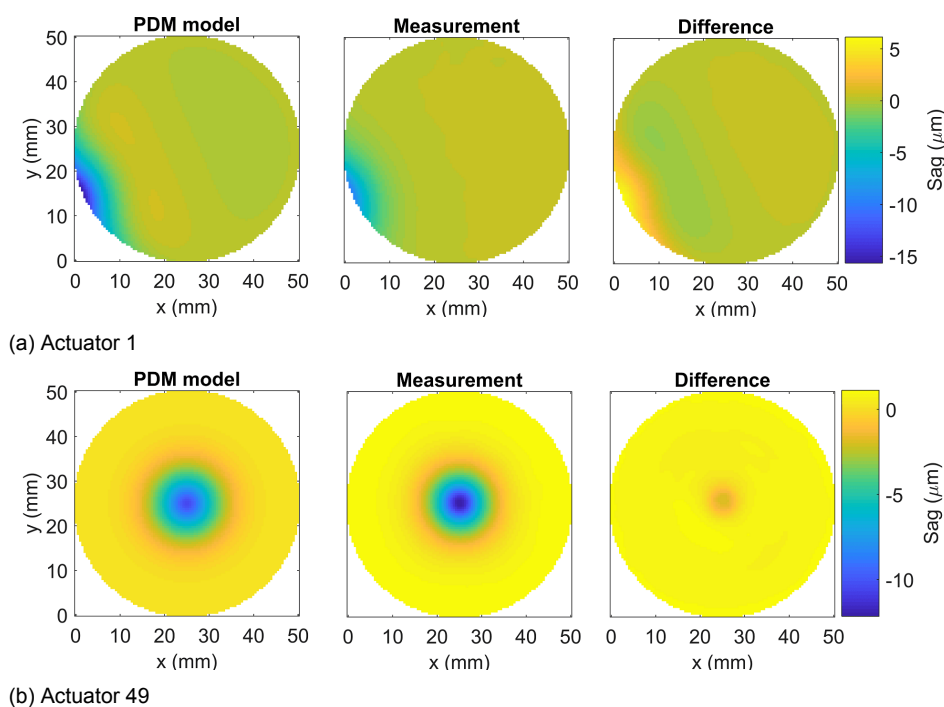
Figure 6.6: True response and modelled response of the Alpao DM97-50. Measurement responses are scaled from reponses of a 15 mm diameter DM, while modelled responses are generated with a PDM model that showed a best-fit for the central influence functions.

6.3. Simulation and Layout Optimisation of TNO PDM

While the Alpao DM offers an interesting case study for PDM model validation, the DM developed by TNO is more relevant for the DST project. Not only is this DM more easy to customise, it is also developed for space applications [30]. Therefore, the next parts of this report use an optimised TNO PDM as reference model. This subsection treats the details of the existing TNO PDM prototype and the corresponding FORTA PDM model.

6.3.1. PDM model based on TNO prototype

Measurements on the existing TNO prototype shown in Figure 5.8 indicate a PV deformation of 40 μm and an inter-actuator stroke of 11 μm [30]. With the known prototype parameters of the face sheet and actuator spacing, the actuator stiffness is the only unknown. It is found that a stiffness of 0.35 N μm^{-1} results in the desired PDM prototype model behaviour, which can be seen in Figure 6.7.

Table 6.2 shows the resulting design parameters of the TNO DM prototype and the corresponding FORTA PDM model that is treated in this section. While the actuator stiffness and face sheet thickness differ for both mirror models, the increase in stiffness ratio t^3/k_{act} is just 2.28 times larger for the real prototype then for the FORTA model. In the next subsections, it is shown that the actuator spacing is decreased from 18 mm in the real prototype to ca. 8 mm for the optimised FORTA DM. This increased actuator density almost entirely cancels the stiffness difference, such that the domain and amplitude of the influence functions is very comparable for both mirrors.

Table 6.2: Parameters comparison between the TNO PDM prototype and the FORTA model. Although a different actuator stiffness and face sheet thickness are used in FORTA, the behaviour is comparable due to equal scaling of the stiffness ratio and actuator spacing [30].

Parameter	Symbol	TNO Prototype	FORTA PDM model
Aperture radius	r	100 mm	40 mm
Actuator spacing	d	18 mm	Optimised[3]
Peak force at surface	F_{max}[1]	7 N	N/A[2]
Peak zero-load deflection	$\Delta_{0,max}$[(2)]	20 μm	31 μm
Face sheet thickness	t	1 mm	51 μm
Actuator stiffness	k_{act}	350 000 N m^{-1}	100 N m^{-1}
Poisson's ratio[4]	ν	0.17	0.17
Young's modulus[4]	E	72 GPa	72 GPa

[1]The actuator itself delivers twice this force when some non-linearity is allowed, but since it is connected to a mechanical lever, the force on the DM surface is half of the actuator force. The peak force can be assumed to scale with the square of the actuator spacing.
[2]The true TNO DM uses currents as input signals, which are related to forces rather than the zero-load deflections commanded in FORTA. However, when this zero-load value is used in the FORTA PDM model, it delivers the same maximum force as the true actuator would do.
[3]See following subsections
[4]The prototype uses a fused silicon face sheet

(a)   (b)
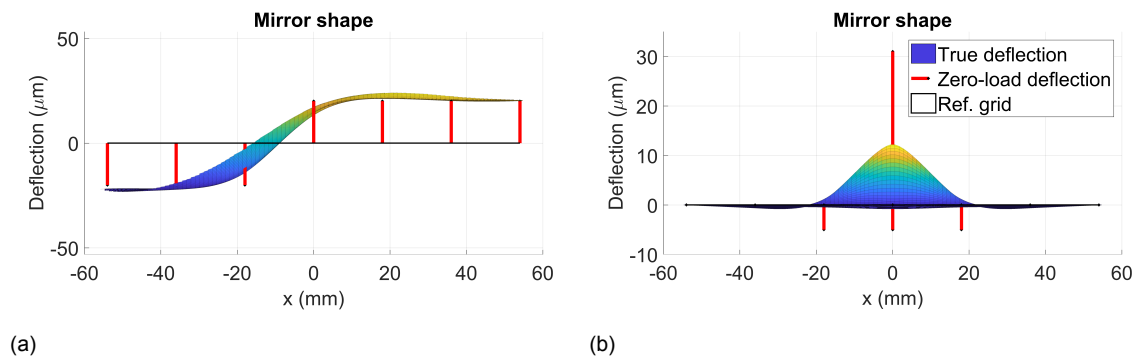
Figure 6.7: Behaviour of the prototype TNO DM as a FORTA PDM model. (a): Peak-to-valley stroke when the actuator control force is maximum. (b) When a the maximum zero-load stroke of ±31 μm is given as command to the central actuator, it delivers maximum force of 7 N at the surface. As a result, the total inter-actuator deflection is ca 11 μm. This agrees with true numbers from [30]. Zero-load deflection is the deflection if the actuator has stiffness, but no face sheet would be present. The modelled TNO prototype parameters are shown in Table 6.2

.

6.3.2. Actuator count optimisation for the entire optical field

To find the ideal number of actuators across the PDM, an optimisation is performed in which the actuators are placed in a simple rectangular grid. The figure of merit for the DM then is the mean Strehl ratio that can be achieved over the primary detector, assuming a least-squares fit of the influence functions of the actuators. From Figure 6.9, it can be seen that an increase in the number of actuators from three
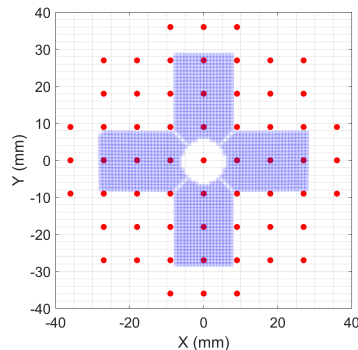

Figure 6.8: TNO DM actuator count example and exit pupil visualisation. The blue dots indicated the coordinates of the ray trace simulation for the central field of TDI 1. The red dots indicate the TNO DM actuator locations. In this case, there are 9 actuators across the mirror diameter.

to seven strongly improves the maximum theoretical performance of the TNO DM. Beyond this, the effect of adding actuators diminishes.

When looking at the differences between figure (a) and (b), it can be observed that the expected achievable Strehl ratio in the central field is above 0.95, in case there are seven actuators or more across the DM diameter. However, the outer field lacks this performance: cases with a Strehl ratio below 0.8 are not uncommon, and outliers down to a Strehl ratio of 0.6 can be found.

A closer look is taken at the outliers in the outer-field. It is found that the most extreme outlier, with a Strehl ratio below 0.6 in most cases, is caused purely by field-dependent aberrations: in the central field, the Strehl ratio is above 0.9, hence the DM optimisation did not fail. Furthermore, M1 segment phasing is also successful. Therefore, it seems that DM shape optimisation to one specific OPD can lead to a large variation in Strehl ratio over the field of view.

To investigate the sensitivity of the results to the location of the OPD, a weighted average of the central field OPD and outer field OPD is taken, according to the values provided in Table 6.3. The trial is repeated for relative OPD weights of 1/0, 0/1, 0.5/0.5/ and 0.3/0.5. It can be seen in the table that, for this case, a weighted average of 0.3 times the central field OPD and 0.7 times the outer field OPD results in the most balanced performance over the field of view.

The 0.3/0.7 weights for the central and outer field OPD are applied to the fitting procedure of the TNO DM to find the new performance spread. The cases for 6 to 10 actuators are re-run. The results are shown in Figure 6.10. It can be seen that the expected optical performance for the central and outer fields is now nearly equal, as opposed to the large difference seen in the previous results. With seven or more actuators across the 80 mm TNO DM, both the central field and outer field can achieve a Strehl ratio above 0.8.

In the real system, it is not possible to directly command the DM to a weighted OPD, as the OPD is not directly measured. Therefore, it is suggested that a weighted sharpness optimisation can be used instead; the sharpness optimisation treated in 8.1 should then be applied to subimages from different locations of the cross-track field of view.

6.3.3. Actuator layout optimisation

As shown above, with the theoretical PDM model and a Monte-Carlo analysis with the tolerances from Table 4.1, it is found that at least 7 actuators across the exit pupil diameter are required to reach an average Strehl ratio of above 0.9 on the entire field of the primary detector of the DST. To maximise the performance of the PDM for this given number of actuators, geometry optimisation of actuator locations is performed.
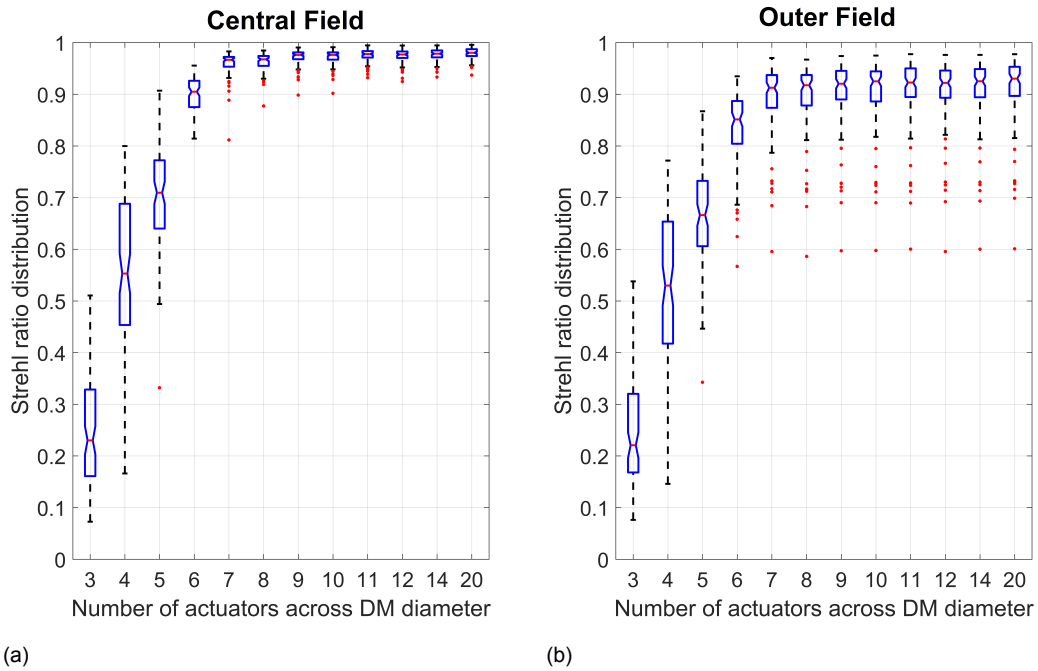
Figure 6.9: TNO DM actuator count optimisation. Theoretically achievable Strehl ratio distribution on TDI 1 when the DM is deformed to remove the central field OPD. Central field (a) and outer field (b). Simulation with 100 trials, of which 9 outliers are removed. These are caused by M1 phasing errors (discontinuities larger than 225 nm). The range of the boxes in the plot contains 50% of the data, the whiskers contain ca. 99% of the data.
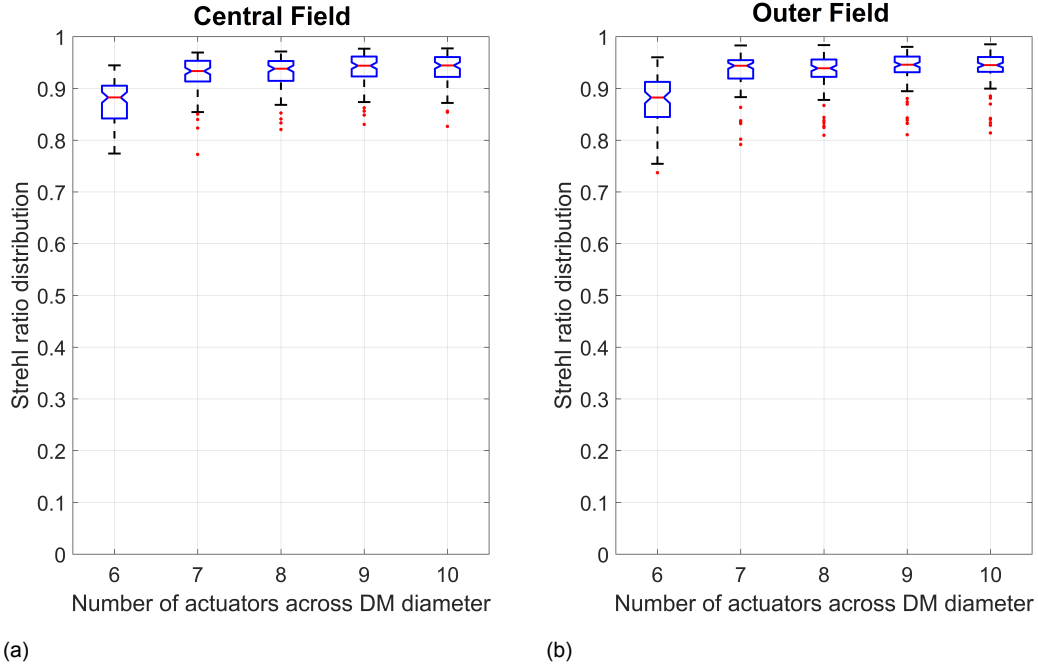
Figure 6.10: Theoretically achievable Strehl ratio distribution on TDI 1 when the DM is deformed to compensate for a weighted average of the central field OPD and outer field OPD. Performance on central field (a) and outer field (b). Simulation with same cases as in Figure 6.9. The Strehl ratio variance increases for the central field, but remains above the required value of 0.8. The Strehl ratio variance on the outer field has become lower and also meets this performance criterion now. The range of the boxes in the plot contains 50% of the data, the whiskers contain ca. 99% of the data.

Table 6.3: The case that produced the strongest outlier in Figure 6.9(b) has been investigated in more detail. It is found that the performance differences, caused by field-dependent aberrations, can be minimised by fitting the DM shape to a weighted average of the OPD data.

Weight central OPD	Weight outer OPD	Strehl central	Strehl outer
1	0	0.94	0.60
0	1	0.71	0.88
0.5	0.5	0.88	0.78
0.3	0.7	0.82	0.83

For this optimisation, a random walk algorithm is used. Nine variables describe the actuator layout: three actuators are constrained to the middle line of a projected M1 segment in the exit pupil, and three actuators are placed on one side of a projected segment. This results in 6 radial distances and 3 polar angles. An additional actuator is placed in the centre for optimal focus control. Due to symmetry along the long axis of each segment and between the segments, this set of variables fully constraints the 37 actuators on the DM aperture.

At each geometry optimisation iteration, the PDM model is used reduce the central field OPD of 100 reference telescopes in FORTA, each with different tolerances applied. The OPD reduction is performed by calculating a least-squares fit of the analytical influence functions w.r.t. the desired DM deformation. This desired deformation is again based on a weighted average of the OPD's at the central field and the extreme field.

Similar to the actuator count optimisation, the figure of merit for the actuator position optimisation is the mean Strehl ratio that can be achieved over the primary detector. On the 100 telescopes generated with a Monte-Carlo simulation, this actuator layout can theoretically achieve a mean Strehl ratio of 0.94 on the primary detector. See Figure 6.11. To achieve this result, ca. 400 random optimisation steps are tried, of which 20 to 40 steps per experiment lead to an increase in the DM performance (and hence a new layout). For the three cases shown in Figure 6.11, it is found that the performance of both mirrors with 40 mm radius is comparable and higher than the performance of the 32 mm radius DM, because the edge effects at the pupil can be taken into account. To avoid unnecessary complexity, it has been decided to select the 40 mm radius mirror with 37 actuators as the reference PDM model in FORTA. See figure 6.11 (b).

(a)   (b)   (c)
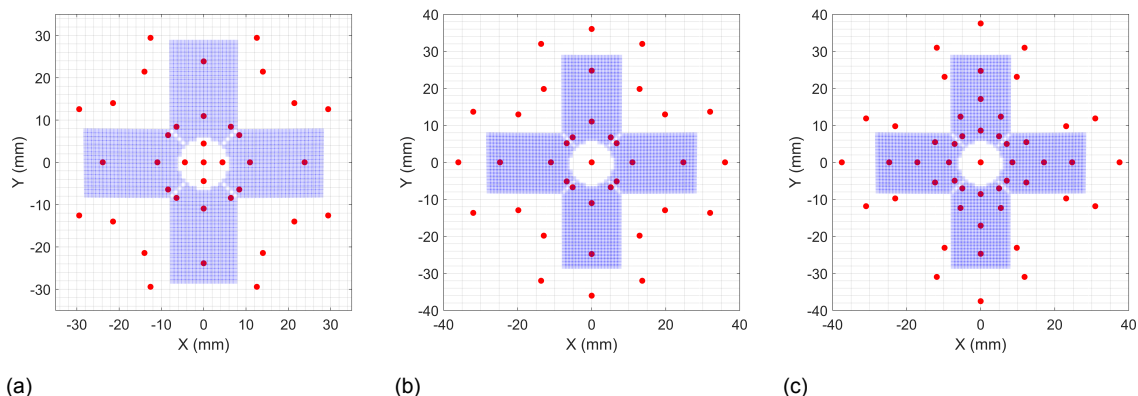
Figure 6.11: TNO DM layout optimisation result and exit pupil visualisation. The blue dots indicated the coordinates of the ray trace simulation for the central field of TDI 1. The red dots indicate the TNO DM actuator locations. In this case, there are 37 (a,b) or 49 (bottom) actuators on the DM. The 40 mm radius mirror with 37 actuators (b) has been selected as the reference PDM model in FORTA, for its high performance w.r.t. design (a) and and low complexity w.r.t. design (c).

6.4. Opto-mechanical Models for Membrane, Monomorph and Bi-morph DMs

In the previous section, a model has been presented for a continuous faceplate DM with push-pull actuators. This PDM model has been developed with the known influence functions. However, for a membrane deformable mirror (MDM), monomorph deformable mirror or bimorph deformable mirror, such generalised analytical influence functions are not available.

6.4.1. Membrane DM with electrostatic actuators

For an electrostatically actuated MDM, the local surface displacement $S(x, y)$ is related to the membrane tension T and surface pressure $p(x, y)$ via Poisson's equation, as shown by Grosso and Yellin [72]:

$$\nabla^2 S(x, y) = -p(x, y)/T. \tag{6.17}$$

For small displacements, the tension is not influenced and can be considered constant over the membrane. The surface pressure can be calculated, when the capacitor-membrane distance $S_0 - S(x, y)$, di-electric constant ϵ and voltage V are known;

$$p(x, y) = \frac{\epsilon V(x, y)^2}{2 \left(S_0 - S\left(x, y\right)\right)^2} \tag{6.18}$$

and hence,

$$\nabla^2 S(x, y) = -\frac{\epsilon V(x, y)^2}{2T \left(S_0 - S\left(x, y\right)\right)^2}. \tag{6.19}$$

For specific geometries and cases, Claflin and Bareket have developed an analytical model that is accurate for Zernike terms up to order 6 [73]. However, this model is not easily extended to general mirror designs. Therefore, numerical methods are required to find the mirror deflection S at a specific location.

6.4.2. Monomorph and bimorph mirrors

The shape of mono- and bimorph mirrors can also be described by Poisson's equation [74, 75], in the form

$$\nabla^4 S(x, y) + c_m \nabla^2 V(x, y) = 0, \tag{6.20}$$

where $S(x, y)$ is the surface displacement, $V(x, y)$ the voltage and c_m a constant, derived from the material properties [76]. The complex coupling between the mirror deformation and voltage of the piezoelectric material makes it difficult to establish a mathematical relation for constant c_m, so experimental measurements of the influence functions are considered the most practical approach for this type of mirror [74].

6.4.3. Practical implementation

It is shown that Poisson's equation describes both the MDM and mono-/bimorph DM. However, for practical use in raytracing software, the shape of the optical surface should be a function of any coordinates (x, y).

Numerical solution of Poisson's equation

Poisson's equation can be solved numerically with e.g. the successive over-relaxation algorithm, which was first described by Young in 1954 [77]. Example implementations for coding can be found in e.g. Press [78, Ch. 20]. For deformable mirrors that are to be developed, these equations and numerical methods can be useful to evaluate the behaviour of the mirror. However, for existing mirrors, measurements of the actuator influence functions are more accurate.

Description as a Zernike surface

When a deformable mirror is to be modelled for simulation in a raytracing code, a function that can be quickly evaluated for many different coordinates (x,y) is preferred above a numerical solution on a predefined grid. Therefore, when measured actuator influence functions are available, a fit with Zernike

polynomials is considered. The mirror deflection S can then be written as a function of control input $\mathbf{u_{act}}$.

Firstly, the measured or modelled influence function of each actuator i under a unit control input is fitted to N_{zern} Zernike polynomial terms, with a normalisation radius that is equal to the full DM radius. The resulting vector of relative Zernike weight coefficients is then set as column i of matrix $\mathbf{W_u}$. So, this matrix will be of size $N_{zern} \times N_{act}$, where N_{act} is the no. of actuators. Subsequently, when a control signal $\mathbf{u_{act}}$ is given to the DM, the response function can be modelled with a summation of Zernike polynomials with weights $\mathbf{w_{zern}}$;

$$\mathbf{w_{zern}} = \mathbf{W_u} \mathbf{u_{act}} \tag{6.21}$$

and since the Zernike functions are defined over the entire DM radius, they can be evaluated in the ray trace software directly, without the need to solve Poisson's equation. Note that $\mathbf{u_{act}}$ is different from the PDM control signal $\mathbf{\Delta}$, in the sense that $\mathbf{u_{act}}$ is applicable for a mirror of which the shape is described by a linear addition of the influence functions, while Δ is specifically described as the zero-load stroke of a push-pull actuator with finite stiffness in a PDM model.

When a fitted surface is used, a trade-off must be made between speed and accuracy. The higher the order of the Zernike polynomials, the lower the fitting error will become. On the other hand, the number of terms grows exponentially with the order,leading to a rapid increase in function evaluation time. So, the trade-off outcome depends on the required accuracy and speed of the simulation.

6.4.4. Least-squares fit of Zernike surface

For a PDM, it is shown in Subsection 6.1.2 that a control signal $\mathbf{\Delta}$ can be found via constrained least-squares optimisation. In case the DM is described as a linear combination of Zernike functions, the surface deflection $\mathbf{S}$ can be described by

$$\mathbf{S} = \mathbf{Z} \mathbf{w_{zern}} = \mathbf{Z} \mathbf{W_u} \mathbf{u_{act}}, \tag{6.22}$$

where $\mathbf{Z}$ is an $N_z \times N_{zern}$ matrix, where $Z_{i,j}$ contains the value of unit Zernike term j in N_{zern} to the (x_i, y_i) coordinate, with i in N_z.

In case the actuator control signals are not limited, the least-squares fit of a mirror, described by Zernike influence functions, to a target deflection $\mathbf{S_{target}}$, is given by

$$\mathbf{u_{act}} = (\mathbf{Z} \mathbf{W_u})^{-1} \mathbf{S_{target}}. \tag{6.23}$$

However, this is found to result in optimum control signals that are outside the bounds of the actuator. Therefore, a constrained least-squares optimisation is preferred. In Matlab, the constrained control signal can be found via e.g:
`u_act = lsqlin(Z*W,S_tar,[],[],[],[],lb,ub).` Where `lb` and `ub` contain the minimum and maximum allowed control signal value, respectively.

6.5. Simulation of CILAS MONO Mirrors

This section treats the simulation of existing MDMs for FORTA to evaluate the ideal performance and the closed-loop performance. In Table 5.1, it is shown that the CILAS company provides monomorph type deformable mirrors (abbreviated MDM) which may comply with the DST ACS requirements. The mirrors are being qualified for space applications [79] and have a low mass, which is why they are considered for modelling in FORTA.

As explained in Subsection 6.4.3, the most effective way to model a monomorph mirror is by using a a Zernike polynomial fit of the influence functions. For two different mirrors, the influence functions are provided by CILAS. The parameters of these mirrors are shown in Table 6.4. To assure the number

Table 6.4: Parameters of the CILAS mirrors used for simulation [36].

Parameter	Symbol	MONO63-87	MONO85-60	MONO85-70[1]
Aperture radius	r	43.5 mm	30 mm	35 mm
No. of actuators	n_{act}	63	85	85
Zernike terms for fit	n_{terms}	136	231	231

[1]This mirror does not currently exist, but is simulated by scaling the Zernike polynomials retrieved from a fit on the MONO85-60 mirror.

of Zernike terms is sufficient to accurately describe the DM surface, a sensitiviy analysis has been performed. The results of this analysis are presented in Figure 6.13. On the left, it shows the actuator locations for the CILAS MONO63-87 mirror. On the right, the relative RMS error is shown as a function of the Zernike polynomial order used for fitting the influence functions. Clearly, a fit of order 15 (121 terms) is sufficient for the RMS fitting error to reach below 0.02 μm and therefore, this number of fitting terms is selected. See also the influence function error in Figure 6.12. Even better would be to create a set of basis functions that are more comparable to the shape of the influence functions, see also Section 9.3.

Considering the CILAS MONO85-70 mirror, the number of terms is increased to 231 (20th order), as Table 6.4 shows. With these terms, an RMS fitting error of below 1×10^{-2} μm for all actuators is achieved, given a maximum sag amplitude of 2 μm to 7 μm. The reason that more terms are required, is that this DM has a larger number of actuators and a smaller actuator spacing, leading to increased spatial frequencies in the influence functions.
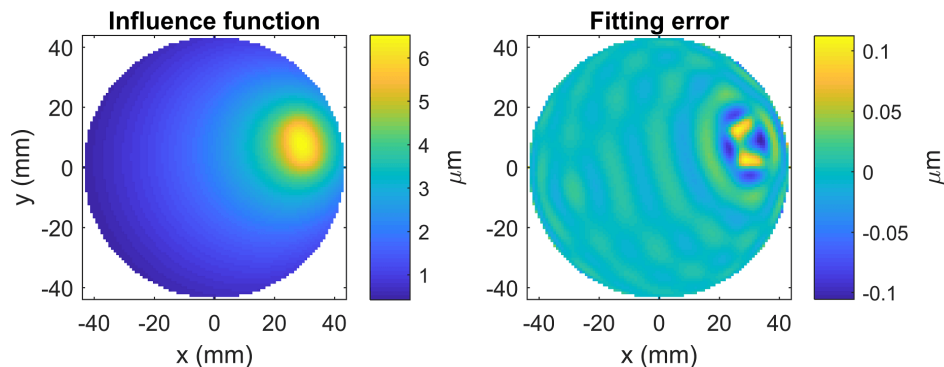

Figure 6.12: Left: influence function of CILAS MONO63-87, actuator no. 32, as provided by CILAS. Right: error of a Zernike polynomial fit of order 15 (136 terms).

Figure 6.14 shows the actuator layout of the CILAS MONO85-70 mirror (left), and a typical example of the DM deformation when two actuators are given the maximum positive and negative control signal (right). When comparing this behaviour with the PDM behaviour in e.g. Figure 6.7, it is clear that the curvature control done in the MDM causes a gradient deformation over the entire mirror, whereas the PDM only displays a local deformation. This can also be observed in Figure 6.12 (left). The result of this global DM surface gradient means that the zonal control variables are less independently controllable in terms of local deformation, such that the high number of actuators perhaps not guarantee fine zonal control per se.
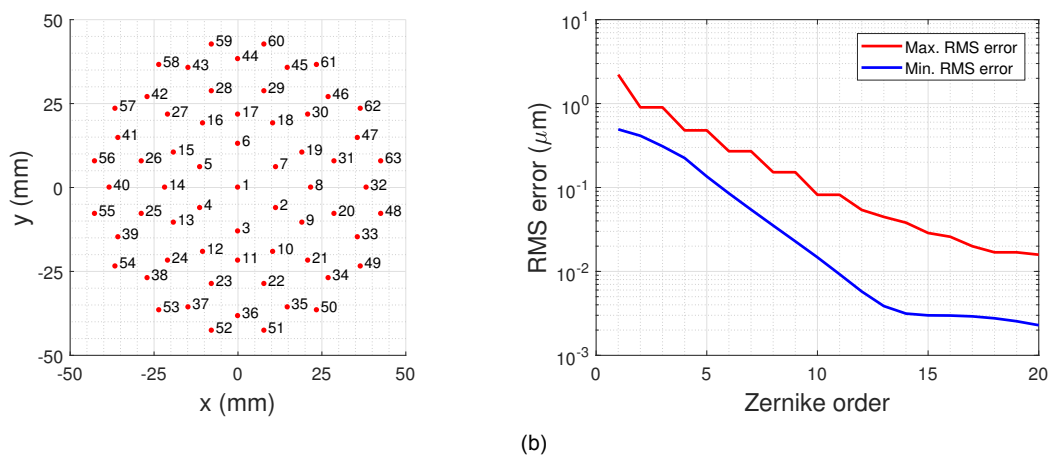
(a)

(b)

Figure 6.13: Left: Locations of influence function maxima CILAS63, corresponding to the locations of the respective actuators. Right: min. and max. RMS error as function of Zernike fit order n, for all 63 actuators of the CILAS MONO63 mirror.
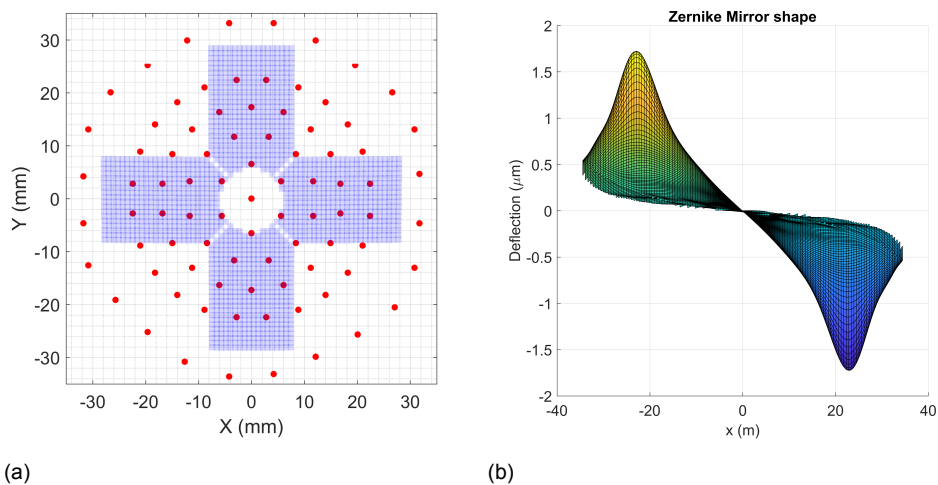

(a)

(b)

Figure 6.14: (a): Locations of influence function maxima CILAS85-70, corresponding to the locations of the respective actuators. (b): Typical mirror deformation when two actuators get a maximum positive and negative control signal, respectively. In contrast to the PDM model, the MDM shows a change in sag of the entire surface when a single actuator is activated.

6.6. Idealised Performance of Simulated Mirrors

With the optimised PDM model and the CILAS MDM model in FORTA, it is possible to assess the optical performance that these DMs may ideally achieve. Therefore, 100 Monte-Carlo simulation trials are performed to find the performance that the optimised FORTA PDM model (37 actuators) and the CILAS MONO85-70 model (85 actuators). To achieve an analytical best-fit, the theory presented in Subsections 6.1.2 and 6.4.4 is applied. The target deformation is taken with respect to the OPD on the central field of detector 1.

Taking into account the removal of 8 outliers caused by the M1 phasing process, the results are as shown in Figure 6.15. Clearly, the PDM and MDM both offer comparable optical behaviour in terms of maximum Strehl ratio, with a central field Strehl ratio of well above 0.9. Unfortunately, field-dependent aberrations clearly limit the performance at other fields. At the edge of TDI 1, the Strehl decreases to below 0.8 for some cases and on the outermost corner of the spectral sensor location it sinks below 0.6. These findings correspond well to those found in the preliminary experiment from Subsection 5.3.3. To
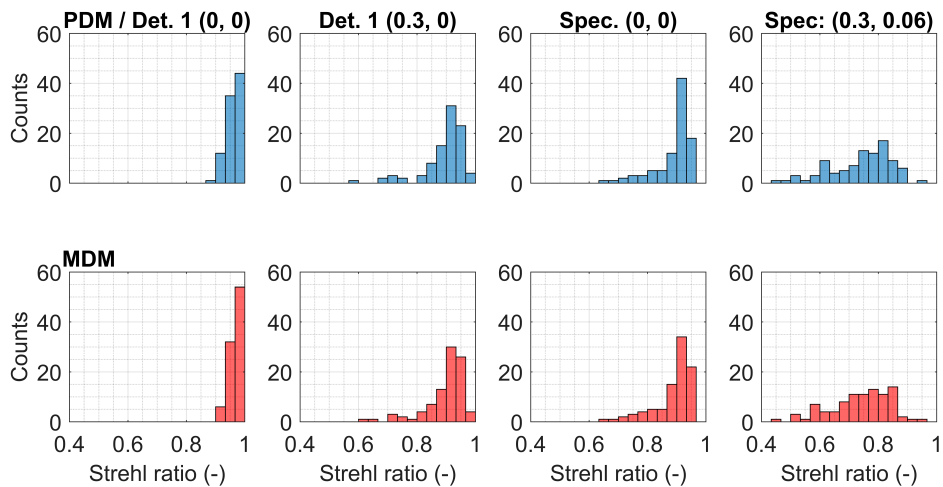
Figure 6.15: Strehl ratio on different detectors and fields on the DST focal plane, when the optimised FORTA PDM (top row) and CILAS85-70 MDM (bottom row) are least-squares fitted to the required deformation in the central field (0, 0) of TDI 1. See Figure 5.11 for an illustration of the fields and detectors.

illustrate the different behaviour of both DMs, figure 6.16 is created. The top row shows the original and reduced OPD for the central field of detector 1 and the magnitude and sign of the actuator signals that are required for a this fit. The bottom row shows this for the optimised PDM model. Note that the PV OPD is ca. 0.2λ after correction for both mirrors. However, the MDM uses 85 actuators instead of 37.

The middle bottom row figure shows that the PDM actuators cause so-called actuator print-through. This effect results in a local bump in the OPD. Print-through can be reduced by an increase in the face sheet stiffness, but this comes at the cost of increased actuator forces. However, for the case shown, the maximum MDM actuator signals were ca. 45% of the voltage limits. For the PDM, the maximum applied force is ca. 10% of the force limit.
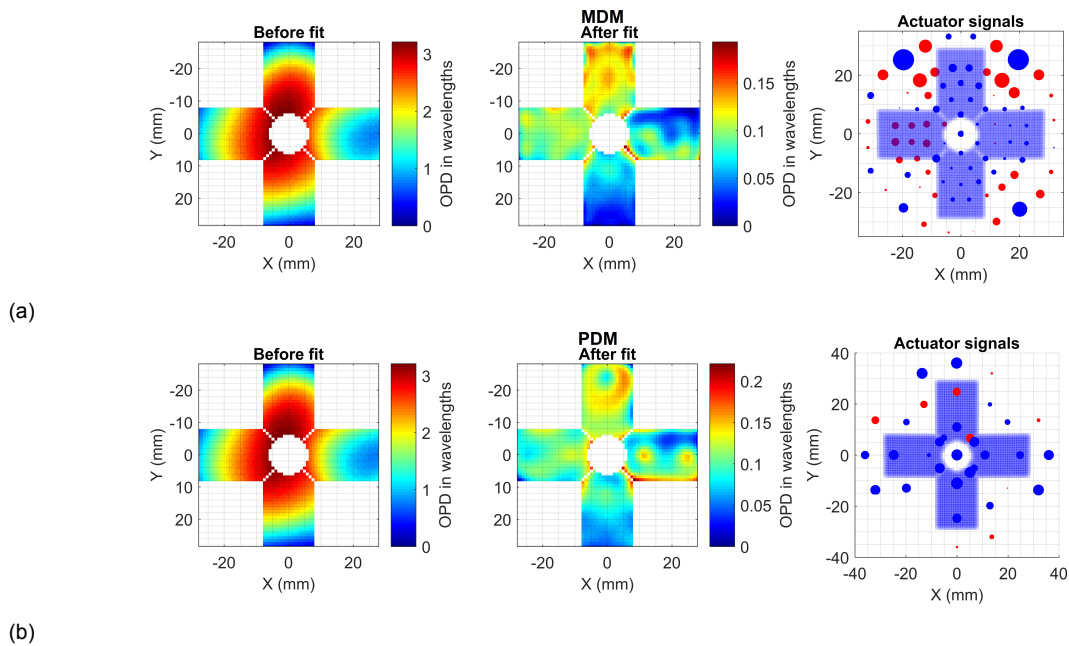
(a)

(b)

Figure 6.16: Correcting performance with least-squares fit. Red markers indicate a positive control signal, blue markers a negative control signal.(a): OPD before CILAS MDM fit, after MDM fit and the corresponding magnitude of the actuator signals. (b): OPD before PDM fit, after PDM fit and the corresponding magnitude of the actuator signals. Some actuator print-through effects can be observed at e.g. the right pupil segment. Negative actuator signals cause a concave deformation, positive signals cause a convex deformation.

7

Simulation of Control via Sharpness Optimisation

While the previous chapter introduced the different types of deformable mirror models and their analytically ideal performance, this chapter focuses on the simulation of realistic control of the mirrors in the context of the ACS.

This chapter contains four sections. The first section treats the simulation of modal and zonal control. The second section elaborates on the different algorithms that have been tested to find an applicable algorithm for control of the DM. The third section presents the sharpness optimisation method that has been selected. The fourth section of this chapter describes the implementation of this algorithm in the simulation.

7.1. Implementation of Modal and Zonal Control

As described in Section 5.5, the control variables that determine the mirror shape can be either modal or zonal. While zonal control is associated with local actuator deflections, modal control is performed on the global mirror shape.

Zonal control

If the mirror is controlled via zonal control variables, separate actuators or groups of neighbouring actuators are controlled to create a local deflection of the mirror surface. This choice will require the most optimisation iterations, because independent control for each actuator results in the largest number of control variables. On the other hand, this option also leads to the highest possible performance: local deformations caused by manufacturing tolerances or expansion due to thermal gradients can be removed directly. An example of zonal control for the TNO prototype PDM model is shown in Figure 6.7.

Modal control

When vector $\mathbf{u_{modal}}$ contains the modal control variables, the control signals to the actuators, $\mathbf{u_{act}}$ can be found with

$$\mathbf{u_{act}} = \mathbf{M}\mathbf{u_{modal}}, \tag{7.1}$$

where $\mathbf{u_{act}}$ is a column vector with N_{act} elements, or the number of actuators of the DM. $\mathbf{u_{modal}}$ has N_{modal} elements, the number of control modes. So, $\mathbf{M}$ is a matrix with dimension $N_{act} \times N_{modal}$. It contains the calibrated values that relate the unit modes to the required actuator responses. This matrix can be found column-by-column via the least-squares fitting methods described in Subsections 6.1.2 and 6.4.3 and implemented in the `OptimDM.m` function, listed in Appendix A.

To derive the required modal control signals, the DM models are calibrated for Zernike terms 1 to 36 (or the seventh order), as this is sufficient for coarse control according to the requirements discovery in Section 4.2. Subsequently, a Zernike term j is introduced as target OPD and with RMS value of 1λ. Therefore, the required RMS deflection of the mirror is 5λ, see eq. 3.6. As a result, the calculated control signal that gives the least-squares surface fit can be directly copied to column j of matrix $\mathbf{M}$.

More specifically, in case the Zernike polynomials are taken as modal variables, the first element of $\mathbf{u_{modal}}$ refers to piston control, the fourth element of $\mathbf{u_{modal}}$ to defocus, etc. See also Figure 3.2. Note that a superposition of unit modal control signals does not necessarily result in a mirror deformation that is exactly the superposition of modes: actuator and surface stiffness effects will limit the actual deformation. Therefore, the deformation is calculated with eq. 6.13 for a PDM, which relates mirror deflections to a PDM control signal. Note that in reality, non-linear effects play a role. For example, hysteresis and a changing thermal environment. These effects are not taken into account at this moment, as they are considered negligible for the performance of the optimisation algorithm.

Figure 7.1 shows an example of the optimised TNO PDM model under modal control. The red lines indicate the deflection the actuators in case no face sheet is present. However, the bending stiffness of the added face sheet mechanically couples the actuators, such that they influence each other according to the equations in Section 6.1. Together, this creates a balance of forces in each actuator that results in a true deflection on the face sheet.

In the figure, primary (left) and tertiary (right) astigmatism are shown. Both have 1λ RMS true deflection and an OPD introduction of 2λ RMS. However, the zero-load deflection of tertiary astigmatism is several times higher than for primary astigmatism, due to the higher spatial frequency of the surface deflection. This also means the actuator forces increase for a given RMS deformation at higher Zernike orders.
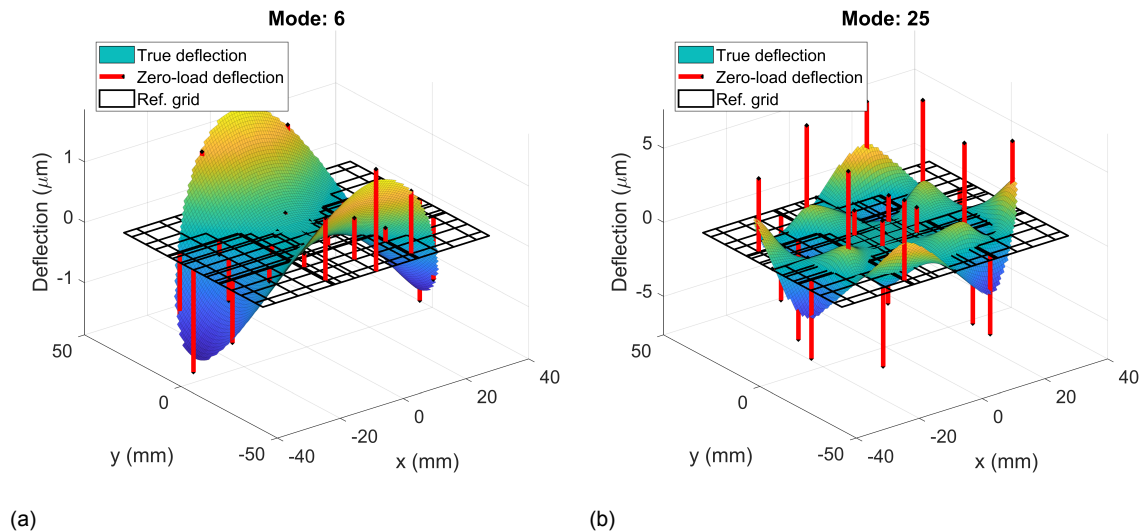

Figure 7.1: Example of modal control on the optimised PDM model in FORTA: required zero-load actuator deflections for modes 6 (left, primary astigmatism) and 25 (right, tertiary astimatism). Both modes cause an RMS OPD of 2λ on the wavefront. It can be seen that the required zero-load actuator displacements are several times higher for the tertiary mode.

7.2. Evaluation of Optimisation Algorithms

This section explains how an algorithm for sharpness optimisation is selected. The goal of this selection process is to achieve the highest rate of convergence to the required diffraction-limited performance. Firstly, note that a general introduction to different algorithms and metrics is presented in Section 5.5.2 and Subsection 5.4.1. Secondly, the flowchart in Figure 7.2 has been created and was followed to determine the successive steps for finding the best applicable algorithm. This flowchart also shows that different mirror models have been tried to evaluate their performance differences in a closed-loop system. See also the results in Section 8.6.
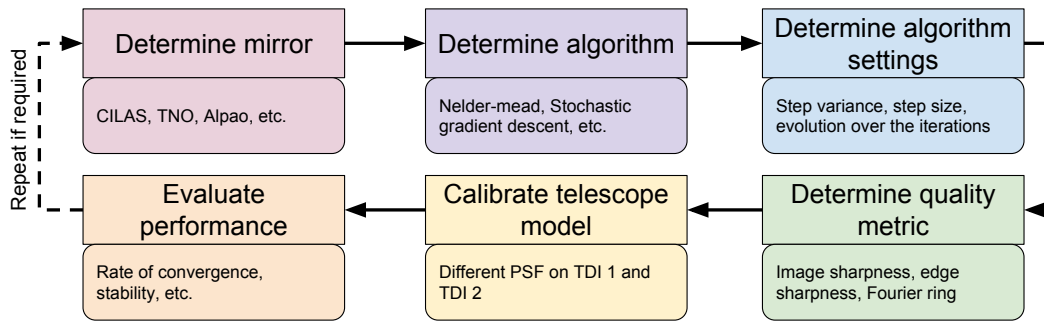
Figure 7.2: Flow diagram showing the steps for determination of the ACS mirror and algorithm in the simulations.

7.2.1. Nelder-Mead simplex

The Nelder-Mead simplex method, first described in 1965 [80], uses a polytope called a *simplex* of $N+1$ points in $N-$dimensional space. The worst performing point in the domain is reflected away along a vertex through the centroid, followed by an expansion or shrinkage along this vertex, depending on the result. If this does not result in a new optimum, the simplex is shrunk.

Advantages of this algorithm are that it is a direct search method, such that no derivatives need to be calculated. This saves time, compared to gradient search methods. Also, the method is robust against image noise. For this reason, it is successfully used for sharpness optimisation in optics [3, 81].

It is shown in Section 8.2 that this algorithm works well for DM control when a static ground scene is considered. However, because the evaluation of points on the simplex is done multiple times on the same scene, this algorithm cannot be used for scanning operations in-orbit.

7.2.2. Steepest descent

The steepest descent method can be used when derivative information is available. Derivatives are estimated by introducing a small change δu to the control variables, one by one. From the difference in sharpness, δf, the gradients are calculated as $\delta f / \delta u$. From the gradients, the direction of steepest decent can be found [63]. By performing a line search along this direction until a minimum is found, large steps towards the optimum can be achieved.

When the optimisation problem has one optimum, this method may be suitable. However, it requires a single scene to work on, in order to find the steepest descent direction. Furthermore, a large number of control variables leads to a large number of function evaluations on each iteration.

Figure 7.3 shows the convergence of the steepest descent algorithm with zonal control on. In this case, all 63 actuator control signals of the CILAS MONO63-85 mirror are the control variables. This means that per iteration, 63 evaluations of the DM are required for gradient determination and ca. 10 to 20 evaluations are required per line search. This results in ca. 3000 changes in the mirror control settings and corresponding calculations of the performance metric. Besides this, the scene has to be static to allow accurate gradient determination. Therefore, this algorithm is not considered applicable for DM optimisation at this point.

It is found that convergence improves when the finite difference step du is set to du_0/i, where i is the iteration number. A relatively large finite difference step is required at the start of the optimisation: the change in the sharpness metric is dominated by noise, so small finite difference steps cause errors in the gradient calculation. At higher sharpness values, the metric becomes more sensitive to changes in the mirror deformation and the step size can decrease. This allows the finite difference steps to stay within the region that contains the optimum control signal values. Ultimately, close to the optimum, the sharpness does not improve significantly any more, such that noise again dominates the gradient determination. See also the sharpness analysis in Section 8.1.

7.3. Proposed Sharpness Optimisation Method

Both the Nelder-Mead simplex method and steepest descent method work on a static scene, and can be applied in the *LowReqs* concept shown in Table 5.4. However ideally, the moving sharpness method introduced in Figure 5.14 should be applied, because it enables the telescope to continue scanning operations during optimisation. This lowers the ADCS requirements and increases the useful
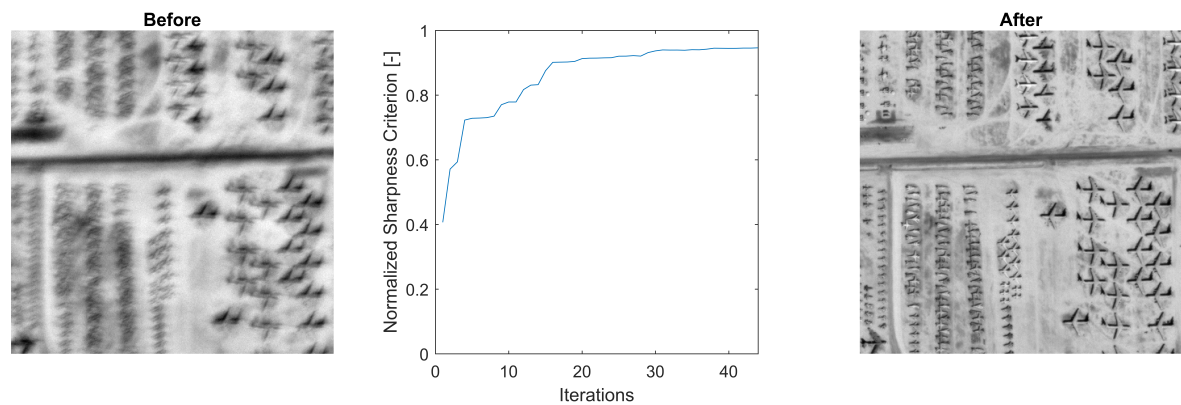
Figure 7.3: Sharpness optimisationwith the steepest descent method for the CILAS MONO63 mirror with zonal control of 63 actuator signals. Numerical determination requires considerable number of function evaluations and may become inaccurate at too small step sizes and with the added noise.

operation time. Each TDI detector can deliver one image of the same ground scene. Therefore, an algorithm needs to be applied that requires a maximum of two sharpness function evaluations.

Vorontsov & Sivokon [82] show that a Stochastic Gradient Descent (SGD) algorithm can be used for wavefront control in an imaging system that registers an incoherent, extended scene. They propose to use the optimisation algorithm to compensate for atmospheric aberrations by introducing parallel perturbations to all control variables of a wavefront corrector, hence the the full name parallel perturbation stochastic gradient descent.

SGD is well-known for its applicability in the automated training of neural networks and other machine learning problems, and variants of the algorithm originate from this field of research. SGD can reach an optimum without explicit numerical determination of the gradient, because it estimates the local gradient stochastically. Therefore, it is computationally efficient, especially on problems that involve a large number of optimisation variables.

Parallel perturbation SGD works as follows. Firstly, a sharpness function evaluation is performed on the first image. Secondly, the DM is perturbed with a random control signal and the sharpness function is evaluated a second time on a new image of the same scene. The change in sharpness then serves as a scaling factor for the actual step size in the direction of the random perturbation. For example, a large sharpness improvement results in a large step in the random perturbation direction, while a small sharpness deterioration results in a small step in the opposite direction of the random perturbation.

A major advantage of this algorithm for ground-scanning telescopes is that it requires only two function evaluations per iteration step, regardless of the number of control variables. This makes it possible to use the algorithm without staring. Both detectors are placed at slightly different optical fields along the direction of orbital motion. This ensures that there is time between acquisition of the first and second image to perturb the DM. For a given scene, the relative change in sharpness is then used to determine the step size of the stochastic step. See Figure 7.4 for an overview of this proposed method. In this overview, a pessimistic DM control bandwidth of 100 Hz is assumed, which is a factor five below the real maximum bandwidth [79]. Integration of the image on one TDI takes 0.02 s, based on image dimensions and the orbital speed. Finally, a sharpness evaluation time of 0.09 s is applied, based on MATLAB experiments. Together, this results in a control loop duration of max. 0.14 s per iteration.

Since all sharpness metrics are dependent on scene content, no absolute metric for image quality can be registered during the process. However, the relative sharpness change provides information on the "quality" of the perturbation step.
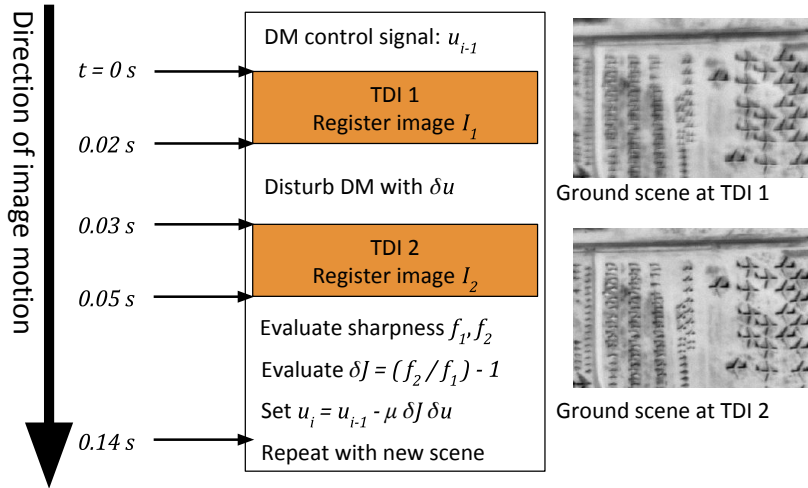
Figure 7.4: Illustration of stochastic gradient descent concept on the time delay integration detectors of the DST. The relative sharpness change is denoted with δJ and the learning rate with μ. One loop is expected to take 0.14 s, based on tests of sharpness evaluation on a simulated image and with a DM change that takes 0.002 s. Based on hardware performance, this duration may change.

7.4. Simulation of the ACS with Stochastic Gradient Descent

To simulate the telescope performance, a ray trace through the optical system is performed with a 64×64 grid of rays for each detector subfield in FORTA. This yields different PSF estimates for the different detectors and subfields. Subsequently, with theory from Section 3.3, the images on each detector are simulated.

7.4.1. Selection of simulated deformable mirrors

For the Aberration Correction System on the DST, two types of deformable mirrors are considered: a monomorph type DM (MDM) and a push-pull actuator type DM (PDM). These are treated in more detail in Chapter 6.

Monomorph DM

the first mirror selected for simulation is a monomorph type DM (MDM). The ray trace model is based on measured influence functions of the CILAS MONO85-60 DM. This mirror has 85 electrode actuators on a 60 mm diameter pupil that control the local curvature of the mirror, i.e. the second derivative of the sag. To encompass the entire pupil of the DST, the model is scaled to have a 70 mm diameter. The advantage of this type of mirror for the DST project is that the technology is currently being space qualified by CILAS [79] and that the mirror has a low mass. See also Table 6.4. The MDM actuator layout is shown in Figure 6.13. Actuator inputs are defined as a normalised electrode voltage of -1 to 1, and influence functions are added linearly with this input. See also Chapter 6 for details on this model.

Push-pull actuator DM

A second series of simulations is performed with a geometry-optimised face plate DM with push-pull actuators (PDM), see Table 6.2. The aim of this model is to simulate a DM currently under development at TNO for use in space instrumentation [30]. The PDM deformation is described by validated analytical plate deformation equations, as explained in Chapter 6. The input signals are zero load deflections of the actuator.

7.4.2. Modelling of uncertainties

To ensure the images are simulated in a realistic manner, noise is added to the images and jitter is taken into account. The modelled noise consists of Poisson shot noise and Gaussian noise. The shot noise on each pixel is drawn from a normal distribution with zero mean and a standard deviation of $\sqrt{Signal}$. The Gaussian noise is set such that the image signal-to-noise ratio is 100. Jitter in the instrument can

cause a relative shift between the images registered on both detectors. To model this effect, an image shift between two detectors is simulated by applying a random tilt to the wavefront of TDI 2. For both focal plane dimensions, this results in a static shift of 1 pixel and an additional random shift with a Gaussian distribution and a standard deviation of 1 pixel. This subpixel shift is modelled by applying a wavefront tilt to the simulated OPD for TDI 2. The angle of tilt determines the PSF shift on the detector. Finally, convolution of the PSF with the pixel size function and the image results in a shifted image on TDI 2.

7.4.3. Implementation of parallel perturbation stochastic gradient descent

The parallel perturbation stochastic gradient descent update step is written as

$$\mathbf{u}_{i+1} = \mathbf{u}_i - \mu \delta J_i \delta \mathbf{u}_i \qquad (7.2)$$

where $\mathbf{u}_i$ is the control signal vector at iteration i, constant μ is the step size or learning rate and δJ is the change in image quality due to a control perturbation $\delta \mathbf{u}$ with variance σ. Due to the stochastic generation of perturbation steps, the product $\delta J_i \delta \mathbf{u}_i$ allows approximation of the function gradient up to $O(\sigma^2)$ [82]. The novelty of the implementation presented here is that a moving scene is used and no absolute sharpness metric is determined in orbit. Instead, the stochastic gradient is estimated by taking the relative fractional change in image sharpness on the two detectors:

$$\delta J = \frac{f_{d2}}{f_{d1}} - 1 \qquad (7.3)$$

Where f_{dk} denotes image sharpness for detector k. The simulated parallel perturbation SGD algorithm in FORTA is explained with the chart in Figure 7.6 and the following pseudocode:

```
1    algorithm Parallel Perturbation SGD is:
2    input: iteration limit i_max, orbital position x_0,
3    scene retrieval function q(x), orbital velocity v,
4    iteration duration δt, pupil P(m,n), initial control vector u_0,
5    detector field locations d_1 and d_2, exit pupil phase function w(u, d),
6    sharpness function s(g), perturbation variance σ, learning rate μ
7
8    output: optimal control vector u, simulated main detector image g_1
9
10   for i = 1 : i_max
11
12          o = q(x_{i-1}) % Get scene data at current location
13
14          for k = 1 : 2 % On both detectors
15                  if k == 1
16                          φ(m,n) = w(u_{i-1}, d_k) % Phase in exit pupil with DM control
17                  elseif k == 2
18                          δu = randn(σ) % Draw perturbations from normal distribution
19                          φ(m,n) = w(u_{i-1} + δu, d_k) % Phase in exit pupil with disturbed DM
20                  end if
21
22                  H(m,n) = P(m,n)e^{-jφ(m,n)} % Amplitude Transfer Function (ATF)
23                  h = F{H(m,n)} % Coherent Point Spread Function (PSF)
24                  f_k = s(o ∗ |h^2|) % Sharpness of simulated image
25          end for
26
27          δJ = f_2/f_1 - 1 % Calculate the relative sharpness change
28          u_i = u_{i-1} - μδJδu % Update the control setting via SGD method
29          x_i = x_{i-1} + vδt % Update orbital position
30   end for
31
32   return u_{i_max}, g_1
```

It is proposed to apply the SGD algorithm with three types of parameter settings during the mission, according to the sequence shown in Figure 7.6. Firstly, after in-orbit deployment, coarse calibration is performed to achieve a wavefront in which the major Zernike aberrations are removed. This algorithm can make relatively large steps with a reduced number of modal control variables. Secondly, fine calibration is performed with different settings to remove the smaller high-frequency wavefront aberrations.

The algorithm needs to make small steps here and may need a different sharpness metric. Also, zonal control variables can be used to achieve local correction. Finally, drifts can be compensated with the SGD algorithm during nominal operations. Depending on the severity of the drifts and the drift rate, different settings may be applied here. Smaller steps reduce the deterioration of image quality due to the perturbations that are introduced, while larger steps may increase the responsiveness at high drift rates.
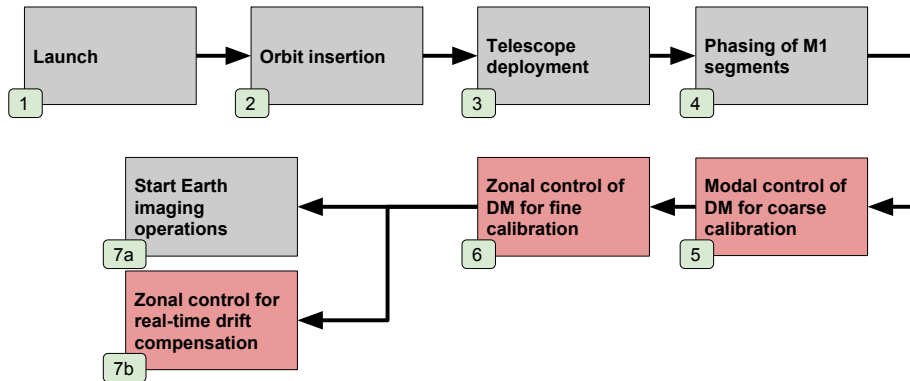

Figure 7.5: Proposed sequence of operations for launch, deployment, phasing of the segmented primary mirror, deformable mirror control and drift compensation during imaging. The coarse and fine calibration blocks are shown in detail in Figure 7.6.
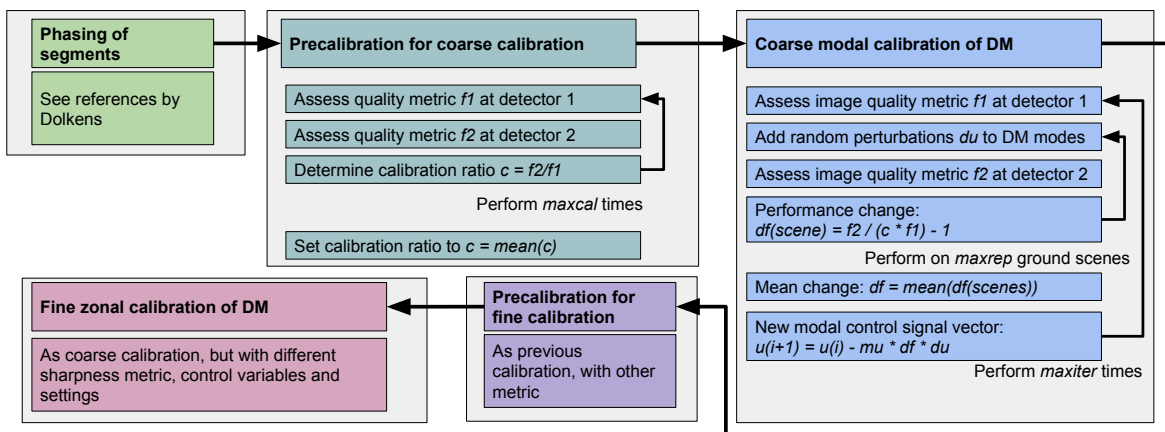

Figure 7.6: Graphical overview of the implementation of parallel stochastic gradient descent control on a dual-detector system for the DST.

7.4.4. Options of the SGD algorithm

The SGD algorithm can be tuned to the optimisation problem with different options. In FORTA, the options that are used during the simulation experiments Table 7.1. These options and their rationale are treated here.

Optimisation variable

For DM control, either modal or zonal commands can be used. See Section 7.1. Modal control uses a set of modes as the control variables. By using modal variables, low-order aberrations with large amplitudes can be removed quickly. The number of variables is determined by the user and can range from 1 (e.g. defocus only) to the highest order terms that the DM can reasonably achieve. For coarse calibration in this experiment, calibrated Zernike modes 4 to 36 (heptafoil) are used, as this is the expected number of terms required for achieving diffraction-limited quality. See Section 4.2. These modes are defined on a Zernike unit circle that just encompasses the cross-shaped exit pupil.

However, to compensate for independent local deformations during fine calibration, zonal control is preferred. In the fine calibration experiment, every actuator is commanded independently. Hence,

Table 7.1: Options implemented for the SGD algorithm in FORTA

Option	Coarse calibration	Fine calibration
Optim. variable	Zernike terms 4 to 36	Actuator input signals
Precalibration steps	50 images	50 images
Step repetitions	3	2
No. of iterations	1000	1500
Sharpness Metric	Power 2	*Fourier ring* or *edge sharpness*
Scaling of μ	Automatic, see text	Automatic, see text
Perturbation std. dev. σ	0.063λ RMS OPD for term 4	50 nm zero-load deflection
σ^2 scaling per variable	See Figure 7.7 and eq. 7.4	None, all actuators the same
σ^2 scaling per iteration	See Figure 7.7 and eq. 7.5	See Figure 7.7 and eq. 7.5

the number of control variables equals the number of actuators on the DM. This type of control is also applied during drift compensation experiments, as shown in the mission flow chart in Figure 7.5.

Precalibration

To quantify the static sharpness difference due to the different detector field locations, a specified number of noisy and shifted images from different scenes are simulated on the central field of TDI 1 and TDI 2. The simulated DM remains in its initial state. The sharpness metric is calculated for both images and the mean ratio between the sharpness metrics is set as the calibration value c. This factor is used to remove a possible sharpness bias during the sharpness optimisation procedure.

Step repetitions

Noise affects the sharpness measurements, especially in low-signal images. Additionally, image shift can cause bright scene content to move into or out of the field of view. This affects the sharpness metrics that depend on a summation of the pixel intensities. In extreme cases, these effects can lead to large optimisation steps in the wrong direction. By repeating the perturbation $\delta\mathbf{u}$ for two or three different scenes and taking the mean sharpness change, this uncertainty is reduced. However, the time required for DM calibration scales linearly with the number of repetitions.

In practice, hysteresis and repeatability of the mirror control signal will also affect the choice for this setting. These effects are not modelled in FORTA.

No. of iterations

Since the moving scene sharpness does not provide an absolute measure for convergence, a maximum number of iterations is used to terminate the algorithm. It has been found empirically that 1000 iterations and 1500 iterations are satisfactory for coarse calibration and fine calibration respectively, given the tolerances from Table 4.1. In general, the number of iterations should scale with the number of optimisation terms and the maximum expected optical path difference.

With the chosen iteration limit, five out of 100 Monte-Carlo trials were identified that did not converge to a Strehl ratio of at least 0.6, due to their large initial aberrations. Visual inspection of the simulated image is sufficient to identify these outliers. A single restart of the algorithm on all these cases is sufficient to achieve a Strehl ratio of at least 0.6. In reality, such extreme tolerances can also be found from the acquired imagery. If necessary, the algorithm parameters can then be updated to increase the step size.

Sharpness metric and measurement

The sharpness metrics were treated in Subsection 5.4.1. With the results that will be shown in the analysis in Section 8.1, it is decided to use the *power 2* metric for coarse calibration. The reasons for this are that it has a relatively steep gradient on a wide domain, but is less sensitive to noise and jitter than the *power 1.5* metric. For fine calibration, the *Fourier ring* metric is selected in the Monte-Carlo experiments shown in Section 8.6, although it has been found in a later stage of the research that the *edge sharpness* metric is more suitable in most cases. See also the conclusion in Chapter 9.

In FORTA, an orbit is simulated and ground scenes with a size of 640×640 pixels are retrieved using the Google Maps API. A scene will only be used for sharpness evaluation when the simulated image

contrast is above a certain threshold, to avoid a sharpness change detection that is dominated by noise. In practice, this setting has been modified to ignore bodies of water and certain desert regions during sharpness optimisation. To avoid artefacts from the Fourier transform and convolution steps in FORTA, the simulated image is padded, convolved with the PSF and subsequently cropped to 540×540 pixels. By taking into account the simulated detector pixel size with respect to the sampled PSF, the simulated image ultimately consists of 180×180 pixels.

Perturbation step generation

The perturbation control vector $\delta \mathbf{u}$ consists of values drawn from a normal distribution with variance vector $\boldsymbol{\sigma}^2$, which may contain a different value for each control variable at each iteration. For modal control, the variance is scaled for each Zernike mode with a factor k_{term}. Scaling follows a logarithmic function that has been matched to the expected initial aberration distribution in the exit pupil of the telescope, see eq. 7.4 and Figure 7.7 (left). As such, it provides the highest expected convergence rate [82]. For zonal control, no relative scaling of actuator perturbation variances is applied.

To allow large steps at the start of the SGD algorithm and smaller steps to the optimum near the end, the variance is scaled as a logarithmic function of the iteration number. This factor, k_i, is given in eq. 7.5 and Figure 7.7 (right).

$$k_{term} = 1 - \frac{\log(term - 3)}{4} \tag{7.4}$$

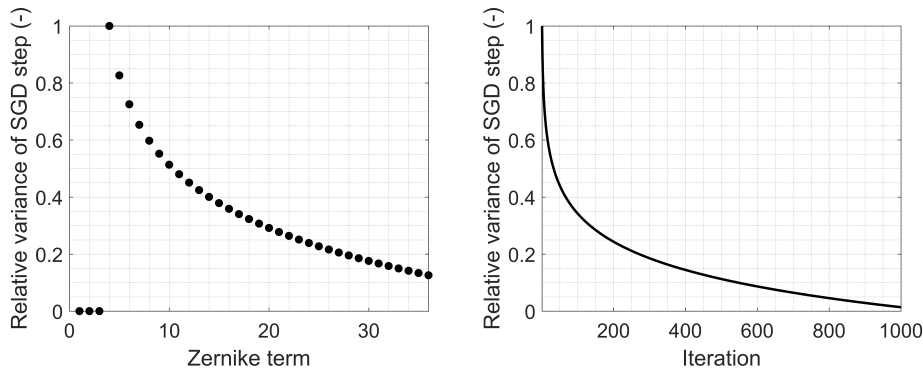$$k_i = 1 - \frac{\log(i)}{\log(1.1 \cdot i_{max})} \tag{7.5}$$

Figure 7.7: The initial SGD variances shown in Table 7.1 are scaled per modal term and per iteration. Left: scaling of relative variance for each Zernike term during modal optimisation. Zernike terms 1, 2, and 3 refer to piston, tip and tilt of the wavefront. They do not change the image quality and are therefore given a step size of zero. Right: scaling of each perturbation variance as function of iteration number (in case the no. of iterations is set to 1000).

Learning rate μ

As is common in machine learning, the step size scaling factor μ is called the learning rate. This factor determines how "aggressively" the algorithm responds to sharpness changes. For example, a relative sharpness increase of $\delta J = 0.1$ and a learning rate $\mu = -6$ result in a step of $\Delta \mathbf{u} = -\mu \cdot \delta J \cdot \delta \mathbf{u} = 0.6 \cdot \delta \mathbf{u}$, or 60% of the random perturbation step.

For the experiment presented here, it is found empirically that the learning rate ideally causes a perturbation step scaling, $-\mu \delta J$, in the range of 5% to 50% of the $\delta \mathbf{u}$. This means that the ideal learning rate depends on the expected quality change δJ, which in turn depends on the sensitivity of the sharpness metric to the aberration severity at that point in the optimisation.

Hence, to avoid manually modifying each sharpness metric in all ranges of operation, an automatic learning rate update rule has been found to be very effective. During each iteration, this update rule increases the learning rate by 10% when a step size would otherwise be below 5% of the perturbation. The step size is decreased by 25% when a step would otherwise be more than 50% of the perturbation. This ensures the rate of convergence is not too low but the response to a perturbation is also never too aggressive.

8
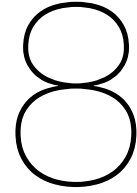
Results of ACS Calibration and Drift Control Simulations

This chapter shows the results and analysis obtained from simulation of the aberration correction system of the DST in FORTA. Firstly, the practical applicability of different sharpness metric is analysed. Secondly, a case study of the Nelder-Mead simplex algorithm for sharpness optimisation by scene-staring is shown. Thirdly, case studies of application of the parallel perturbation SGD algorithm are provided, for both a staring and a moving telescope. Finally, Monte-Carlo simulations are presented that show the performance of SGD on a scanning telescope, considering different DMs, sensitivities of the simulation and algorithm settings.

8.1. Analysis of Sharpness Metrics

To find the behaviour of the sharpness metrics, FORTA is used to simulate the introduction of an astigmatism aberration in the exit pupil. The severity of this aberration is expressed as the root mean square (RMS) OPD value over the exit pupil.

Behaviour of sharpness metrics

In the first experiment, the sharpness metrics discussed in Subsection 5.4.1 are analysed on a single scene, simulated on detector 1.

The three power metrics are given by eq. 5.1. For all of them, a normal weight of $w_n = 1$ is chosen, together with powers $\sigma = 1.5$, $\sigma = 2$ and $\sigma = 4$. These power metrics are expected to each offer optimal performance at a different type of image content, according to Fienup and Miller [45]. They state that lower powers work better on scenes with low-frequency content, whereas higher powers work better on scenes with distinct features. These metrics are referred to as *power 1.5, power 2* and *power 4*, respectively. The *edge sharpness* metric is defined in eq. 5.2 and the *Fourier ring* metric in eq. 5.3. The lower bound and upper bound of the Fourier ring are set to 60% and 80% of the maximum frequency, respectively: in this domain, it is found that the magnitude of the spectrum shows the steepest increase, when typical ground scenes and aberrations are considered. See also Figure 8.2(b) and (c).

The relative sharpness is plotted as a function of DST aberration severity in Figure 8.1. A maximum severity of 3λ RMS OPD is chosen, as this is the maximum expected aberration level in the exit pupil. This level takes into account phasing of the M1 segments and the tolerances from Table 4.1. See also the budget analysis results shown in Figure 4.6.

It can be seen that the *power 1.5* and *power 2* metrics are relatively steep over the entire domain, while power 4, edge sharpness and Fourier ring are more responsive at lower aberration amplitudes. What is the "best" metric for the ACS depends on the optimisation stage, scene and optical system. In early optimisation stages, it is desired to bring the DM close to an optimum shape in a small number of iterations. In later stages of the optimisation, the "best" metric is the one that can bring the DM shape as close as possible to the global optimum.
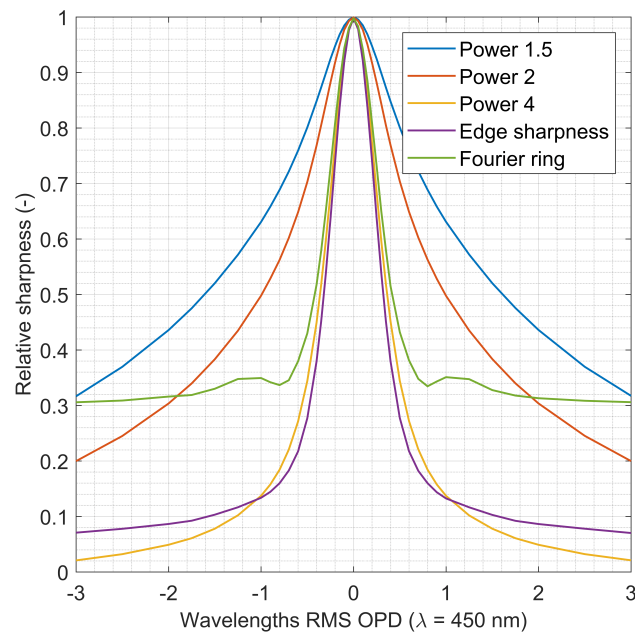
Figure 8.1: Relative sharpness on the static scene shown in Figure 8.2, for five different metrics as a function of aberration severity. The x-axis shows the RMS OPD of introduced astigmatism (Zernike mode 5). The y-axis shows relative sharpness for the different metrics.
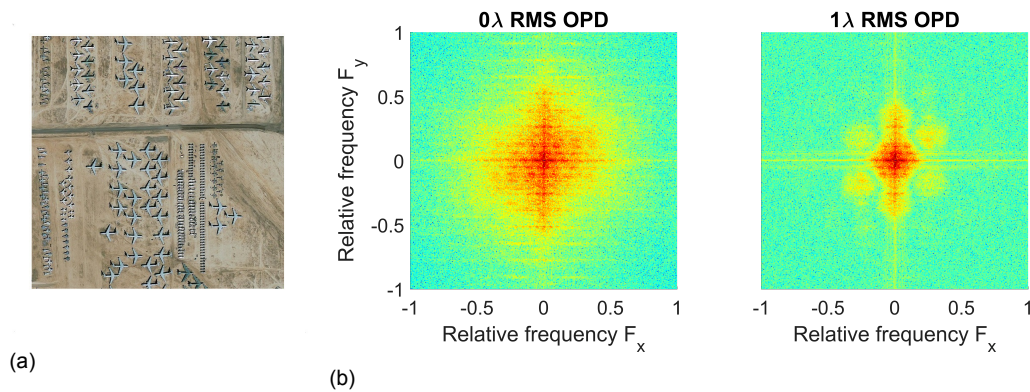

(a)

(b)

Figure 8.2: (a) The image that is used in FORTA to evaluate the *Fourier ring* metric. (b, left) 10-log of the magnitude of the Fourier transform of the image when no aberrations are present. (b, right) 10-log of the magnitude of the Fourier transform of the image, when the DM adds astigmatism with 1λ RMS OPD. It can be seen that Fourier content in the frequency band of $F_L = 0.6 \cdot F_{max}$ to $F_u = 0.8 \cdot F_{max}$ is reduced.

Sensitivity of sharpness metric to aberration reduction

The practical applicability of the sharpness metric also depends on the uncertainties in the sharpness change, which arise from noise and image shift, see Subsection 7.4.2.

Therefore, in the second sharpness experiment, the relative standard deviation (SD) of the sharpness changes is found, given an aberration reduction. The lower this SD, the higher the accuracy of the sharpness metric. Hence, a low SD means less iterations or step repetitions are required for the SGD algorithm to converge.

The experiment is performed as follows. Firstly, the sharpness of an image is calculated on detector 1. After this, the aberration magnitude is halved from e.g. 2λ to 1λ RMS OPD. Subsequently, the sharpness is calculated at detector 2. Finally, the sharpness change is determined according to eq. 7.3. This process is repeated for 300 Monte-Carlo trials per scene to find the probability distribution of the relative metric change.

The scenes and experimental results are shown in Figure 8.3. All scenes measure an equal ground area. Scene A (prairie land) has low overall contrast, but relatively many details from shrubs and their shadows. Scene B (roads, trees and a lake) has high contrast on all spatial frequencies., while scene C (agricultural crops) has low overall contrast, but contains many edges. The bar plots in Figure 7 indicate the SD in the measured sharpness change for a 50% aberration reduction, starting at 2λ (left) 1λ (middle) and 0.2λ (right) RMS OPD of astigmatism.
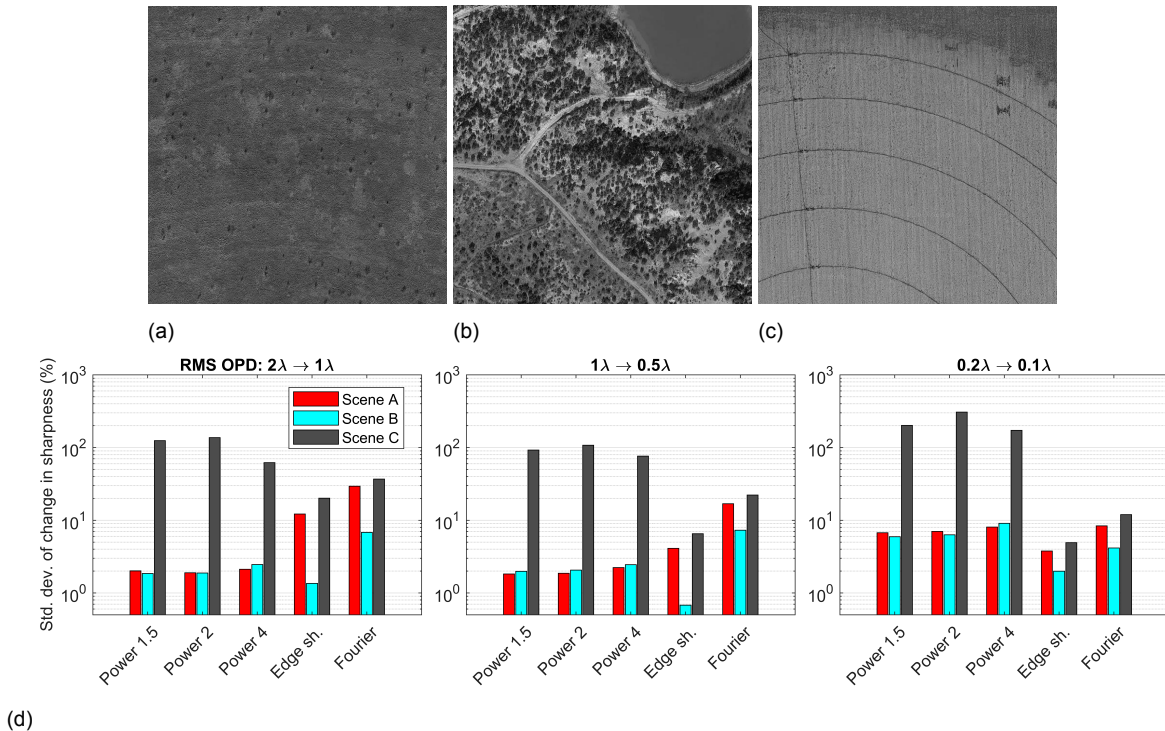

Figure 8.3: Standard deviation of the sharpness change for three different scenes, different sharpness metrics and different OPD reduction steps. The effect of the OPD reduction is simulated in 300 Monte-Carlo trials per case. Noise and jitter are taken into account. It can be seen that the relative and absolute accuracy of the metric depends on the selected scene and aberration magnitude.

In the results, it can be seen that scene C has a higher SD than scenes A and B, with all metrics and for all aberration severities. In cases where the SD is higher than 100%, this scene is practically useless for stochastic gradient determination. Furthermore, for scenes B and C, the edge sharpness metric has the lowest SD of all metrics, for all three aberration levels: its maximum SD is below 21%, its minimum SD is 0.7% and occurs for scene B at a reduction from 1λ to 0.5λ RMS OPD. On the other hand, for scene A, the power 1.5 and power 2 metrics perform best at an aberration level of 2λ and 1λ RMS OPD.

The Fourier ring metric shows a relatively high SD for all scenes at 2λ and 1λ RMS OPD, but this improves at 0.2λ RMS OPD. On the other hand, the SD of all power metrics increases at an aberration level of 0.2λ RMS OPD, even reaching 300% for scene C. Hence, fine calibration should not use power metrics.

A final note is that the sharpness change becomes practically undetectable below an aberration level of ca. 0.05λ RMS OPD, depending on the scene. At this level, image noise and shift drive the measured sharpness change. However, the target Strehl ratio of 0.08 requires an RMS OPD of 0.07λ, see MIS-REQ-07 in Section 4.4. Therefore, this requirement can in principle be achieved with the accuracy of these sharpness metrics.

Table 8.1 provides an overview of the findings of this sharpness metric analysis, which can be used for the selection of a metric.

Table 8.1: Properties of sharpness metrics. The calibration factor is the mean of the relative differences between the metric at detector 2 and detector 1. It indicates the sensitivity of the metric w.r.t. the optical field. The variance column shows the variance of the relative differences between the metric at the two detectors. A higher variance indicates a higher sensitivity to image noise and image shift and makes the metric less reliable in detecting image quality improvement in the DST.

Metric	Findings
Edge sharpness	Least sensitive to shift and noise, scene-dependent, strong gradient near optimum.
Power 1.5	Smooth over large domain, not as accurate as *power 2*.
Power 2	Medium sensitivity to shift and noise. Smooth over entire domain.
Power 4	Performance comparable to *power 1.5*. Steep in central part of the domain, but sensitive to noise and jitter there.
Fourier ring	Ring taken from 60% to 80% of Nyquist frequency. Local maxima found at ± 1 wavelength RMS OPD. Relatively flat over domain used during coarse calibration, but steep and relatively accurate on fine calibration domain. Requires on-board Fourier transform operations.

8.2. Optimisation with Nelder-Mead Simplex

As a reference for comparison of the parallel perturbation SGD algorithm, the DM is controlled via sharpness optimisation on a single scene, by using the Nelder-Mead simplex algorithm [80] applied to the image on only detector 1, assuming this detector is not scanning. This approach has been demonstrated to work in experimental setups [81] and has been used before by Dolkens for DM optimisation in the DST [3].

In this FORTA simulation experiment, the geometry-optimised 37-actuator PDM is controlled in a single calibration procedure. Zonal control is applied. This leads to a 38-point polytope for simplex optimisation. The initial actuator zero-load deflection commands required for polytope generation are $1 \, \mu m$. The power 2 sharpness metric is used. Noise is added to every image, but no relative image shifts are applied. In total, 800 optimisation iterations are performed, requiring 1100 DM control changes and sharpness evaluations.

Figure 8.4 shows the convergence of the Nelder-Mead simplex algorithm for DM control, on a typical case of initial exit pupil aberrations. The results are shown for the central field of detector 1.

The plot shows that the Strehl ratio increases to 0.97, while the RMS OPD decreases from 0.71λ to 0.03λ RMS OPD. The "spiky" behaviour of the Strehl ratio and OPD are a result from the Nelder-Mead simplex iterations, which sometimes cause a function evaluation at a point that is worse than the current optimum.
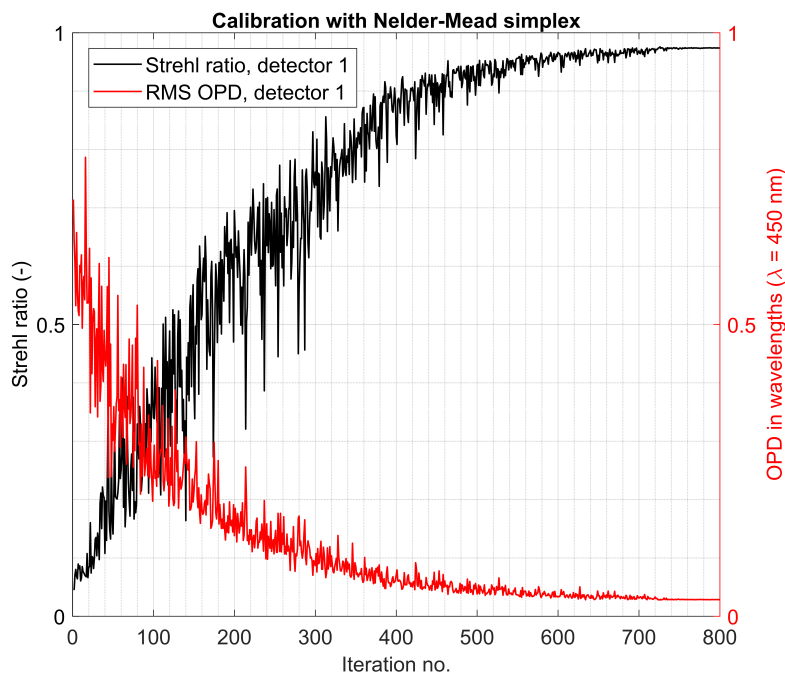

Figure 8.4: Sharpness optimisation with the Nelder-Mead simplex algorithm for PDM control, applied to a static scene. The 800 iterations shown require ca. 1100 sharpness function evaluations.

8.3. Application of SGD to a Single Scene on One Detector

The results in Figure 8.5 show the optical performance change during coarse and fine calibration with the parallel perturbation SGD algorithm, as applied to the images of a single scene on a starin detector 1 only. This case study is performed on the same case as the one used in the Nelder-Mead simplex optimisation.

To simulate the images, noise is added, but no relative image shifts are applied. Coarse calibration uses modal control variables and the *power 2* sharpness metric, while fine calibration uses zonal control variables and the *edge sharpness* metric.

With this experiment, it is demonstrated that the SGD algorithm can converge to values comparable to the Nelder-Mead simplex algorithm: a Strehl ratio of 0.97 is achieved again. However, this value is

reached after 2500 iterations (i. e. 5000 sharpness evaluations) instead of the 800 iterations (1100 sharpness evaluations) used for the Nelder-Mead simplex algorithm.
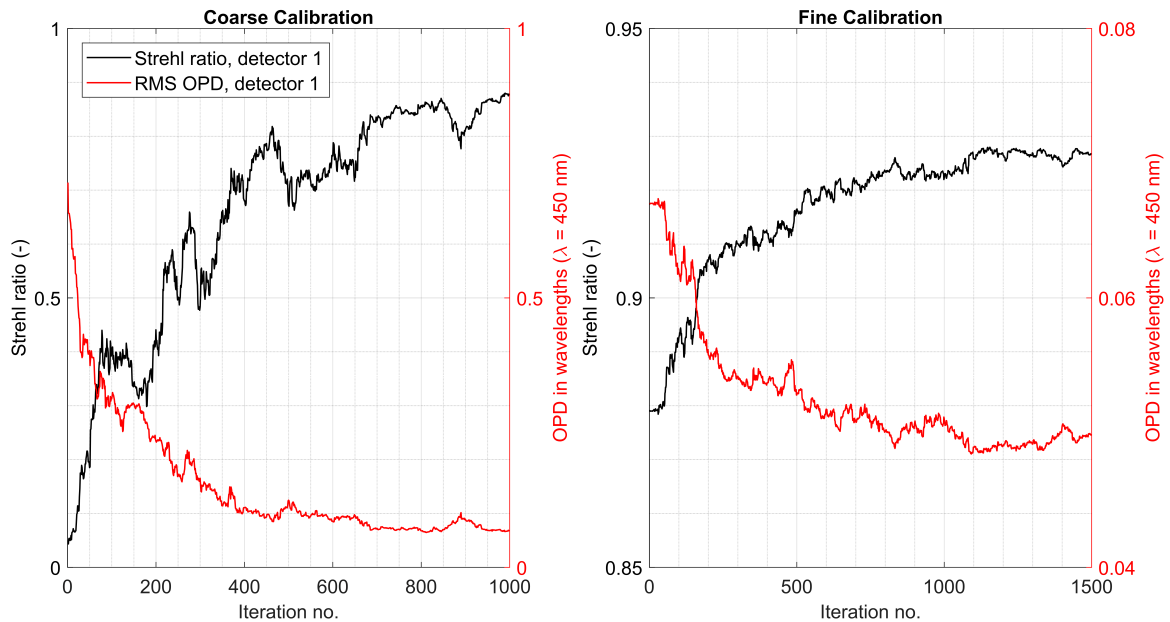

Figure 8.5: Application of the parallel perturbation SGD algorithm for PDM control with a static scene and a single detector. Coarse calibration with modal control and *power 2* metric (left) and fine calibration with zonal control and edge sharpness metric (right). Every iteration requires two sharpness evaluations on detector 1.

8.4. Application of SGD to Moving Scenes on Two Detectors

The actual performance of the metrics in the parallel perturbation SGD algorithm depends on the wide range of scenes that the telescope observes during orbit. With FORTA and Google Maps API integration, a wide range of scenes along the orbit path is used. For nominal simulations, imagery from a longitude of $-100°$ above North America is used, while a second set of imagery from a longitude of $+6.6°$ is used to verify results from the nominal image data. See Figure 8.6 for a graphical overview.
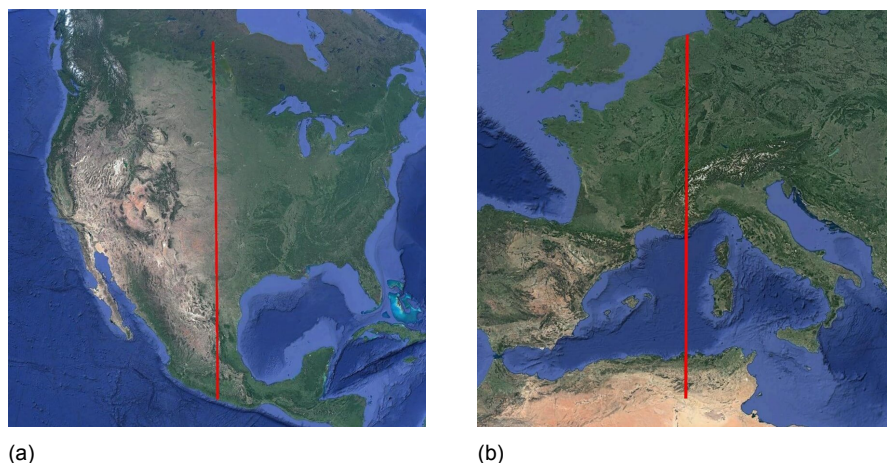

Figure 8.6: The track of satellite imagery used for generating the moving scene. Left: test set. Right: validation set. Images ©Google

It is found empirically that the *power 2* metric shows the best convergence behaviour at coarse calibration with modal variables (which works for an RMS OPD of 3λ to ca. 0.1λ). Although edge sharpness was expected to work well in this range too, it is found that certain DM perturbations cause

a PSF with increased local brightness maxima. This causes artefacts of scene edges, thus falsely increasing the measured edge sharpness and slowing down the convergence rate. See the example in Figure 8.7. This issue does not occur during fine calibration, as the PSF is not disturbed as much and contains one sharp maximum at the central region already.
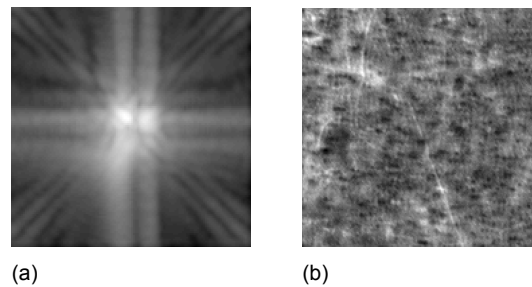

(a)   (b)

Figure 8.7: Simulated PSF (a) and a simulated image (b) when the edge sharpness metric encounters a local optimum during coarse calibration. Multiple local maxima in the PSF cause edge artefacts in the image, thereby falsely increasing the measured sharpness. The power metrics do not suffer from this type of problem, since they do not depend on the brightness difference between pixels.

Figure 8.8 shows the results of the moving scene SGD experiment, for the same case as the two experiments treated above. Coarse calibration brings the Strehl ratio on the central field of detector 1 to 0.80, while fine calibration increases this to 0.92 before levelling out around iteration 800. The RMS OPD is reduced from 0.7λ to 0.05λ.

Figure 8.9 shows the exit pupil OPD before calibration, after coarse calibration and after fine calibration of the DM. It shows that the peak-to-valley OPD is reduced from more than 3λ to less than 0.6λ after coarse calibration, and less than 0.5λ after fine calibration.
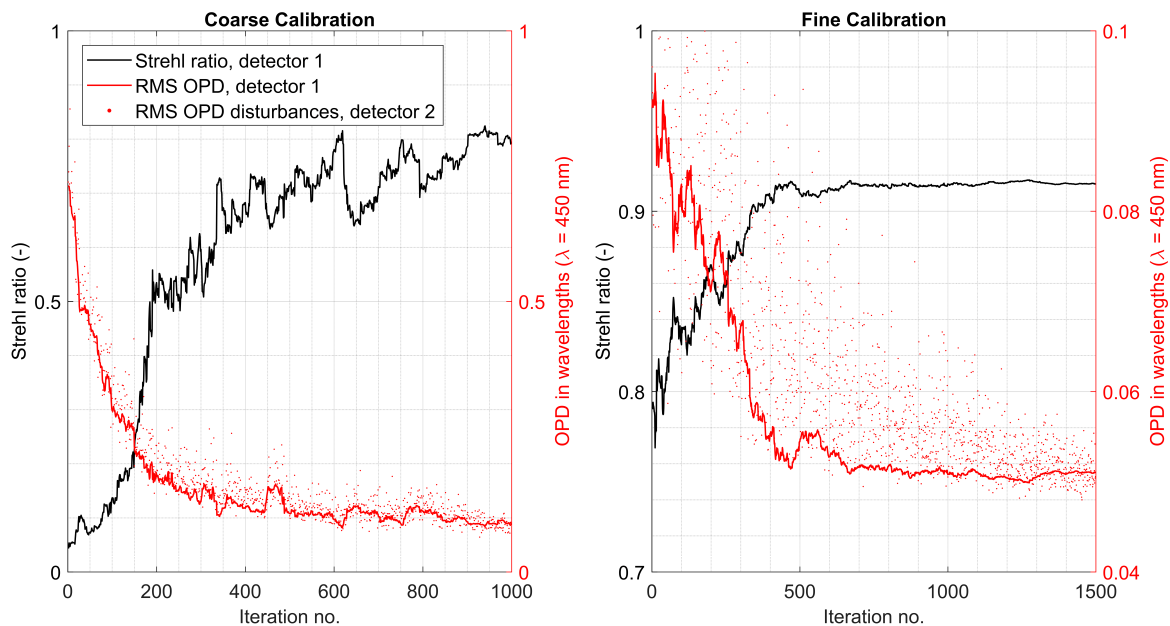

Figure 8.8: Simulated Strehl ratio and OPD with PDM calibration via the stochastic gradient descent algorithm. Coarse calibration with modal control and the power 2 metric (left) and fine calibration with zonal control and the Fourier ring metric (right). Dots indicate the OPD values on detector 2 when the mirror is disturbed to determine stochastic gradients. The decreasing variance of the steps ensure "spiky" behaviour decreases towards the end of the optimisation. Every iteration requires one sharpness evaluation on detector 1 and one evaluation on detector 2.

To compare the performance of the controller with that of the analytical best-fit of the mirror, figure 8.10 shows the OPD and relative actuator control signals for four cases. Both the optimised PDM (top row) and CILAS 85-70 MDM (bottom row) are considered. On the left, the OPD and control signals
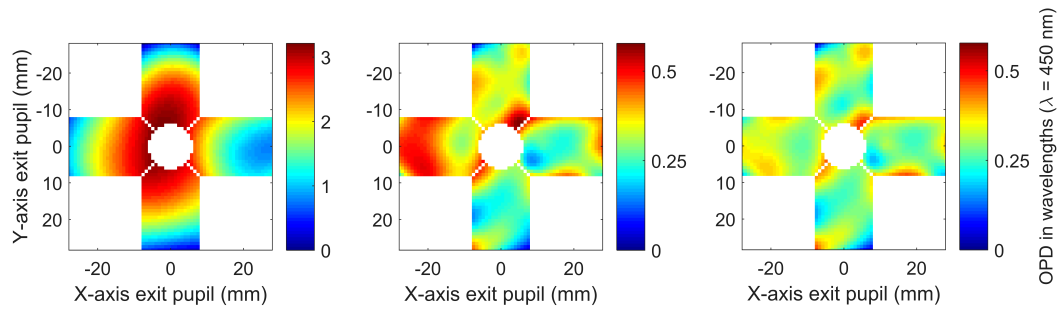
Figure 8.9: Exit pupil optical path difference for the case shown in Figure 12 after primary mirror segment phasing (left), after PDM modal control (middle) and after PDM zonal control (right).

after an analytical least-squares DM fit are repeated (these are also shown in Figure 6.16). On the right, the result after fine calibration is shown. The least-squares fit has been calculated with the theory in Chapter 6.

It can be seen that there are some differences between the least-squares fit and the control output. Interestingly, the top-right part of the top pupil segment shows the highest PV OPD in both the MDM and PDM control case. However, the rest of the wavefront is relatively flat. Especially for the PDM, the wavefront variation over the pupil is equally low for the fit and the control output.

Regarding the MDM, it can be seen that the actuators outside the pupil receive the highest signals in case of the ideal fit. However, the SGD control method does not show this difference. The most likely cause for this is the fact that the stochastic perturbations at off-pupil actuators have a very small effects on the sharpness, such that their effect cannot be accurately estimated by the SGD algorithm. To still allow the outermost actuators to receive an optimum control signal, their perturbation variance could be increased in future implementations of the algorithm.
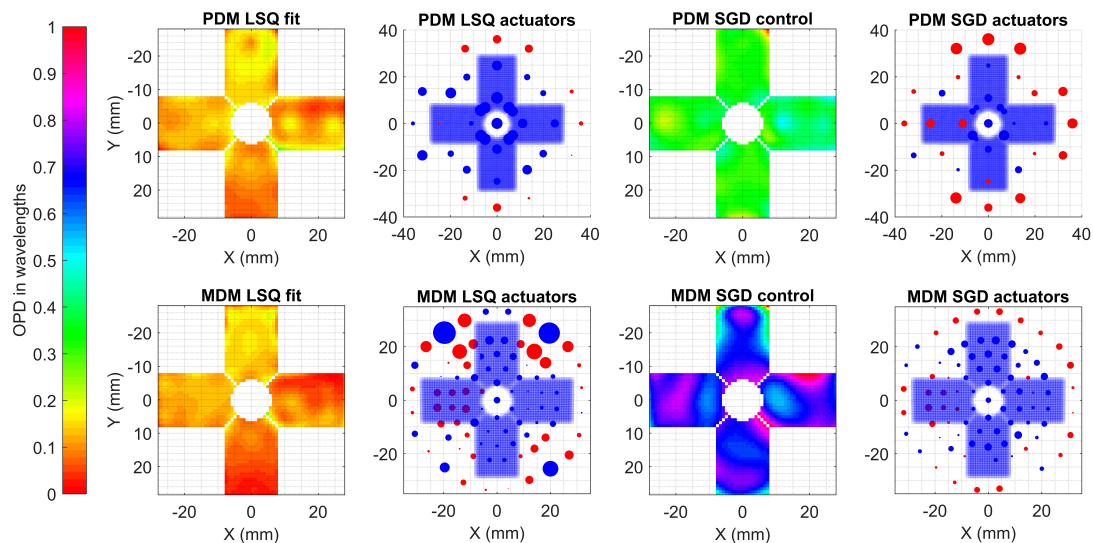
Figure 8.10: Det. 1 central field OPD and actuator control signals for the analytical LSQ solution and moving-scene SGD output after fine calibration. Red markers indicate a positive control signal, blue markers a negative control signal. The size of the markers indicates the magnitude of the signal. Note that the MDM actuator signals outside the pupil are much higher in the least-squares fit than for the SGD output.

FORTA Live Simulation Dashboard

To follow the behaviour of the moving scene SGD algorithm in FORTA throughout an orbit, a dashboard function has been written. This function displays the current PSF and OPD of the central field of the primary detector, the satellite location and the corresponding simulated image that is used for sharpness change measurement.

Figure 8.11 shows two frames of an animation created with this function. In the first image, the satellite is above North-Eastern Europe and moving in a southward polar orbit. In the final image, the satellite is near the equator in Africa. The coarse calibration of the DM has finished by this time. This can be seen by the increase in Strehl ratio, the decrease in RMS OPD and the increased intensity at the centre of the PSF. Also, the simulated image is visually of higher quality.

(a)

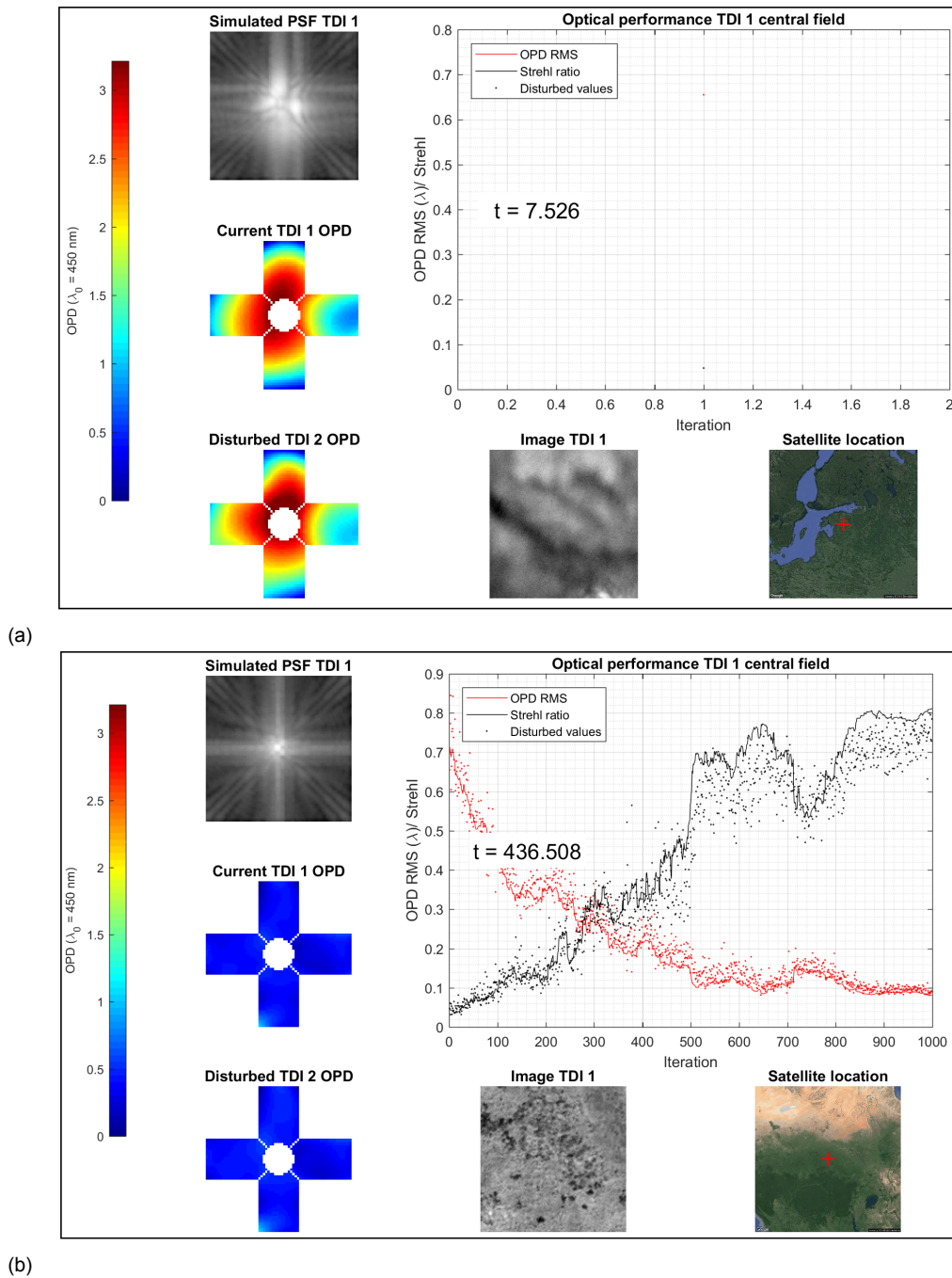(b)

Figure 8.11: Snapshot of the animated PSGD dashboard in FORTA. Figure (a): start of coarse modal DM calibration with SGD. (b): end of coarse modal calibration with SGD at iteration 1000. The timestamp denotes active algorithm time. The actual flight time is higher than the timestamp diplays, because the algorithm skips low-contrast areas such as the Sahara desert and the Mediterranean Sea.

8.5. Application of SGD for Drift Compensation

A drift compensation case study is performed on the output of the calibrated system shown in the previous subsection. The experiment simulates an introduction of stochastic tolerance drifts over a period of 300 seconds. See the results in Figure 8.12 (left). Without active drift compensation, the Strehl ratio goes down from 0.92 to 0.42, while the RMS OPD increases from 0.05λ to 0.31λ. When the SGD algorithm is switched on, the drifts are actively compensated, see Figure 8.12 (right). This time, the Strehl ratio decrease is limited to a final value of 0.78 and the RMS OPD does not increase to above 0.12λ. The exit pupil OPD for this case is shown in Figure 8.13. Without drift compensation, the peak-to-valley OPD increases from 0.4λ to 1.5λ. With drift compensation, this error is constrained to 0.8λ.
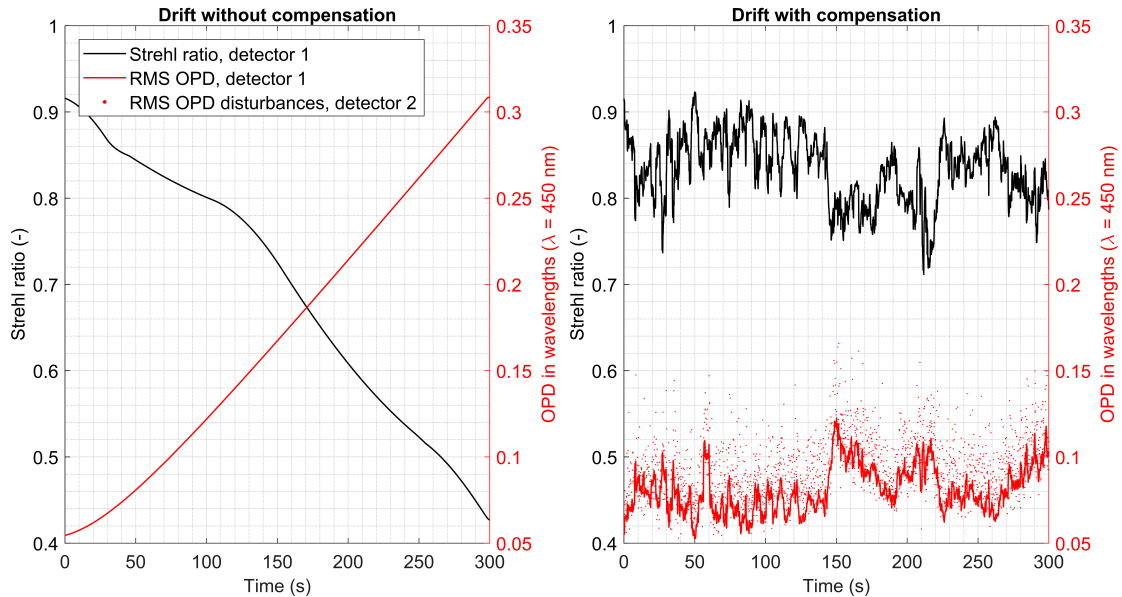

Figure 8.12: Optical performance on the central field of detector 1 when drifts are introduced during a period of 300 seconds. Without SGD drift compensation (left) and with SGD drift compensation (right).
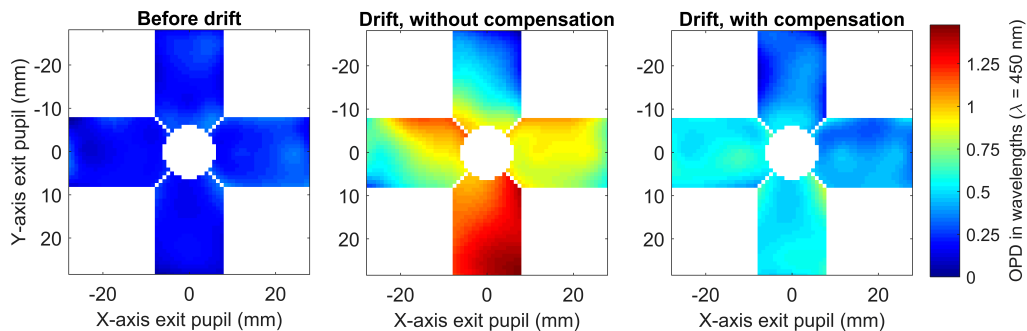
Figure 8.13: Exit pupil optical path difference for the case shown in Figure 8.12. Left: after fine calibration, before drifts. Middle: after tolerance drift, without SGD compensation. Right: after tolerance drift, with SGD compensation.

When the drift-compensation algorithm is on, zonal control is applied with a fixed perturbation variance for all actuators, with a value of 30% of the initial variance for fine calibration. When the DM has been calibrated, these small perturbations cause a step in the RMS OPD of ca. 0.02λ, and a Strehl ratio change of ca. 0.01. These numbers are so low that the human eye cannot observe the effects of drift control perturbations on the acquired images. Nevertheless, these perturbations result in a measurable sharpness change, such that drift compensation can be used throughout the nominal scanning operations.

8.6. Monte-Carlo Simulations of Control with Two Detectors

To find the effects of different SGD algorithm settings, it is not sufficient to test these changes on one typical aberration profile. Instead, a Monte-Carlo simulation is performed on 100 optical systems, on which the two-sigma tolerances from Table 4.1 are applied. Firstly, the M1 segment phasing algorithm from Dolkens is applied to remove piston, tip, and tilt errors from the entrance pupil. Subsequently, the parallel perturbation SGD algorithm is applied on the dataset of moving scenes, visualised in Figure 8.6. At the time of the experiment, the M1 phasing algorithm was still under development. Hence, it caused 13 outliers in the exit pupil OPD, which are ignored in the Monte-Carlo results. Three types of Monte-Carlo experiments are performed: firstly, a sensitivity analysis of the algorithm settings during coarse and fine calibration, secondly, a comparison study between calibration with the PDM and MDM and thirdly, a study for the application of SGD to compensate for drifts that occur during the orbit. After application of SGD, a Weibull distribution is fitted to the cumulative distribution function of the Strehl ratios on detector 1. In all experiments, this fit has an R-squared value of at least 0.97, indicating a good fit.

Monte-Carlo experiment 1: Sensitivity analysis

To find the effects of simulation and algorithm settings, a sensitivity analysis is performed. In this analysis, the nominal settings are those shown in Table 7.1. The *Fourier ring* metric is used for zonal control, because at the time of this experiment, the advantages of *edge sharpness* had not yet been investigated. The MDM model is used, as this monomorph mirror offers faster ray trace calculations than the PDM model, while the number of actuators is higher.

The effects of three parameter changes are shown in Figure 8.14. In the first case, noise is removed from all simulated images. In the second case, image shift is removed from the simulated images. In the third case, the no. of iterations of the algorithm is doubled.
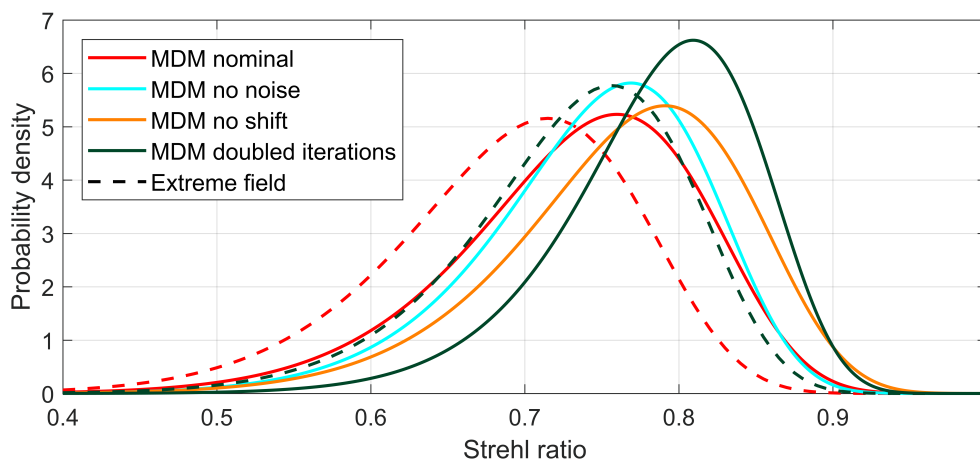

Figure 8.14: Monte-Carlo results of the sensitivity analysis. Solid lines indicate the Strehl ratio on the central field of detector 1 after fine calibration, while dashed lines show the Strehl ratio on the extreme field (across the orbital track) of this detector.

It can be seen that the effect of doubling the no. of iterations is largest, followed by the removal of image shift and the removal of noise. Also, as expected, the extreme field shows lower optical performance due to field-dependent aberrations. The following four Monte-Carlo cases did not produce a significant change with respect to the nominal case and are therefore not shown in these results:

1. To remove static optical quality bias, the two detectors are placed closer together in the along-track field of the telescope.

2. To avoid dependency on the scene content, the dataset of scenes is changed from a strip across North America to a strip across Europe, see Figure 10.

3. To avoid dependency on the order of pseudo-random steps, different random seeds are used to initialise the SGD algorithm.

4. To remove possible scaling effects in the pupil, the simulated MDM is scaled back from $70\ mm$ pupil diameter to the original value of $60\ mm$.

Monte-Carlo experiment 2: PDM and MDM comparison
A comparison between the performance of the PDM and MDM models is show in Figure 17. Besides comparing the nominal cases for both mirrors, a case is added where the PDM uses the edge sharpness metric for fine calibration, instead of the nominal Fourier ring metric, to verify the finding from Subsection 4.1 that this metric should deliver convergence to higher Strehl ratios.
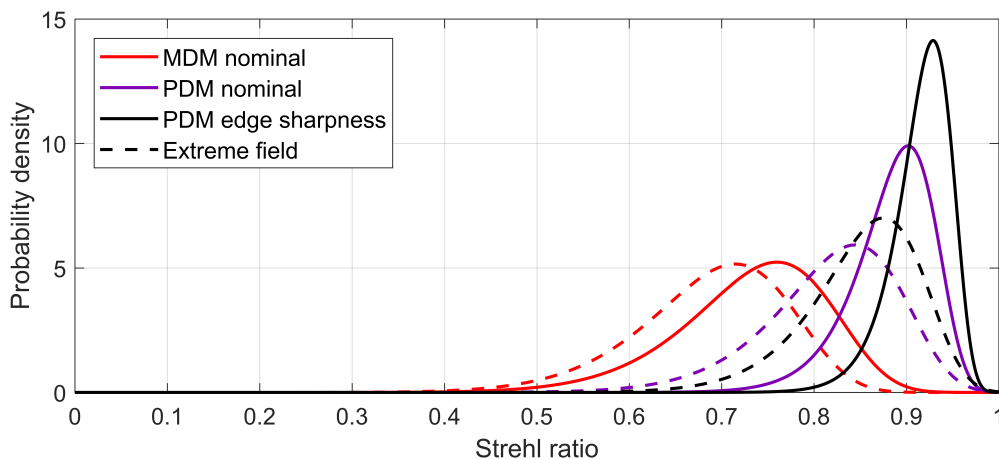

Figure 8.15: Monte-Carlo results of the MDM and PDM comparison. Solid lines indicate the Strehl ratio on the central field of detector 1, while dashed lines show the Strehl ratio on the extreme field (across the orbital track) of this detector.

Clearly, the PDM offers improved optical performance with respect to the MDM, although the number of actuators is 37 instead of 85. This difference arises due to two effects. Firstly, the PDM actuator positions are optimised for the exit pupil of the DST. Secondly, the MDM technology causes a curvature change that affects the sag on the entire mirror surface, such that there is a strong coupling between the deformations caused by actuators. The actuator coupling on the PDM is much less strong. This effect makes the stochastic gradient estimate less accurate for the MDM than for the PDM. Also, as expected from the results in Section 8.1, the use of the edge sharpness metric for fine calibration of the PDM offers the highest performance, with an expected Strehl ratio above 0.9 on the central field of detector 1 and an expected Strehl ratio above 0.8 on the extreme field.

Monte-Carlo experiment 3: drift compensation with SGD
In orbit, the telescope will suffer from thermo-mechanical drifts that decrease the optical performance. The current two-sigma budgets are shown in Table 1. Ideally, the SGD algorithm is used after calibration to continuously compensate for these drifts. The results in Figure 18 illustrate that this is indeed possible. In this experiment, the tolerances of a calibrated system are changed linearly during a period of 600 seconds, towards a new, drifted state. During this time, the SGD algorithm can be switched off (the "no control" case in the figure) and on (the "control" case in the figure). In both cases, the stability budgets are applied as well, to simulate the effects of uncompensated high-frequency jitter on the image.

The results show that SGD drift compensation avoids a dramatic decrease in optical performance. Without control, the expected Strehl ratio decreases to below 0.5 for both mirror designs. With drift compensation control, the performance still decreases, but the Strehl ratio on the central field remains above 0.6 for the MDM, and above 0.7 for the PDM for most cases. The reason that full drift compensation is not possible, is that the drifts in M1 segments cause discontinuities in the wavefront at the exit pupil. These discontinuities cannot be removed with the current DM design. Even if this were possible, the severity of optical field-dependent aberrations would still increase.
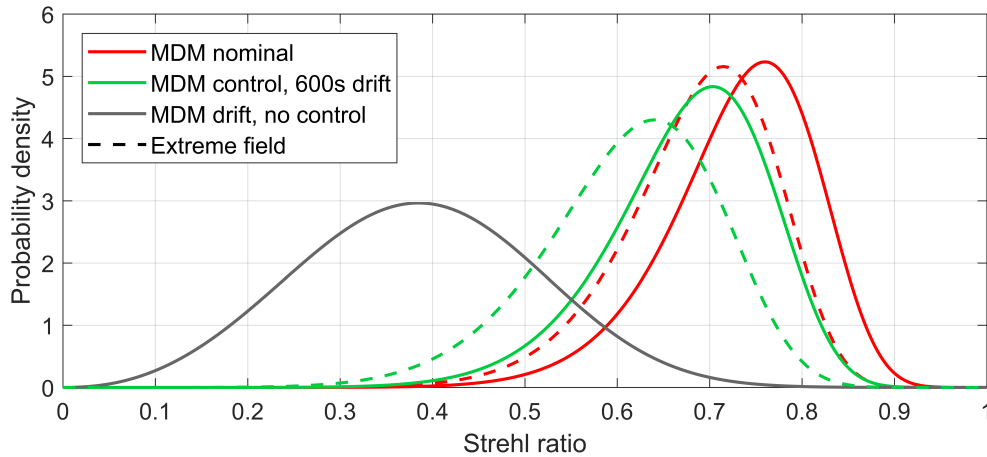
Figure 8.16: Monte-Carlo results of the SGD performance for drift compensation, in case the drifts are added during a 600 s period. On top of the drifts, stability budgets are taken into account. Solid lines indicate the Strehl ratio on the central field of detector 1, while dashed lines show the Strehl ratio on the extreme field (across the orbital track) of this detector.

8.7. Addition of Phase Diversity

As stated in Subsection 5.4.2 and Section 5.7, the use of a Phase Diversity (PD) algorithm is proposed for different DST concepts. With PD, two detector images are sufficient to reconstruct a most likely wavefront map. With this map, the DM could be controlled directly.

Hence, to improve the convergence rate of mirror control, PD experiments are done. In FORTA, TDI detector 2 is placed out of focus by 0.1 mm and the image on detectors 1 and 2 is simulated. The SGD algorithm and the MATLAB `fminunc` functions are used to minimise the PD error metric, assuming a wavefront consisting of the Zernike terms up to the fifth order, and constraints on the weights of 1λ RMS OPD per Zernike term.

In rare occasions, removal of the estimated aberration does increase the performance. However, often local minima are found far from the optimum and the optical performance only deteriorates with this PD implementation. Further research into the application of Phase Diversity is outside the scope of this thesis work, since the majority of the time has been spent on sharpness optimisation using SGD. Therefore, no further experiments were performed to improve the performance of the PD algorithm.

9

Conclusions and Recommendations on ACS Design

With the design features and results that are presented in the previous chapters, a detailed ACS design has been established. This chapter presents this design in the first section and the corresponding scientific conclusions in the second section. Finally, in the third section, recommendations for future research are done.

9.1. Final Design

This section presents the final architecture and design choices of the ACS. Figure 9.1 shows the remaining options from the five Design Option Trees that have been presented in Chapter 5. All other options have been discarded for the current ACS design.

The final design is mostly based on the *LowReqs* concept, which can be found in the morphological overview. See Table 5.4. Two changes are done to the original concept to increase the ACS performance. These are shown in morphological table 9.1. The first change is that both modal and zonal control variables are used, so that rapid coarse calibration and precise fine calibration can be achieved.

The second change is the application of parallel perturbation SGD on the output of two TDI detectors. This control algorithm enables the DST to continue scanning operations while optimising the image sharpness. Therefore, nominal operations need not be interrupted. Hence, the name of this final concept is *SharpScan*. To compare the new concept to the original trade-off in Table 5.5, the *Sharp-Scan* score is presented in Table 9.2. Note that this concept obtains the highest trade-off score of all concepts, because it delivers a high optical performance and compensated for drifts during scanning operations. Furthermore, the concept has a low mass, a low power consumption, introduces a low risk and a low cost of development. This is because only minor changes are required with respect to existing technologies implemented in the design. So, the final system design can be summarised as follows:

> The Aberration Correction System on the Deployable Space Telescope corrects the optical path difference in the exit pupil of the system with a DM. This is either a customised mirror with push-pull actuators on a facesheet, e.g. from TNO, or a customised monomorph mirror, e.g. from CILAS. The control system has three modes of operation: coarse calibration, fine calibration, and drift control. All three modes use a parallel perturbation SGD algorithm for image sharpness optimisation with the DM. The algorithm requires the output of two scanning TDI detectors placed in the focal plane, such that two images of the same ground scene can be acquired to evaluate the effect of a DM perturbation. The SGD control algorithm can be used without degradation of the nominal imagery during scanning. Therefore, the algorithm can be used to calibrate the DM and correct for optical tolerance drifts. For coarse calibration, the optimisation metric is the sum of the squared pixel intensities, while for fine calibration and drift compensation, an edge sharpness metric is used.
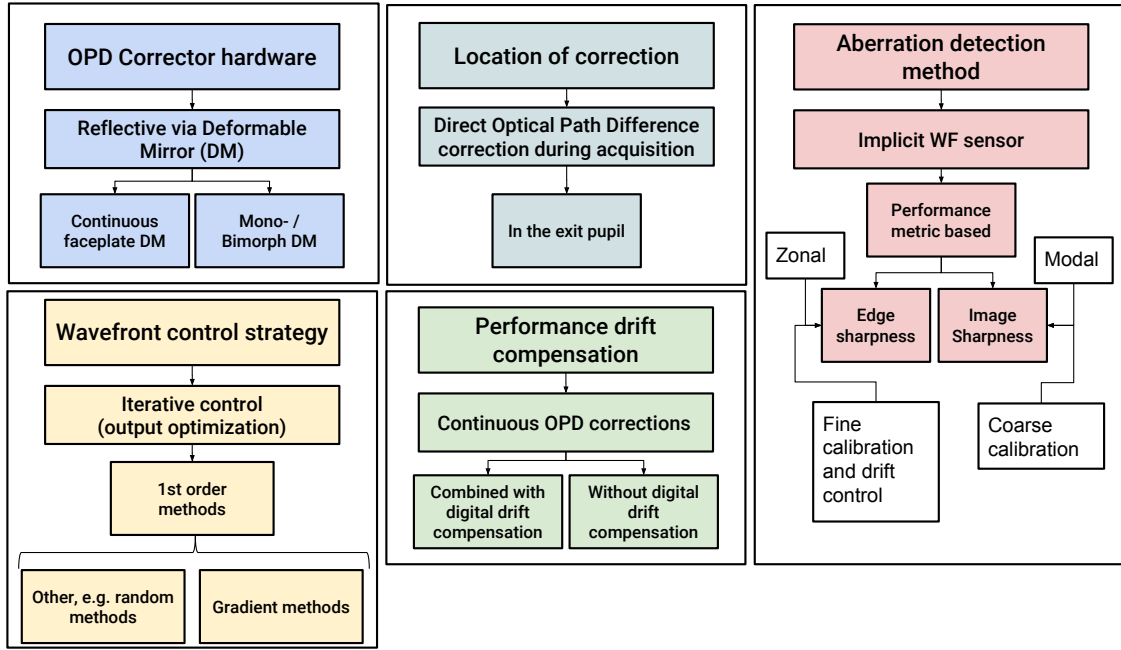
Figure 9.1: Design Option Tree options that are proposed for the final system design. Two options are still open for the DM type.

Table 9.1: The final proposed *SharpScan* ACS concept, an improved version of the original *LowReqs* concept that uses continuous drift compensation and a combination of modal and zonal control.

Element	*SharpScan*	*Element*	*SharpScan*
WF Corrector	Def. Mirror	Control strategy	Optimize metric
Location of correction	Exit pupil	Control variables	Modal + Zonal
Location of PD^2 drift compensation	None	Aberration detection	Performance Metric
Duty cycle	Continuous		

Table 9.2: Trade-off score for final *SharpScan* concept, as addition to the trade-off in Table 5.5. This concept performs best, compared to the original concepts.

Misalignment compensation	Drift compensation	Total mass	On-board power	Cost	Risk	Scanning interruption
+	+ +	+	+ +	+	0	+ +

9.2. Conclusions

This section presents the conclusions and findings from this thesis research. Firstly, it is checked whether the ACS system requirements, presented in Table 4.2 in Chapter 4, can be met by the current system design. After this, general conclusions are considered.

9.2.1. Achievement of goals and system requirements

In Chapter 2, six subgoals for this thesis are stated to support the design of the ACS. Five of these subgoals have been achieved. The tasks related to subgoal 5 have not been carried out, due to the limited time available for breadboard research. However, detailed simulations in FORTA have still enabled the design of a new and promising system.

Most importantly, the main mission requirement MIS-REQ-07, has partly been achieved. This requirement states that a Strehl ratio of 0.8 shall be achieved over the entire telescope FOV under all circumstances. As such, it drives the need for an ACS. The central field of the primary detector indeed achieves a Strehl ratio above 0.8 in all simulated cases, when the PDM and edge sharpness optimisation are simulated. However, it has been shown by Figures 6.15 and 8.15 that the value of 0.8 is not always reached on the extreme field of the primary detector. This indicates that the difference in quality over the FOV is mainly caused by field-dependent aberrations, which are unavoidable with the current DST design and tolerances. However, as also stated in the recommendations, a weighted sharpness optimisation may be investigated for partly removing the effects of field-dependent aberrations. It is expected that this will lead to a slightly lower Strehl ratio on the central field, but at the gain of a higher average Strehl ratio over the detector. See also Table 6.3.

Requirement ACS-OPT-01 states that a Strehl ratio change of 0.05 shall be detected by the ACS. It has indeed been shown that this is possible during active drift compensation in Section 8.5, as changes in the Strehl can be as small as 0.01 and still allow convergence of the control algorithm.

As the system has been designed to detect sharpness changes in Earth imagery, requirement ACS-OPT-02 has been successfully met. Furthermore, this system indeed corrects initial aberration with the severities found in the requirements discovery. Hence, ACS-OPT-03, ACS-OPT-04 and ACS-OPT-05 have been met as well.

ACS-OPT-06 states that drift effects should be compensated. It has been shown in Section 8.6 that this can indeed be achieved, albeit within realistic limits. Discontinuous wavefronts, caused by phasing drifts of the primary mirror segments, cannot be fully flattened in the exit pupil. However, when drift control is extended to the primary mirror segments as well, this requirement may be achieved. MSc student Sean Pepper will look into this part of the design for his thesis research.

Requirement ACS-OPT-07 relates to post-processing. This technique has not been investigated, because of the scope of this thesis. Therefore, it is still to be determined whether this requirement is still applicable. MSc student Dirk Risselada will take this requirement into account during his thesis research.

Regarding the context of the system, ACS-OPT-08 to ACS-ELE-01 in Table 4.2 relate to the system environment, the mission duration mass, volume, and power consumption. During this thesis research, no reasons have been found to not be able to meet these requirements. For example, the TNO PDM prototype requires much less than 1 W to operate [30], so no requirement violations are expected. Also, the current control method does not require more than a small detector and low-power on-board computer to run the algorithm. Furthermore, existing the true drift rates and calibration requirements of the final DST design will determine the actual power consumption.

Regarding space readiness: the MDM technology is being space qualified. However, depending on the practical implementation of the design, different hardware experiments should be executed to validate if these requirements are met. For example, the PDM technology has not been space qualified yet. Therefore, hardware tests should be performed to increase the TRL.

So, an novel ACS design has been presented that is capable of removing aberrations, such that high-resolution images can be made with the Deployable Space Telescope. In general, the system has a minimum impact on the spacecraft mass and volume, but allows for continuous operation during ground scanning operations. This makes it an elegant solution for the next generation of Earth observation telescopes.

9.2.2. General conclusions

The research output presented in this thesis is not only applicable to the DST project, but may also be relevant for other projects in the field of active optics for space telescopes. Therefore, several general conclusions are drawn. A graphical overview of all conclusions is shown in Figure 9.2.
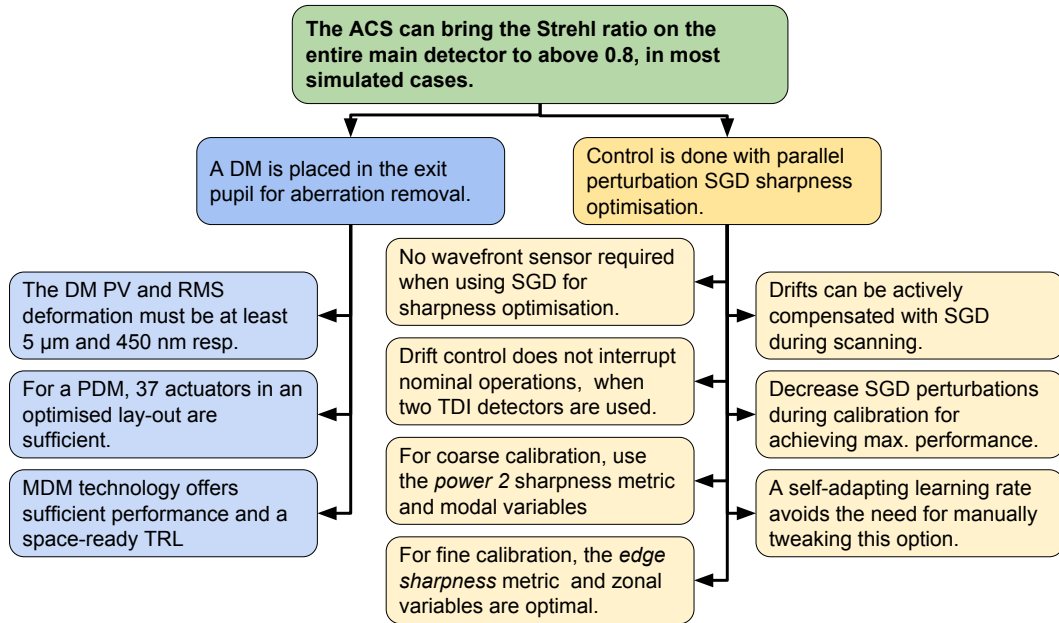
Figure 9.2: The main conclusions of this thesis are summarised in this overview, which is split up into a branch for the DM design and a branch for the sharpness optimisation method. Note that the conclusions regarding the DM only hold for the DST design, while the control branch of conclusions also holds for other space telescopes for Earth observation.

In this thesis, it has been shown that a parallel perturbation stochastic gradient descent algorithm can be used to calibrate different types of deformable mirrors in space telescopes for Earth observation. The algorithm uses the relative sharpness change on images of ground scenes, as acquired on two time-delay and integration detectors that are a small distance apart in the along-track direction of motion. The algorithm has a very low computational cost, only requiring two sharpness function evaluations per iteration and the generation of one random control perturbation.

Besides offering calibration of the mirror, it is also possible to use the parallel perturbation SGD algorithm to actively counter drift effects that are introduced by e.g. thermal variations and material creep. The perturbations have no visual effect on the imagery, such that drift compensation can be used during normal telescope operations. Not only does the use of this system remove the need for a dedicated wavefront sensor, but it also allows the telescope to continue scanning operations without the need for pointing at a single ground scene. Hence, the total system mass and complexity can be reduced and the duration of nominal operations can be increased.

During coarse calibration with SGD, calibrated Zernike polynomials are used as the control variables. The *Power 2* sharpness metric is used in case of the DST. During fine calibration, every actuator is controlled independently as zonal control variable, while the *edge sharpness* metric enables the SGD algorithm to achieve the highest performance. These settings are applied during the active drift compensation.

Noise and relative image motion between the detectors does affect the accuracy and convergence behaviour of the algorithm. Especially random image shifts are found to affect the accuracy of the sharpness change measurements. Depending on the real shifts in the application, it may be required to first digitally align the two images before the sharpness is calculated over a defined area of the detector.

When comparing the MDM and PDM deformable mirrors, the best optical performance is achieved with a PDM with an optimised layout for 37 actuators. However, simulation of an MDM with 85 actuators also shows a performance that may be sufficient for most applications. Most likely, a reduction in the number of actuators will even improve the convergence rate, as less control variables are to be

considered. The MDM technology is currently being space qualified, which makes it more practical to apply in a real space telescope design.

A disadvantage of the use of parallel perturbation SGD is that the wavefront error is not explicitly measured, such that actual aberration statistics need to be achieved by determination of the control signal to the mirror, or by implementing phase diversity techniques. Besides this, relative motion between image acquisition on both detectors can result in inaccuracy in the sharpness change measurement. Future research on this topic can be done when the design of the DST becomes more refined.

9.3. Recommendations for future work

Different suggestions and recommendations for follow-up research are derived from this research. Most importantly, not all steps presented in Figure 5.20 have been carried out, due to time constraints of the work. However, it is still very valuable to develop a breadboard system to validate the outcome of the FORTA simulations.

Furthermore, with the current ACS design, no explicit information is given about the aberration severity in the telescope. However, image restoration and mirror control with phase diversity techniques can provide an estimate for the aberrations, without the need for explicit wavefront sensors in the design. It is therefore recommended to put effort into simulating different phase diversity options in FORTA.

Regarding the sharpness optimisation, an investigation into a weighted combination of sharpness metrics may be used to define a metric that is accurate on different types of scenes, noise, and image shift. For example, a combination between *Power 2* and *Edge sharpness* may be applicable over a larger domain than both metrics independently. This combined metric may even be dependent on the detected image contrast and content, to ensure optimal measurement techniques are selected for the available data.

A comparable recommendation is to remove the bias of the sharpness optimisation w.r.t. the central field of TDI 1. For example, to allow an optimisation of weighted performance on the entire FOV, different sharpness regions can be selected on the detector for the measurement of sharpness change. The weighted average of the change due to an SGD perturbation can then be used for wide-FOV optimisation. Due to time constraints, this has not been implemented in the FORTA simulation yet.

To improve the convergence rate of the sharpness optimisation, other SGD algorithm variations may be tested. For example, momentum methods can be applied, which use information of past SGD iterations to improve the estimate for the global search direction.

Finally, improvements on the DM models for ray tracing can be made when a set of analytical basis functions can be derived for the MDM type mirror. Also, actuator hysteresis and actuator control resolution can be taken into account to achieve a more realistic model for simulation of the ACS.

Bibliography

[1] G. P. Van Marrewijk, "Deployable space telescope: Technology review for AE4020 literature study." unpublished literature review, June 2017.

[2] D. Dolkens, "A deployable telescope for sub-meter resolutions from microsatellite platforms," Master's thesis, Delft University of Technology, February 2015.

[3] D. Dolkens and J. M. Kuiper, "Design and end-to-end modelling of a deployable telescope," in *International Conference on Space Optics*, October 2016.

[4] J. W. Lopes Barreto, "Deployable space telescope: Optimal boom design for high precision deployment of the secondary mirror," Master's thesis, Delft University of Technology, May 2017.

[5] B. T. Van Putten, "Design of the deployment mechanism for the primary mirror elements of a deployable space telescope," Master's thesis, Delft University of Technology, March 2017.

[6] D. Dolkens, "Design and optimization of a deployable telescope for earth observation applications," *Submitted for Publication*.

[7] R. K. Tyson, *Principles of Adaptive Optics*. Academic press, second ed., 1998.

[8] G. Hickey, T. Barbee, M. Ealey, and D. Redding, "Actuated hybrid mirrors for space telescopes," in *Proc. SPIE*, vol. 7731, 2010.

[9] K. L. Cahoy, A. D. Marinan, B. Novak, C. Kerr, T. Nguyen, M. Webber, G. Falkenburg, and A. Barg, "Wavefront control in space with mems deformable mirrors for exoplanet direct imaging," *Journal of Micro/Nanolithography, MEMS, and MOEMS*, vol. 13, no. 1, p. 011105, 2014.

[10] M. Laslandes, E. Hugot, M. Ferrari, C. Hourtoule, C. Singer, C. Devilliers, C. Lopez, and F. Chazallet, "Mirror actively deformed and regulated for applications in space: design and performance," *Optical Engineering*, vol. 52, no. 9, p. 091803, 2013.

[11] K. Patterson and S. Pellegrino, "Ultralightweight deformable mirrors," *Applied optics*, vol. 52, no. 22, pp. 5327–5341, 2013.

[12] R. Paxman and J. Fienup, "Optical misalignment sensing and image reconstruction using phase diversity," *JOSA A*, vol. 5, no. 6, pp. 914–923, 1988.

[13] W. J. Smith, *Modern Optical Engineering*. SPIE Press, McGraw-Hill, third ed., 2000.

[14] R. E. Fisher, B. Tadic-Galeb, and P. R. Yoder, *Optical System Design*. SPIE Press, second ed., 2008.

[15] M. Bass, C. M. DeCusatis, J. M. Enoch, V. Lakshminarayanan, G. Li, C. MacDonald, V. N. Mahajan, and E. Van Stryland, *Handbook of Optics*, vol. 1. McGraw-Hill New York, third ed., 2010.

[16] J. W. Goodman, *Introduction to Fourier Optics*. McGraw-Hill, second ed., 1996.

[17] L. C. Roberts Jr, M. D. Perrin, F. Marchis, A. Sivaramakrishnan, R. B. Makidon, J. C. Christou, B. A. Macintosh, L. A. Poyneer, M. A. van Dam, and M. Troy, "Is that really your Strehl ratio?," in *SPIE Astronomical Telescopes+ Instrumentation*, pp. 504–515, International Society for Optics and Photonics, 2004.

[18] M. Verhaegen, P. Pozzi, O. Soloviev, G. Vdovin, and D. Wilding, *Control for High Resolution Imaging*. Delft University of Technology, 2017. Lecture notes, will be published as book. Retrieved from: `https://blackboard.tudelft.nl/bbcswebdav/pid-2937403-dt-content-rid-10253588_2/xid-10253588_2`.

[19] V. N. Mahajan, "Strehl ratio for primary aberrations in terms of their aberration variance," *JOSA*, vol. 73, no. 6, pp. 860–861, 1983.

[20] D. Korsch, "Closed form solution for three-mirror telescopes, corrected for spherical aberration, coma, astigmatism, and field curvature," *Applied Optics*, vol. 11, no. 12, pp. 2986–2987, 1972.

[21] M. Lampton and M. Sholl, "Comparison of on-axis three-mirror-anastigmat telescopes," in *Optical Engineering+ Applications*, p. 66870S, International Society for Optics and Photonics, 2007.

[22] M. Bass, C. MacDonald, G. Li, C. M. DeCusatis, and V. Mahajan, *Handbook of Optics*, vol. 5. McGraw-Hill New York, third ed., 2010.

[23] S. Manzanera, M. A. Helmbrecht, C. J. Kempf, and A. Roorda, "Mems segmented-based adaptive optics scanning laser ophthalmoscope," *Biomedical optics express*, vol. 2, no. 5, pp. 1204–1217, 2011.

[24] M. Loktev, D. W. De Lima Monteiro, and G. Vdovin, "Comparison study of the performance of piston, thin plate and membrane mirrors for correction of turbulence-induced phase distortions," *Optics Communications*, vol. 192, no. 1, pp. 91–99, 2001.

[25] N. Doble, D. T. Miller, G. Yoon, and D. R. Williams, "Requirements for discrete actuator and segmented wavefront correctors for aberration compensation in two large populations of human eyes," *Applied optics*, vol. 46, no. 20, pp. 4501–4514, 2007.

[26] P. Y. Madec, "Overview of deformable mirror technologies for adaptive optics and astronomy," in *Proc. SPIE*, vol. 8447, p. 844705, 2012.

[27] D. Gallieni, M. Tintori, M. Mantegazza, E. Anaclerio, L. Crimella, M. Acerboni, R. Biasi, G. Angerer, M. Andrigettoni, A. Merler, *et al.*, "Voice-coil technology for the e-elt m4 adaptive unit," in *1st AO4ELT conference-Adaptive Optics for Extremely Large Telescopes*, p. 06002, EDP Sciences, 2010.

[28] R. Hamelinck, "Adaptive deformable mirror: based on electromagnetic actuators," 2010. retrieved from `https://pure.tue.nl/ws/files/2837696/201010440.pdf`.

[29] G. Vdovin and M. Loktev, "Deformable mirror with thermal actuators," *Optics letters*, vol. 27, no. 9, pp. 677–679, 2002.

[30] S. Kuiper, N. Doelman, E. Nieuwkoop, T. Overtoom, T. Russchenberg, M. van Riel, J. Wildschut, M. Baeten, J. Human, H. Spruit, *et al.*, "Electromagnetic deformable mirror development at tno," in *SPIE Astronomical Telescopes+ Instrumentation*, pp. 991204–991204, International Society for Optics and Photonics, 2016.

[31] G. Vdovin, "Current performance limits for micromachined membrane deformable mirrors," in *Proceedings of the Second International Workshop on Adaptive Optics for Industry and Medicine*, pp. 118–122, World Scientific, Singapore, 2000.

[32] G. Vdovin. Oral discussion, 2017.

[33] J. R. Nagel, "Solving the generalized poisson equation using the finite-difference method." `http://www.ece.utah.edu/~ece6340/LECTURES/Feb1/Nagel%202012%20-%20Solving%20the%20Generalized%20Poisson%20Equation%20using%20FDM.pdf`, 2012.

[34] O. Ikeda and T. Sato, "Comparison of deformability between multilayered deformable mirrors with a monomorph or a bimorph actuator," *Applied optics*, vol. 25, no. 24, pp. 4591–4597, 1986.

[35] C. Schwartz, E. Ribak, and S. Lipson, "Bimorph adaptive mirrors and curvature sensing," *JOSA A*, vol. 11, no. 2, pp. 895–902, 1994.

[36] R. Palomo. E-mail correspondence with CILAS, 2017.

[37] P. Rausch, S. Verpoort, and U. Wittrock, "Unimorph deformable mirror for space telescopes: environmental testing," *Optics express*, vol. 24, no. 2, pp. 1528–1542, 2016.

[38] P. Fortescue, G. Swinerd, and J. Stark, *Spacecraft Systems Engineering*. John Wiley & Sons, 2011.

[39] D. Redding. E-mail correspondence, 2017.

[40] K. Patterson and S. Pellegrino, "Shape correction of thin mirrors," in *52nd AIAA Structures, Structural Dynamics and Materials Conference*, 2011.

[41] K. N. LaFortune, "Generalized alvarez lens for correction of laser aberrations," tech. rep., Lawrence Livermore National Laboratory (LLNL), Livermore, CA, 2004.

[42] A. M. Manuel, *Field-dependent aberrations for misaligned reflective optical systems*. The University of Arizona, 2009.

[43] R. G. Paxman, T. J. Schulz, and J. R. Fienup, "Joint estimation of object and aberrations by using phase diversity," *JOSA A*, vol. 9, no. 7, pp. 1072–1085, 1992.

[44] C. Johnston, K. Gribbon, and D. Bailey, "Implementing image processing algorithms on fpgas," in *Proceedings of the Eleventh Electronics New Zealand Conference, ENZCon'04*, pp. 118–123, 2004.

[45] J. Fienup and J. Miller, "Aberration correction by maximizing generalized sharpness metrics," *JOSA A*, vol. 20, no. 4, pp. 609–620, 2003.

[46] R. A. Muller and A. Buffington, "Real-time correction of atmospherically degraded telescope images through image sharpening," *JOSA*, vol. 64, no. 9, pp. 1200–1210, 1974.

[47] R. A. Gonsalves, "Phase retrieval and diversity in adaptive optics," *Optical Engineering*, vol. 21, no. 5, p. 215829, 1982.

[48] L. M. Mugnier, A. Blanc, and J. Idier, "Phase diversity: a technique for wave-front sensing and for diffraction-limited imaging," *Advances in Imaging and Electron Physics*, vol. 141, pp. 1–76, 2006.

[49] D. M. Muñoz, C. H. Llanos, L. d. S. Coelho, and M. Ayala-Rincón, "Comparison between two fpga implementations of the particle swarm optimization algorithm for high-performance embedded applications," in *Bio-Inspired Computing: Theories and Applications (BIC-TA), 2010 IEEE Fifth International Conference on*, pp. 1637–1645, IEEE, 2010.

[50] J. M. Rodríguez-Ramos, E. Magdaleno, D. Domínguez, M. Rodríguez, and J. Marichal, "2d-fft implementation on fpga for wavefront phase recovery from the cafadis camera," in *Proc. SPIE*, vol. 7015, p. 701539, 2008.

[51] J. A. Georges, P. Dorrance, K. Gleichman, J. Jonik, D. Liskow, H. Lapprich, V. Naik, S. Parker, R. Paxman, M. Warmuth, *et al.*, "High-speed closed-loop dual deformable-mirror phase-diversity testbed," in *Optical Engineering+ Applications*, pp. 671105–671105, International Society for Optics and Photonics, 2007.

[52] J. L. Codona, "Differential optical transfer function wavefront sensing," *Optical Engineering*, vol. 52, no. 9, p. 097105, 2013.

[53] L. A. Poyneer, "Scene-based shack-hartmann wave-front sensing: analysis and simulation," *Applied Optics*, vol. 42, no. 29, pp. 5807–5815, 2003.

[54] E. Sidick, J. J. Green, R. M. Morgan, C. M. Ohara, and D. C. Redding, "Adaptive cross-correlation algorithm for extended scene shack-hartmann wavefront sensing," *Optics letters*, vol. 33, no. 3, pp. 213–215, 2008.

[55] L. F. Rodríguez-Ramos, Y. Martín, J. J. Díaz, J. Piqueras, and J. M. Rodríguez-Ramos, "The plenoptic camera as a wavefront sensor for the european solar telescope (est)," in *SPIE Optical Engineering+ Applications*, p. 74390I, International Society for Optics and Photonics, 2009.

[56] J. M. Rodríguez-Ramos, B. F. Castellá, F. P. Nava, and S. Fumero, "Wavefront and distance measurement using the cafadis camera," in *SPIE Astronomical Telescopes+ Instrumentation*, p. 70155Q, International Society for Optics and Photonics, 2008.

[57] H. Song, R. Fraanje, G. Schitter, H. Kroese, G. Vdovin, and M. Verhaegen, "Model-based aberration correction in a closed-loop wavefront-sensor-less adaptive optics system," *Optics express*, vol. 18, no. 23, pp. 24070–24084, 2010.

[58] D. L. Fried, "Least-square fitting a wave-front distortion estimate to an array of phase-difference measurements," *JOSA*, vol. 67, no. 3, pp. 370–375, 1977.

[59] W. H. Southwell, "Wave-front estimation from wave-front slope measurements," *JOSA*, vol. 70, no. 8, pp. 998–1006, 1980.

[60] E. Gendron, "Modal control optimization in an adaptive optics system," in *European Southern Observatory Conference and Workshop Proceedings*, vol. 48, p. 187, 1994.

[61] S. Boyd and L. Vandenberghe, *Convex optimization*. Cambridge university press, 2004.

[62] R. Fletcher and C. M. Reeves, "Function minimization by conjugate gradients," *The computer journal*, vol. 7, no. 2, pp. 149–154, 1964.

[63] F. Roger, "Practical methods of optimization," *Constrained Optimization*, 1987.

[64] A. S. Lewis and M. L. Overton, "Nonsmooth optimization via bfgs," *Submitted to SIAM J. Optimiz*, pp. 1–35, 2009.

[65] W. A. Gardner, "Learning characteristics of stochastic-gradient-descent algorithms: A general study, analysis, and critique," *Signal processing*, vol. 6, no. 2, pp. 113–133, 1984.

[66] K. Levenberg, "A method for the solution of certain non-linear problems in least squares," *Quarterly of applied mathematics*, vol. 2, no. 2, pp. 164–168, 1944.

[67] J.-L. Starck, E. Pantin, and F. Murtagh, "Deconvolution in astronomy: A review," *Publications of the Astronomical Society of the Pacific*, vol. 114, no. 800, p. 1051, 2002.

[68] A. I. Lourye, "Some problems of bending of a thin plate," *Prikladnaja Matematika i Mehanika*, vol. 4, pp. 93–102, 1940.

[69] V. V. Apollonov, G. V. Vdovin, V. V. Kiĭko, and S. A. Chetkin, "Flexible adaptive mirror in the form of a thin plate with a free edge and ball-and-socket joints along a circular contour," *Quantum Electronics*, vol. 21, no. 11, pp. 1253–1257, 1991.

[70] V. V. Apollonov, G. Vdovin, E. Ivanova, A. M. Prokhorov, and S. A. Chetkin, "Analytic model of an adaptive mirror in the form of a thin plate with discrete actuators," *Soviet Journal of Quantum Electronics*, vol. 20, no. 11, p. 1414, 1990.

[71] S. Camet, J.-F. Curis, and F. Rooms, "Deformable mirror having force actuators and distributed stiffness," Aug. 5 2014. US Patent 8,794,773.

[72] R. P. Grosso and M. Yellin, "The membrane mirror as an adaptive optical element," *JOSA*, vol. 67, no. 3, pp. 399–406, 1977.

[73] E. S. Claflin and N. Bareket, "Configuring an electrostatic membrane mirror by least-squares fitting with analytically derived influence functions," *JOSA A*, vol. 3, no. 11, pp. 1833–1839, 1986.

[74] P. Halevi, "Bimorph piezoelectric flexible mirror: graphical solution and comparison with experiment," *JOSA*, vol. 73, no. 1, pp. 110–113, 1983.

[75] J. Susini, D. R. Labergerie, and O. Hignette, "R&d program on bimorph mirrors at the esrf," in *Optics for High-Brightness Synchrotron Radiation Beamlines II*, vol. 2856, pp. 130–145, International Society for Optics and Photonics, 1996.

[76] E. Steinhaus and S. Lipson, "Bimorph piezoelectric flexible mirror," *JOSA*, vol. 69, no. 3, pp. 478–481, 1979.

[77] D. Young, "Iterative methods for solving partial difference equations of elliptic type," *Transactions of the American Mathematical Society*, vol. 76, no. 1, pp. 92–111, 1954.

[78] W. H. Press, *Numerical recipes 3rd edition: The art of scientific computing*. Cambridge university press, 2007.

[79] R. Cousty, T. Antonini, M. Aubry, H. T. Krol, and A. Moreau, "Monomorph deformable mirrors: from ground-based facilities to space telescopes," in *International Conference on Space Optics 2016*, vol. 10562, p. 1056231, International Society for Optics and Photonics, 2017.

[80] J. A. Nelder and R. Mead, "A simplex method for function minimization," *The computer journal*, vol. 7, no. 4, pp. 308–313, 1965.

[81] L. Murray, J. C. Dainty, and E. Daly, "Wavefront correction through image sharpness maximisation," in *Opto-Ireland 2005: Imaging and Vision*, vol. 5823, pp. 40–48, International Society for Optics and Photonics, 2005.

[82] M. A. Vorontsov and V. Sivokon, "Stochastic parallel-gradient-descent technique for high-resolution wave-front phase-distortion correction," *JOSA A*, vol. 15, no. 10, pp. 2745–2758, 1998.

$$A$$
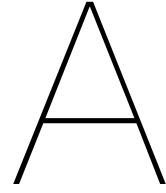
Overview of Code Added to FORTA

The following two tables list the functions and useful scripts added to FORTA, the Fast Optical Ray-Trace Application.

Table A.1: Description of functions and scripts added to FORTA for the modelling of deformable mirrors.

File	Description
PDM model for ray tracing	
PDMfun.m	Main ray trace surface file called in the ray trace procedure. Requires the functions below.
Cylstiff.m	Function to calculate cylindrical stiffness or rigidity of a thin plate, eq. 6.4.
Sgfun.m	Implementation of eq. 6.3.
kfuns.m	Function that returns the series approximation of the polylogarithm for a matrix of complex coordinates, see eq. 6.14.
PDM_Cmat.m	Implementation of eq. 6.7.
PDM_Spmat.m	Implementation of eq. 6.11.
Deformable mirrors	
CILAS_mono85_70.m	MDM model of the up-scaled CILAS MONO85-60 mirror. Requires corresponding files `cilas85zernweights_order20_noll.mat` for a description of the influence functions in terms of Zernike polynomials and file `cilas85_70_modal_relations.mat` for modal control parameters in the DST exit pupil, in terms of normalised actuator signals.
TNO_DM_Optimized.m	PDM model of the optimised mirror presented in this report. Requires the files `actuatorlocations_optimtnodm.mat` and `modes_optimtnodm.mat` for actuator locations and modal control parameters in the DST exit pupil, in terms of actuator signals.
TNO_DM_prototype.m	PDM model of the existing prototype TNO mirror presented in [30]. No modal calibration file has been created.
ALPAO_DM97_50.m	PDM model of the up-scaled Alpao mirror presented in this report. Requires the file `alpao_modal_relations.mat` for modal control parameters in the DST exit pupil, in terms of actuator signals.
modal_calibration_pdm.m and *modal_calibration_mdm.m*	Scripts that calibrate the control signal vectors for different unit modal control variables in the exit pupil, as explained in Chapter 7. A version for PDM and MDM models is available.

Table A.2: Description of functions and scripts added to FORTA for the simulation of the control algorithm

File	Description
Optimisation	
PD_optimizer_GM.m	Preliminary function for estimating the OPD in the exit pupil using simulated phase diversity. See Section 8.7.
FORTAOptimiser.m	Function containing the SGD sharpness optimisation algorithm simulation. The variable `optimsettings` defines the SGD settings. See the implementation details in Chapter 7.
calibrateDM.m	End-to-end calibration simulation function that accepts an *Optical System* object and returns the same system with a calibrated DM. Implements of the ideal coarse and fine calibration `optimsettings` from Chapter 7.
antidriftDM.m	End-to-end drift simulation function that accepts an initial and a drifted *Optical System* object and returns the same system with a DM that compensates the drifts, assuming they are introduced over a 300-second time frame. See Section 8.5.
OptimDM.m	Function that accepts an optical system with an PDM or MDM surface definition and an OPD that should be reduced. Returns a definition of the same system, with DM actuator control settings that ensure an analytical least-squares fit of the DM to the required deformation for OPD removal. See Sections 6.1.2 and 6.4.4.
Fitzernike.m	Function that accepts a surface z on coordinates ρ, φ and returns a least-squares fitted Zernike surface. The Zernike polynomial weights are given in Noll's ordering, with a maximum order of *nmax*. Optionally, *wbound* limits the maximum Zernike weights for each term.
getnoll.m	Function that returns the Noll ordering term of a Zernike polynomial with order *n* and azimuthal frequency *m*.
Zernikesurf.m	Function that returns a Zernike surface definition for the given coordinates, order and frequency and weight. A unit weight gives an RMS value of 1. Uses function `Radpol.m`
Experiments	
RayTracer_PSGD_ID1.m to *RayTracer_PSGD_ID14.m*	Monte-Carlo simulation files that take 100 phased reference systems and return the optical performance of these systems after coarse and fine calibration. The file *planned_experiments.xlsx* shows an overview of the different experiment identifiers and their meaning.